University of Cyprus

DEPARTMENT OF MECHANICAL AND MANUFACTURING ENGINEERING

MATHEMATICAL MODELING AND SYSTEMS BIOLOGY APPLICATIONS IN ONCOLOGY

DOCTOR OF PHILOSOPHY DISSERTATION

CONSTANTINOS HARKOS

2024

University of Cyprus

DEPARTMENT OF MECHANICAL AND MANUFACTURING ENGINEERING

MATHEMATICAL MODELING AND SYSTEMS BIOLOGY APPLICATIONS IN ONCOLOGY

CONSTANTINOS HARKOS

A Dissertation Submitted to the University of Cyprus in Partial Fulfillment of the Requirements for the Degree of Doctor of Philosophy

APRIL 2024

VALIDATION PAGE

Doctoral Candidate: Constantinos Harkos

Doctoral Dissertation Title: Mathematical Modeling and Systems Biology Applications in Oncology

The present Doctoral Dissertation was submitted in partial fulfillment of the requirements for the Degree of Doctor of Philosophy at the ***Department of Mechanical and Manufacturing Engineering*** *and was approved on the 9/4/2024 by the members of the* ***Examination Committee****.*

Examination Committee:

Research Supervisor: Triantafyllos Stylianopoulos_____

Committee Member: Gibin Powathil_____

Committee Member: Vangelis Sakkalis_____

Committee Member: Vasileios Vavourakis_____

Committee Member: Alexandros Syrakos_____

DECLARATION OF DOCTORAL CANDIDATE

The present doctoral dissertation was submitted in partial fulfillment of the requirements for the degree of Doctor of Philosophy of the University of Cyprus. It is a product of original work of my own, unless otherwise mentioned through references, notes, or any other statements.

Constantinos Harkos

……..

ABSTRACT

Η παρούσα διατριβή χρησιμοποιεί το εργαλείο της μαθηματικής μοντελοποίησης για την ανάλυση περίπλοκων βιολογικών συστημάτων με σκοπό την έρευνα στην περιοχή της ανάπτυξης και της θεραπείας καρκινικών όγκων. Η διατριβή ξεκινά με ένα εισαγωγικό Κεφάλαιο (Κεφάλαιο 1) σχετιζόμενο με τις μεθόδους μαθηματικής μοντελοποίησης για τον καρκίνο. Στο Κεφάλαιο 2 παρουσιάζεται το πρώτο μαθηματικό μοντέλο που αναπτύχθηκε στο πλαίσιο της διατριβής, το οποίο βασίζεται στην ενσωμάτωση μη επεμβατικών τεχνικών απεικόνισης δημιουργώντας ένα μαθηματικό μοντέλο εξειδικευμένο για τον ασθενή. Συγκεκτιμμένα το μοντέλο αυτό είναι το πρώτο που χρησιμοποιεί την απεικονιστική μέθοδο Magnetic Resonance Elastography (MRE) από ασθενείς με καρκίνο του εγκεφάλου για να προσομοιώσει την επίδραση των μηχανικών ιδιοτήτων των όγκων στην ανισότροπη ανάπτυξη του όγκου, την ανομοιογένεια των λειτουργικών αγγείων και την μεταφορά της χημειοθεραπείας. Τα αποτελέσματα δείχνουν ότι η ενσωμάτωση της μεθόδου MRE οδηγεί σε πιο ακριβή υπολογισμό των μηχανικών τάσεων και επιτρέπει μια καλύτερη πρόβλεψη της ετερογενής ανάπτυξη του αγγειακού δικτύου οδηγώντας σε διαφορές μεταξύ των ασθενών στην αιμάτωση και την μεταφορά των φαρμάκων. Η έρευνα αυτού του κεφαλαίου δημοσιεύτηκε στο περιοδικό Cancers. 2022;14: 884. https://doi.org/10.3390/cancers14040884

Στο Κεφάλαιο 3 το μοντέλο ανάπτυξης του όγκου επεκτάθηκε για την εξέταση της απόκρισης του ανοσοποιητικού συστήματος μετά την χορήγηση ανοσοθεραπείας. Συγκεκριμένα, το μοντέλο προσδιορίζει την αποτελεσματικότητα των ενέσιμων συζευγμένων κυτοκινών εντός του όγκου, λαμβάνοντας υπόψη τις ιδιότητες του μικροπεριβάλλοντος του όγκου και των κυτοκινών. Οι προσομοιώσεις του μοντέλου δείχνουν πώς οι ιδιότητες του όγκου και των κυτοκινών καθορίζουν τα αποτελέσματα της θεραπείας. Η έρευνα αυτή δημοσιεύτηκε στο περιοδικό PLOS Computational Biology. 2023;19: e1011740. https://doi.org/10.1371/journal.pcbi.1011740

Στο Κεφάλαιο 4, το πλαίσιο μοντελοποίησης που αναπτύχθηκε στο Κεφαλαίου 3, συνδυάστηκε με την Φαρμακοκινητική-Φαρμακοδυναμική μοντελοποίηση για να συμπεριλάβει τους λεμφαδένες, όπου λαμβάνουν χώρα σημαντικές λειτουργίες του

ανοσοποιητικού συστήματος, όπως η παρουσίαση του αντιγόνου και η ανάπτυξη διαφόρων κυττάρων του ανοσοποιητικού. Αυτό το μοντέλο επιπρόσθετα ενσωματώνει την θεραπεία ανοσοθεραπείας με αναστολείς σημείων ελέγχου του ανοσοποιητικού (immune checkpoint blockers (ICBs). Τα αποτελέσματα της ανάλυσης κατέδειξαν ότι ο συνδυασμός της θεραπείας ICB και των θεραπειών που στοχεύουν στη βελτίωση της αιμάτωσης του όγκου, μειώνει την πίεση του ενδιάμεσου υγρού στο όγκο και αυξάνει τη συγκέντρωση των ανοσοκυττάρων στο κέντρο του όγκου αντί για την περιφέρεια. Η ανάλυση βρήκε επίσης ότι ο αριθμός των λειτουργικών αγγείων μέσα στην περιοχή του όγκου και η δόση ICB που χορηγείται έχουν την μεγαλύτερη συνεισφορά στα αποτελέσματα της θεραπείας. Η έρευνα αυτή έχει δημοσιευτεί στο περιοδικό Journal of Theoretical Biology. 2024; 111768. https://doi.org/10.1016/j.jtbi.2024.111768

Στο Κεφάλαιο 5 έχει συνδυαστεί το μοντέλο ανάπτυξης του όγκου και της απόκρισης του ανοσοποιητικού συστήματος με στατιστική ανάλυση για να διερευνήσει τον ρόλο του εντερικού μικροβιώματος, το οποίο έχει αναδειχθεί ως ένας ρυθμιστής της ανοσοθεραπείας. Αυτό το πλαίσιο μοντελοποίησης συνδυάζει i) δεδομένα εντερικού μικροβιώματος που προέρχονται από ποντίκια με μελάνωμα μετά από μεταμόσχευση κοπράνων, ii) μοντελοποίηση της απόκρισης του ανοσοποιητικού συστήματος, και iii) ανάλυση συσχέτισης των προφίλ μικροβιωμάτων ποντικών και ανθρώπων με τα προβλεπόμενα από το μοντέλο ανοσοποιητικά προφίλ. Τα αποτελέσματα του μοντέλου δείχνουν ότι το μικροβίωμα επηρεάζει την ενεργοποίηση και τον ρυθμό που σκοτώνουν τα ανοσοκύτταρα και προβλέπουν συσχετίσεις μεταξύ συγκεκριμένων βακτηρίων και ανοσοκυττάρων. Η έρευνα αυτή βρίσκεται υπό κρίση στο περιοδικό Nature Computational Sciences. https://doi.org/10.21203/rs.3.rs-3647386/v1

Η διατριβή καταλήγει με μια σύνοψη τω κυριότερων ευρημάτων και με εισηγήσεις για μελλοντική έρευνα (Κεφάλαιο 6). Μελλοντική έρευνα έχει ως στόχο να συνδυάσει αυτές τις διάφορες προσεγγίσεις μοντελοποίσης σε ένα γενικό μοντέλο για την διερεύνηση διαφόρων παραγόντων στην ανάπτυξη και θεραπεία του όγκου το οποίο μπορεί να οδηγήσει σε ψηφιακές κλινικές δοκιμές και στην αναγνώριση βιοδεικτών.

ABSTRACT

This thesis uses the valuable tool of mathematical modelling to model and analyse complex biological systems (Systems Biology) to investigate tumor progression and treatment. It applies a tumor growth model to different applications incorporating various modelling approaches. The thesis begins with an introductory chapter (Chapter 1) providing a framework of the mathematical analysis for cancer, then in Chapter 2 it integrates non-invasive imaging techniques creating a patient specific mathematical model. The model is the first one to our knowledge that uses patients' Magnetic Resonance Elastography (MRE) images to simulate the effect of tumor-specific biomechanical properties and their effects on tumor anisotropic growth, vascular density heterogeneity and chemotherapy delivery. The results show that incorporating MRE data provide a more accurate calculation of intratumoral mechanical stresses and enables a better mathematical description of subsequent events, such as the heterogeneous development of the tumor vasculature and intrapatient variations in tumor perfusion and delivery of drugs. This work was published in the journal Cancers. 2022;14: 884. https://doi.org/10.3390/cancers14040884

In Chapter 3 the tumor growth model is extended to investigate the immune response after administration of immunotherapy. Specifically, it determines the efficacy of intratumorally-injected conjugated-cytokines accounting for properties of the tumor microenvironment and the conjugated-cytokines. Model simulations show how the properties of the tumor and of the conjugated-cytokines determine treatment outcomes and how selection of proper parameters can optimize therapy. This work has been published in PLOS Computational Biology. 2023;19: e1011740. https://doi.org/10.1371/journal.pcbi.1011740

In Chapter 4, the modeling framework of Chapter 3 was combined with Pharmacokinetic-Pharmacodynamic modeling to incorporate the tumor draining lymph nodes were important functions of the immune system take place like the antigen presentation and the development of cytotoxic immune cells. This model incorporates immune checkpoint blockade (ICB) therapy which is another type of immunotherapy. The results show that combination of ICB therapy and normalization treatments, that aim to improve tumor perfusion, decreases interstitial fluid pressure and increases the concentration of immune cells at the tumor center

rather than the periphery. The analysis also found that the number of functional vessels inside the tumor region and the ICB dose administered have the largest impact on treatment outcomes. This research has been published in the Journal of Theoretical Biology. 2024; 111768. https://doi.org/10.1016/j.jtbi.2024.111768

Chapter 5 merges the tumor growth, immune response with statistical approaches to investigate the role of the gut microbiome which has emerged as a key regulator of immunotherapy. This modeling framework combines i) gut microbiome data derived from preclinical studies on melanomas after fecal microbiota transplant, ii) mechanistic modeling of antitumor immune response, and iii) robust association analysis of murine and human microbiome profiles with model-predicted immune profiles. Model results show that the microbiome affects the activation and killing rate of immune cells. Furthermore, combination of mechanistic modeling with association analysis identifies associations between specific bacterial taxonomies and immune cells. This research is in revision in Nature Computational Sciences. https://doi.org/10.21203/rs.3.rs-3647386/v1

The thesis concludes with a summary of key findings and suggestions for future research (Chapter 6). Future work aims to merge those modeling approaches in a global modeling framework for investigating various aspects of tumor progression and treatment, which can lead to in silico trials and biomarkers identification.

Acknowledgements

The thesis is dedicated to the memory of Charis Kourras

First and foremost, I am deeply grateful to my supervisor Professor Triantafyllos Stylianopoulos and Professor Rakesh K. Jain for their support and valuable advice. Their expertise have inspired me to become a better researcher.

This endeavour would not have been possible without the continuous support of the members of the Cancer Biophysics Laboratory, especially Dr. Valantis Voutouri.

Kyriaki, thank you for your unconditional love. Without your support I wouldn't be able to finalize my PhD journey.

I would like to thank from the bottom of my heart my grandmother Eleni for her support all these years.

I would also like to thank my parents, and my sister Ivi.

Irene, Michales and Savvas thank you for giving me joy since you were born.

Table of Contents

List of Figures

List of Tables

Chapter 1: Introduction

A solid tumor is characterized by an accumulation of cancer cells mixed with a variety of host cells, all embedded within an extracellular matrix. This formation is nourished by blood vessels, also the lymphatic vessels assist in the removal of fluids [1]. The main function of these blood vessels is to transport blood, vital nutrients, and therapeutic agents to the tumor site. In contrast to normal blood vessels, the blood vessels developed in the tumor region possess larger pores on their walls, which allows blood to escape into the adjacent space. This adjacent space is known as the interstitial space. Besides the vascular network, the lymphatic system also plays an integral part. The lymphatic vessels are responsible for absorbing excess plasma and additional fluids that seep into the interstitial space through the pores of the blood vessels. This process effectively removes fluid from the interstitial space, thereby regulating hydrostatic pressure in normal regions.

The proliferation of cancer cells within the confined space of the host tissue along with the accumulation of stromal cells and extracellular matrix components (e.g., collagen and hyaluronan) induces stiffening of the tumor and compression of intratumoral blood vessels [2–4]. Thus solid stresses are exerted by stroma and cancer cells and the tumor extracellular matrix [5–8]. There are also fluid stresses associated with the interstitial and vascular fluid pressure [9,10]. Due to the abnormal nature of the intratumoral vasculature, the larger pores and the increased leakiness the interstitial fluid pressure (IFP) is elevated. This reduces the pressure gradient among the interstitial pressure and the vascular pressure reducing the pressure gradient that induces the transport of nutrients and drugs with convection inside the tumor[11–14].

Additionally, vessel compression makes the vessels dysfunctional reducing their ability to transport nutrients or drugs by either diffusion or convection. A significant result of the reduced nutrients-oxygen in the region is that the cancer cells become invasive in an effort to find nutrients [15]. Furthermore, reduced blood flow impairs the transport of immune cells to the tumor location as well. The hypoxic conditions in the tumor microenvironment (TME) create an immunosuppressive environment, reducing the effectiveness of immune effector cells in destroying cancer cells and thus reducing the outcome of immunotherapy [16,17].

One approach of enhancing the efficacy of chemotherapy and immunotherapy is the use of agents that reprogram the TME (mechanotherapeutics). These agents aim to restore the mechanical properties of the tissue as well as the blood vessels' functionality inside the tumor. A less compressed TME with more functional vessels increases the delivered chemotherapeutic agents, the delivery of immunotherapeutic agents and the delivery of immune cells[1,18].

More specifically, chemotherapy is a type of treatment that directly attacks cancer cells. On the other hand, immunotherapy works by boosting the host immune system to destroy tumor cells [19]. This method of aiding the host immune cells in combating cancer without relying on cytotoxic drugs presents a hopeful strategy, necessitating a deeper comprehension of the immune system and its reaction to immunotherapy. Although, there are various types of immunotherapies in this thesis two types are investigated: i) Immune checkpoint blockade (ICB) therapy that uses immune checkpoint inhibitors (ICIs) [19] and ii) the injection of cytokines [20–22]. Immune checkpoint blockers (ICBs) or ICIs block the checkpoint proteins from binding with their counterparts. When the checkpoint proteins bind, they stop the immune system from attacking cancer cells. Thus, blocking the binding with immune checkpoint blockers enhances the immune system on recognizing and killing cancer cells. Common examples of checkpoint inhibitors are the cytotoxic T-lymphocyte associated protein 4 (CTLA4), programmed cell death protein 1 (PD1) and programmed cell death ligand 1 (PDL1) inhibitors.

The other type of immunotherapy investigated in this thesis uses cytokines that are small proteins that control the activity of the immune system. The pro-inflammatory cytokines are produced by the immune cells in an effort to enhance the immune response against the tumor. Injecting pro-inflamatory cytokines like interleukin 2 (IL2) and interleukin 12 (IL12) enhances the host immune system to kill tumor cells [20–22].

Despite the potential of immunotherapy, less than 20% of patients currently experience benefits [23] with many of those encountering immune-related adverse effects [24]. This led the research community to investigate ways to enhance the effect of immunotherapy. The last few years the gut microbiome has emerged as regulator of immunotherapy [25–27]. The microbiome is a collection of bacteria, viruses and microbes that leave mainly inside the gut. Those microorganisms play a crucial role in various functions of the human body like

digestion, metabolism and immune function. Recent experimental trials have demonstrated how fecal microbiota transplants (FMT) can benefit immunotherapy [25,28–33]. FMT is the transplantation of faces from a donor to another subject. Usually, the donor has previously responded to immunotherapy and thus the microbiome of the donor's intestine consists of microbes that benefit immunotherapy. The beneficial microbiome is transplanted to another subject in an effort to adjust the receiver's microbiome to a set of microbes that are beneficial for a follow up injection of immunotherapeutic agents [29,30,34].

Mathematical modeling can be proven very useful in capturing these complex, dynamic and heterogeneous events that take place within a growing tumor and make predictions for optimal designing of therapeutic agents, diagnostic tools and treatment strategies [1]. Furthermore, due to the variation of the treatment outcome in many patients, patient specific mathematical modeling can have multiple clinical uses, including predictions making, treatment planning and expert diagnostic assistance [35]. Additionally, given that treating and investigating cancer treatments requires high costs [36] , this makes mathematical modeling a valuable and low-cost tool for predicting treatment outcomes and best combinations of therapeutic approaches with minimal adverse effects [37].

Various types of modeling approaches were followed over the years. One of those approaches is Pharmacokinetic (PK) – Pharmacodynamic (PD) modeling. PK is the study of how the body processes a drug and can define the dose schedule, whereas PD is how a drug affects the body to produce its therapeutic effects. PK-PD modeling is especially useful in preclinical trials for drug discovery and determination of the optimal dose of the drug [38]. The majority of PK-PD models describe the time evolution of a tumor to a given therapeutic using a set of ordinary differential equations (ODEs) [39].

Furthermore, another modeling approach is the distributed parameter modeling that integrates continuum mechanics which is the study of the mechanical behavior of matter has been proven a valuable tool for generating models that simulate tumor growth, stress progression, transport of drugs and nutrients [40]. Continuum mechanics can be used in finding the optimal dosage of a treatment and examining/developing new treatment strategies [41,42].

Another modeling approach are the discrete and stochastic models that treat the cells or the vasculature as discrete entities are quite useful in examining proliferation, migration, death,

angiogenesis or any other processes. Continuum and discrete approaches can be combined in generating hybrid models to investigate multiple factors that contribute to tumor progression or treatment at different length scales [43].

Due to that the treatment outcome varies from patient to patient and thus, Imaging fused with mathematical modeling makes the development of patient specific models possible [44,45]. This can have multiple clinical uses, including predictions making, treatment planning and expert diagnostic assistance [35].

Finally, the vast heterogeneity of tumors and variability in responses makes the use of advanced statistical analysis and machine learning methods a valuable tool to understand underlying the mechanisms, identify the most crucial biological programs and develop biomarkers predictive of response [46–49].

In this thesis a modeling framework of tumor growth was used in various applications. Firstly, Chapter 2 integrates non-invasive imaging techniques to the continuous tumor growth model creating a patient specific mathematical model (Figure 1). It also applies a set of equations for the drug delivery in this case to model transport of chemotherapy by also considering properties of the TME. The model is the first one to our knowledge that uses patients' Magnetic resonance elastography (MRE) to simulate the effect of tumor-specific biomechanical properties and their effect on tumor anisotropic growth, vascular density heterogeneity and chemotherapy delivery.

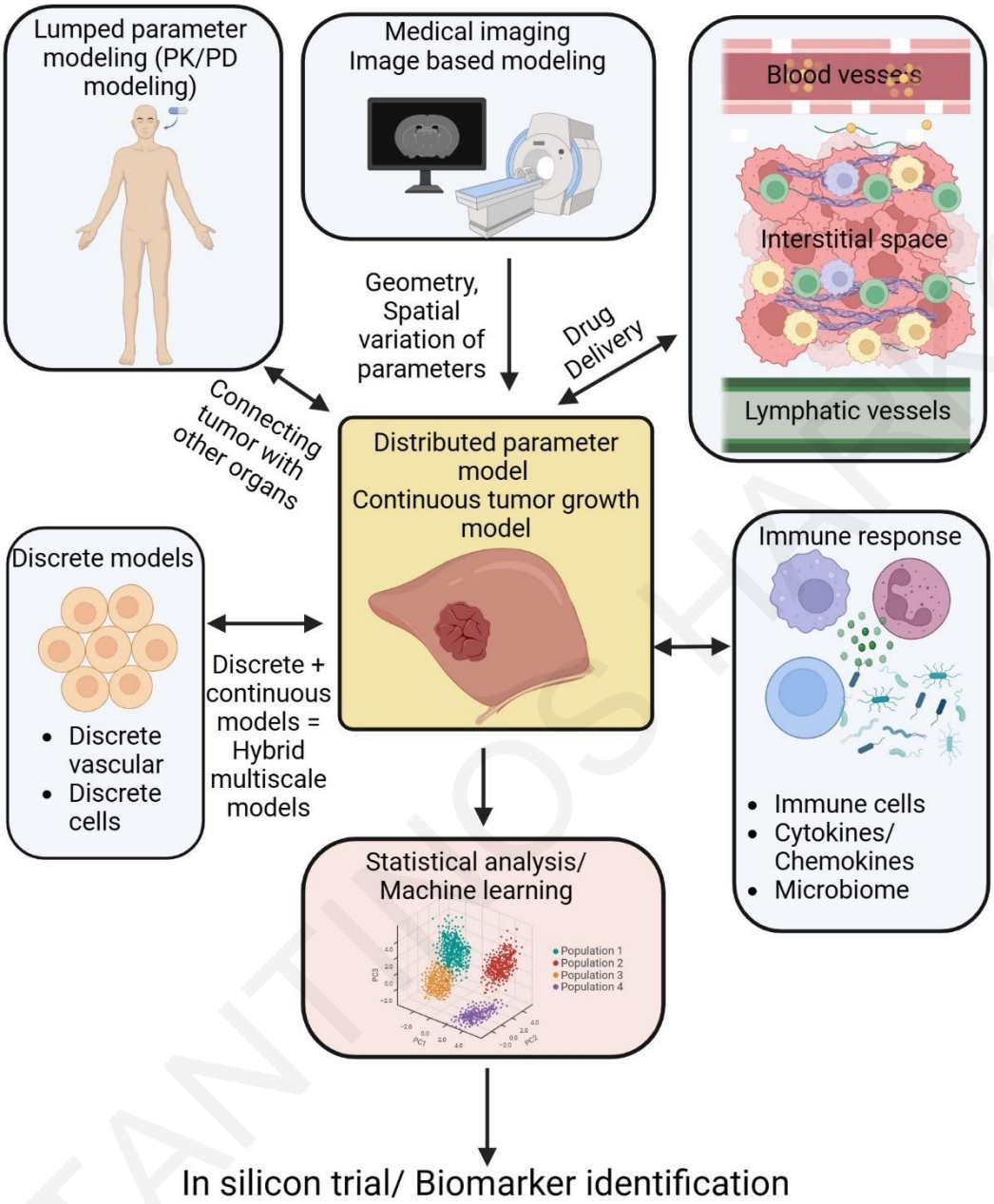

Figure 1: Framework of mathematical modelling of solid tumors. The schematic shows how different modelling approaches can be combined for modelling the dynamic and complex aspects of tumor progression and treatment.

Secondly, Chapter 3 illustrates a mathematical model that uses the continuous tumor growth model in combination with the equations of the drug delivery and a set of equations for the

immune response (Figure 1). This model investigates the intratumorally-injected conjugated-cytokines, accounting for properties of the TME and the conjugated-cytokines.

Thirdly, Chapter 4 extends the modeling framework presented in Chapter 3. This model not only includes the continuous tumor growth model combined with the transport equations and the equations of the immune response but also incorporates PK-PD modeling (Figure 1) by considering the tumor draining lymph nodes (TDLNs). In the TDLNs important functions of the immune system take place like the antigen presentation and the development of cytotoxic immune cells. This model incorporates ICB therapy by also investigating the effect of normalizations treatments that aim to improve tumor perfusion.

Finally, Chapter 5 merges the tumor growth model, the immune response equations and statistical approaches (Figure 1) to investigate the role of the gut microbiome which has emerged as a key regulator of response to cancer immunotherapy. More specifically, this modeling framework combines i) gut microbiome data derived from preclinical studies on melanomas after fecal microbiota transplant, ii) mechanistic modeling of antitumor immune response, and iii) robust association analysis of murine and human microbiome profiles with model-predicted immune profiles.

The thesis concludes with a summary of key findings and suggestions for future research (Chapter 6). Future work aims to merge those modeling approaches in a global modeling framework for investigating various aspects of tumor progression and treatment, which can lead to in silico trials and biomarkers identification.

Chapter 2: Inducing biomechanical heterogeneity in brain tumor modeling by MR Elastography: effects on tumor growth, vascular density and delivery of therapeutics

This study has been published in the journal Cancers: Harkos C, Svensson SF, Emblem KE, Stylianopoulos T. Inducing biomechanical heterogeneity in brain tumor modeling by MR Elastography: effects on tumor growth, vascular density and delivery of therapeutics. Cancers. 2022;14: 884. https://doi.org/10.3390/cancers14040884

Summary

The purpose of this chapter is to develop a methodology that incorporates a more accurate assessment of tissue mechanical properties compared to current mathematical modeling by use of biomechanical data from magnetic resonance elastography. The elastography data were derived from five glioblastoma patients and a healthy subject and used in a model that simulates tumor growth, vascular changes due to mechanical stresses and delivery of therapeutic agents. The model investigates the effect of tumor-specific biomechanical properties on tumor anisotropic growth, vascular density heterogeneity and chemotherapy delivery. The results showed that including elastography data provides a more realistic distribution of the mechanical stresses in the tumor and induces anisotropic tumor growth. Solid stress distribution differs among patients, which, in turn, induces a distinct functional vascular density distribution—owing to the compression of tumor vessels—and intratumoral drug distribution for each patient. In conclusion, incorporating elastography data results in a more accurate calculation of intratumoral mechanical stresses and enables a better mathematical description of subsequent events, such as the heterogeneous development of the tumor vasculature and intrapatient variations in tumor perfusion and delivery of drugs.

Introduction

Glioblastoma multiforme (GBM) is one of the most common primary brain tumors [50,51]. Despite the different treatments developed, it remains a devastating disease with a poor prognosis and an overall survival of 14 to 15 months [52,53]. The response to treatment varies from patient to patient. Thus, the development of patient-specific mathematical

models not only enables further understanding of glioblastoma development but also allows the optimization of a patient's treatment [54].

Mathematical models can be divided into two categories based on the scale at which the tumor is represented. The models can be discrete/stochastic, with an emphasis on the microscopic scale and the interactions at the cellular level, or continuum models, which focus on events taking place at the macroscopic scale [55,56]. Hybrid-multiscale models have also been developed that combine elements of both microscopic and macroscopic models [57]. GBM models most often combine the human brain geometry derived from magnetic resonance imaging (MRI) or computer tomography (CT) with equations accounting for cancer cells' proliferation and diffusion [58–60]. This modeling strategy allows for the prediction of patterns of submicroscopic tumor invasion not detectable by MRI images [58–60]. Some models even consider anisotropic diffusion based on data derived from diffusion tensor imaging (DTI MRI), which allows for patient-specific predictions of the shape and evolution of the tumor [44,61,62]. A probabilistic diffusion coefficients scheme in the diffusion reaction equation has also been employed instead of fixed diffusion parameters to improve predictions [63,64]. Furthermore, some studies focus on simulating treatments, such as radiotherapy [65–68], while others simulate chemotherapy based on the patient's imaging data [69,70].

The realization that not only biological and brain physiological factors but also biomechanical forces drive brain tumor progression has led to the development of mathematical models that account for tissue biomechanical properties [71,72]. The effect of the biomechanical properties is crucial because tumor progression is associated with the onset and accumulation of mechanical stresses [18,73–75]. A source of mechanical stress is solid stress exerted by stromal and cancer cells and the tumor extracellular matrix as a consequence of a growing tumor, which deforms the surrounding tissues [5–8]. There are also fluid stresses associated with the interstitial and vascular fluid pressure [9,10]. Glioma in silico models consider the effect of stresses with either continuous or discrete approaches [76–79]. Solid stresses can directly affect glioma cell proliferation and migration [80,81]. They can also induce blood vessel compression and dysfunction, limiting perfusion rates and, thus, oxygen and chemotherapeutic agents' transport into the tumor [74,82]. Oxygen levels, in turn, affect cancer cell proliferation, tumor growth and invasion as proliferative

cells can become invasive under hypoxic conditions [15,71,76,81,83–86]. Thus, the normalization of brain tumor blood vessels to restore vessels' hyper-permeability and compression can lead to improved perfusion and therapeutic efficacy [87,88]. The incorporation of tissue mechanics on tumor growth models improves predictions on preclinical models and also helps distinguishing radiation necrosis from tumor progression in patients [89,90].

For a better understanding of the biomechanical tumor microenvironment, a detailed quantification of the mechanical properties of the normal and tumor brain is required. Magnetic resonance elastography (MRE) is a promising imaging technique, which allows for noninvasive quantification of the mechanical properties of tissues by applying external vibrations [91]. Biomechanical properties provide information about tissue stiffness, which is related to the magnitude of mechanical stresses developed in the tumor. Even though MRE has been used for studying brain cancer in patients and animal models [92,93], it has not been used in simulations of brain tumor development, omitting the importance of biomechanical properties in tumor progression.

To this end, we present a mathematical model that incorporates not only conventional anatomical and DTI MRI data but also considers MRE data for a more realistic representation of the biomechanical properties and mechanical stresses in healthy and malignant brain tissues. The model combines the elastography data of a healthy subject's brain with those of five patients with GBM. Our model simulates tumor progression by assuming that the non-uniform distribution of mechanical stresses promotes proliferation towards low-stress regions [94–98]. This allows for predictions of patient-specific anisotropic tumor growth, non-uniform vessel compression and heterogeneous distribution of functional tumor vessels. Heterogeneous vascular density, in turn, determines chemotherapeutic agents' transport, posing limits to effective drug delivery [82]. The model highlights the important relationship of elastography data with tumor anisotropic growth, vascular density and chemotherapy delivery and can be a valuable tool for optimizing cancer treatment by using patient-specific noninvasive medical imaging.

Materials and methods

Application of MR Imaging data in the model

MR imaging was performed on a 3T clinical MRI scanner (Ingenia, Philips Medical Systems, Best, The Netherlands) using a 32-channel head coil. Anatomical T1-weighted, T2-weighted and fluid attenuated inversion recovery (FLAIR) images, as well as DTI MRIs and MRE data, were acquired for five patients, using imaging parameters as in [99], also shown in

Table 9. The MRE was performed using a gravitational transducer [100] attached on the side of the head, inducing shear waves of 50 Hz into the brain. The MRE acquisition lasted 5.5 min, with further details about acquisition and processing listed in reference [101]. Patients were between 53 and 75 years (median 60 years), with two female patients and three male patients. All patients had IDH-wildtype glioblastomas, and tumor sizes ranged from 41 cm^3 to 110 cm^3 (median 60 cm^3). Imaging was performed before any treatment. For a healthy subject (a 34-year-old woman), the MRE imaging was extended to cover the entire brain.

Storage and loss modulus values were derived from the MRE data using a localized divergence-free finite element reconstruction [101,102]. The storage modulus relates to the material's ability to store energy and the loss modulus describes the material's ability to dissipate stress through heat. The MRE data for both the patients and the healthy subject were converted from a digital imaging and communications in medicine (DICOM) format to Matlab format. Diffusion tensors were derived from the DTI MRI scan of the healthy subject. This was performed using the Diffusion Toolkit (Massachusetts General Hospital, Boston, MA, USA) following a similar procedure as in a previous study [44]. Diffusion tensors were converted to Matlab matrix format too.

A brain geometry employed in a previous study [72] was used here. This geometry instead of the patients' geometry was used to include the hole brain domain. This was done because only the tumour region of the patients was available and not the hole brain. To reduce computational demands, only the gray matter and white matter regions were included. Generation of the 3D geometry was performed using ScanIP (Simpleware Ltd., Mountain View, CA, USA [72]. The geometry was then imported in COMSOL Multiphysics (COMSOL, Inc, Burlington, MA, USA). Inside the brain geometry, a small spherical tumor,

with a radius of 5 mm, acting as the initial tumor seed, was added in the same position for all cases to avoid host tissue mechanical heterogeneities.

A mesh was generated in COMSOL Muliphysics (COMSOL, Inc, Burlington, MA, USA) as shown in Figure 2. A finer mesh was used inside and around the tumor domain compared to the rest of the brain in order to improve accuracy and reduce computational cost. The mesh included two types of elements: 1008 prisms that form boundary layers at the tumor boundary and 34,468 tetrahedra for the rest of the geometry.

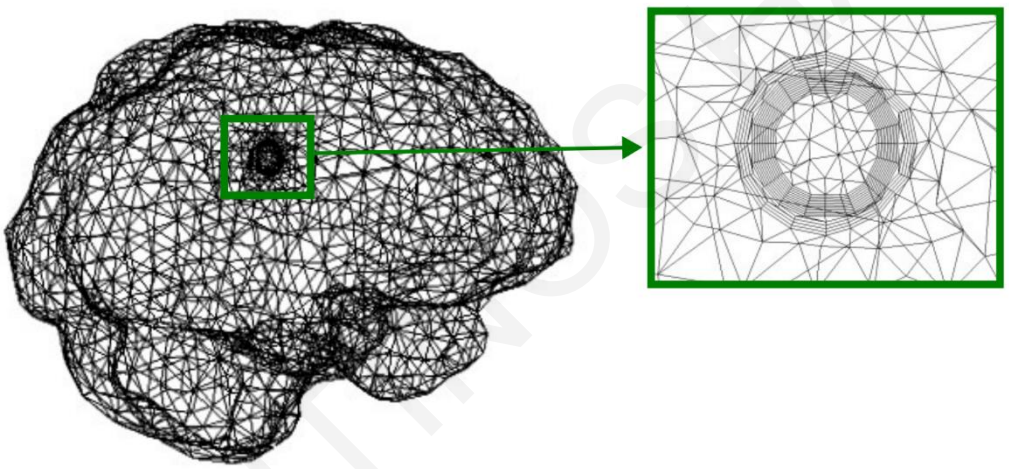

Figure 2: The mesh used for the solution of model equations with the finite element method. The mesh includes two types of elements: 1008 prisms that form boundary layers at the tumor boundary and 34,468 tetrahedra for the rest of the geometry. The boundary layers enabled the capturing of steep changes at the tumor periphery.

The storage, loss modulus and diffusion tensors matrices derived from the healthy subject were applied on the brain domain in COMSOL Multiphysics. This was done using interpolation. Specifically, a MATLAB's built-in interpolation function was used (scatteredInterpoland with the method set to natural interpolation). This enabled the

interpolation the data existing in the MATLAB matrices to the nodes of the finite elements in COMSOL Multiphysics. The same interpolation was used for the patient's data to the initial tumor seed. This required a deformation of the patient's data prior to the interpolation, as shown in Figure 3.

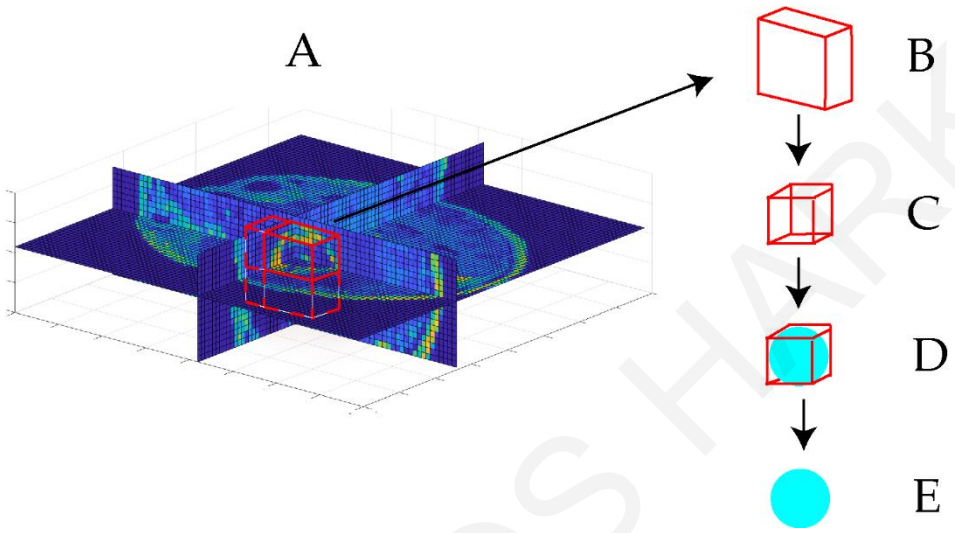

Figure 3: The figure presents how the DTI and MRE data from the tumors of the patients were applied to the initial tumor seed of the model. This was done by deformation and interpolation of the patient's data to the initial tumor seeds' mesh elements: (a) T1c MRE space used to locate the tumor region of each patient, (b) tumor data of each patient, (c) deforming the data into becoming a cube, (d) interpolating the data of the cube to each initial tumor seed, (e) initial tumor seed with data.

For each patient dataset, a rectangular parallelepiped containing the tumor data was extracted. For each patient's data, the rectangular parallelepiped had the smallest possible dimensions that fitted inside the tumor domain. The parallelepiped was deformed into a cube and then interpolated to the initial tumor seed. For each simulation performed, the tumor seed was subjected to each patient's elastography data and to the same surrounding elastography data of the normal tissue (derived from the healthy subject). This was done to examine the effect of different tumor elastography properties on the tumor growth.

Figure 4 and Figure 5 depict the shear modulus values, G, which are used for the constitutive equation of the normal and brain tumor material model.

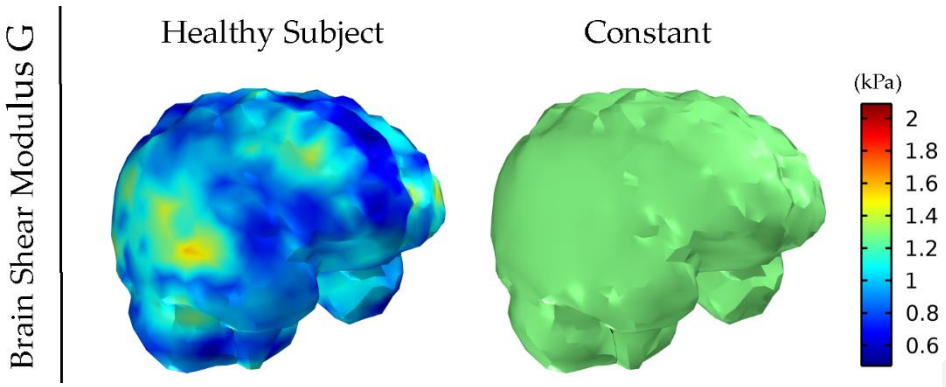

Figure 4: Healthy subject's shear modulus, G, of the brain derived by MRE. The value for the constant shear modulus is the average of the healthy subject's data. The constant case was used to compare tumor development in the case of incorporating the MRE data and in the case of not incorporating the MRE data (constant case)

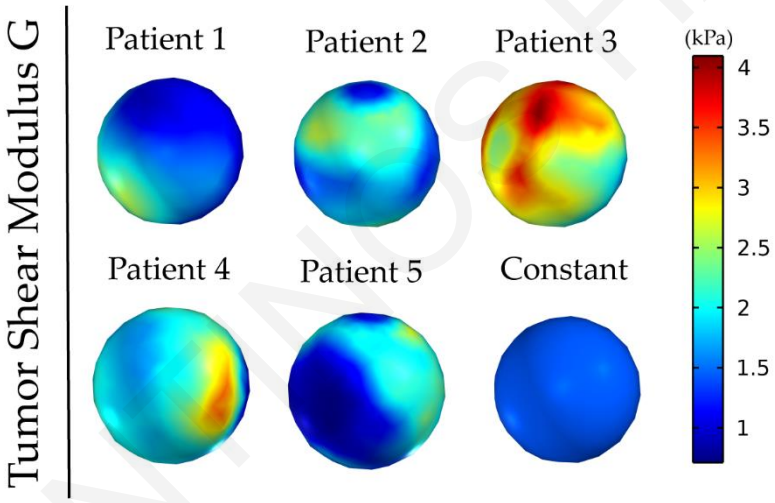

Figure 5: Patients' tumor shear modulus, G, derived from MRE as it was fitted on the initial tumor seed of the model. The value for the constant shear modulus case is the average value of patient's 1.

The complex shear modulus $G^*(\omega)$ can be written as $G^*(\omega) = G'(\omega) + G''(\omega)\,\boldsymbol{i}$, where G' and G'' are the storage and loss modulus calculated by MRE and given by

$$G'(\omega) = G\frac{(\omega\tau_m)^2}{1+(\omega\tau_m)^2} \quad (1)$$

$$G''(\omega) = G\frac{\omega\tau_m}{1+(\omega\tau_m)^2} \quad (2)$$

where ω is the radial frequency, τ_m is the characteristic decay time and G is the shear modulus [103]. In the model, we only considered elastic effects as transient effects due to tissue viscoelastic properties associated with the characteristic decay time were assumed negligible due to the relatively slow growth/deformation rates.

Kinematics of tumor growth

Tumor growth is based on principles of continuum mechanics. The deformation gradient tensor, **F**, was decomposed into two components [104,105].

$$\mathbf{F} = \mathbf{F_e}\cdot\mathbf{F_g}, \quad (3)$$

where $\mathbf{F_e}$ is the elastic (reversible) component of **F** that is related to the stress response of the material. $\mathbf{F_g}$ is the inelastic (growth, irreversible) component of **F**. The diagonal components of $\mathbf{F}_g$ correspond to the growth stretch ratios in the x,y,z direction (λ_{gx}, λ_{gy},λ_{gz})

$$\mathbf{F_g} = \begin{bmatrix} \lambda_{gx} & 0 & 0 \\ 0 & \lambda_{gy} & 0 \\ 0 & 0 & \lambda_{gz} \end{bmatrix}. \quad (4)$$

The elastic component of the deformation gradient tensor is calculated as,

$$\mathbf{F_e} = \mathbf{F}\cdot\mathbf{F_g}^{-1} \quad (5)$$

and the growth stretch ratios are calculated as [94,106],

$$\frac{1}{\lambda_{ga}}\frac{d\lambda_{ga}}{dt} = \Gamma_a r_g\,,\ a = x,y,z, \quad (6)$$

where λ_{ga} is the growth stretch ratio in each direction (α = x,y,z) and r_g is the mass growth per unit of the current mass. The anisotropic growth multiplier, Γ_a, defines the distribution of the growth term, r_g, among the three directions (x,y,z) and is written as,

$$\Gamma_a = \Gamma_\Sigma^{-1} \exp(A\,\sigma^s_{aa}/k)\,,\ a = x,y,z, \tag{7}$$

$$\Gamma_\Sigma = \exp(A\,\sigma^s_{xx}/k) + \exp\left(A\,\sigma^s_{yy}/k\right) + \exp(A\,\sigma^s_{zz}/k) \tag{8}$$

$\boldsymbol{\sigma}^s$ is the Cauchy stress, k is the bulk modulus of the tumor and Γ_Σ is defined in a way that $\sum_a \Gamma_a = 1$ is satisfied. A is a parameter describing the degree of anisotropy [106]. When A = 0, the Equation (6) becomes

$$\frac{3}{\lambda_g}\frac{d\lambda_g}{dt} = r_g \tag{9}$$

the growth stretch ratios, λ_{ga}, become the same and the model accounts for isotropic tumor growth [107]. For $A > 0$, the larger the value of A, the higher the degree of anisotropy, and growth occurs mostly at the directions of lower stress magnitude [95–98].

The growth term, r_g, depends on the oxygen concentration in the tissue, c_{ox}, and the cancer cell density, T_{cel} [44],

$$r_g = \frac{k_1\, c_{ox}}{k_2 + c_{ox}}\, T_{cel} \tag{10}$$

where k_1, k_2 are growth rate parameters.

Stress balance

According to the biphasic theory for soft tissues [108], the total stress tensor, σ_{tot}, can be expressed as the summation of the solid phase stress tensor, σ^s, and the stress tensor, $p_i I$, due to the effect of the interstitial fluid pressure p_i,

$$\nabla\cdot\boldsymbol{\sigma}_{tot} = 0 \Rightarrow \nabla\cdot(\boldsymbol{\sigma}^s - p_i\mathbf{I}) = 0 \tag{11}$$

The Cauchy stress tensor, $\boldsymbol{\sigma}^s$, is expressed as [109],

$$\boldsymbol{\sigma}^s = J_e^{-1}\mathbf{F_e}\frac{\partial W}{\partial \mathbf{F_e}^T}, \tag{12}$$

where $Je = \det\mathbf{F_e}$ and W is the strain energy density function of the tissue [110].

$$W = \frac{G}{2}\left(\bar{I}_1\text{-}3\right) + \frac{k}{2}(J_e\text{-}1)^2 \quad (13)$$

where G is the shear modulus calculated from the elastography data and I_1 is the first invariant of the elastic Green–Cauchy deformation tensor.

Cancer cell density

Cancer cell density, T_{cel}, was normalized by division with a reference initial value of 10^7cells/cm^3 [111]. Thus, the initial value was set to 1 for the tumor region and to 0 for the host tissue. T_{cel} is given by the diffusion–reaction equation,

$$\frac{\partial T_{cel}}{\partial t} + \nabla\cdot(-\mathbf{D_T}(x)\nabla\mathbf{T_{cel}}) = R \quad (14)$$

$$R_{tumor} = r_g = \frac{k_1\, c_{ox}}{k_2 + c_{ox}} T_{cel} \quad (15)$$

$$R_{host} = \rho_{cell} T_{cel} \quad (16)$$

where $\mathbf{D_T(x)}$ is the inhomogeneous and anisotropic diffusion tensor acquired from the DTI MRI [44,64,112]. In the tumor region, cancer cell proliferation is associated with oxygen supply. The cancer cells that escape the tumor domain due to diffusion were assumed to have a constant proliferation rate, ρ_{cell}.

Interstitial pressure-fluid velocity

Normal and tumor tissues have properties similar to those of a porous medium. According to Darcy's law, the interstitial fluid velocity is given by

$$\mathbf{v^f} = -k_{th}\,\nabla\mathbf{p_i} \quad (17)$$

where k_{th} is the hydraulic conductivity of the interstitial space [113]. The mass balance gives [114,115],

$$\nabla\cdot(\mathbf{v}^f) = L_p S_v\,(p_v\text{-}p_i)\text{-}L_{pl}\,S_{vl}\,(p_i\text{-}p_{vl}) \quad (18)$$

The first term of the right-hand side of Equation (18) describes the fluid flux entering from the blood vessels and the second term the flux exiting through the lymphatic system. L_p is the blood vessels' hydraulic conductivity, and p_v is the vascular pressure. L_{pl}, S_{vl} and p_{vl} are the corresponding parameters for the lymphatic vessels [116].

Oxygen transport

The rate of change of oxygen concentration in the tissue was modeled with a convection diffusion equation that includes a source and a sink term [117,118]. The source term is due to oxygen supply from the blood vessels and the sink term describes oxygen consumption by cancer cells:

$$\frac{\partial c_{ox}}{\partial t} + \nabla\cdot\left(c_{ox}\mathbf{v^f}\right) = D_{ox}\,\nabla^2 c_{ox} - \frac{A_{ox}\,c_{ox}}{c_{ox} + k_{ox}}\,T_{cel} + P_{erox}\,S_v\,(c_{iox} - c_{ox}) \qquad (19)$$

where S_v is the vascular density, D_{ox} the oxygen diffusion coefficient, A_{ox} and k_{ox} are oxygen uptake parameters, c_{iox} is the oxygen concentration in the vessels, $\mathbf{v^f}$ is the fluid velocity and P_{erox} is the vascular permeability of oxygen defined as the oxygen diffusion coefficient divided by the length of the vessel wall.

Vascular density

Cancer cell infiltration was studied in our previews work [44]. Thus, in this study, we emphasize the anisotropic tumor growth governed by the effect of elastography data and how that affects stresses and the vasculature. The vascular density was considered as the vascular surface area, S, per unit volume,

$$S = \pi d L_{vw} N \qquad (20)$$

where d and L_{vw} are the diameter and length of the vessel and N is the number of vessels. By the assumption that the solid stresses do not affect the length or the number of vessels but only the diameter due to compression [82], and by dividing the vascular density with a reference vascular density

$$\frac{S_v}{S_{V0}} = \frac{\pi d L_{vw} N}{\pi do L_{vw} N} = \frac{d}{do} \tag{21}$$

The functional vascular density can be expressed as [82],

$$S_v = (d/do)\, S_{V0} \tag{22}$$

where S_{V0} is the vascular density of the host tissue and d/do is the degree of vessel compression assumed to be affected only by the solid stress levels, as described in [82]. The compression is assumed to be affected by the average bulk stress. The average bulk stress is expressed as the trace of the solid Cauchy stress. Initially, the vascular density was assumed to have the value of S_{V0} in both the tumor and host tissue. In the tumor region, due to the development of stresses, the degree of vessel compression d/do changes as the tumor grows and, thus S_v decreases in a stress-dependent manner.

Drug transport

Drug transport in the tumor interstitial space

The therapeutic agent can exist in three states: it can travel freely through the interstitial space (c_f) of the tumor, bind to cancer cells (c_b) and get internalized by the cells (c_{int}). The equations describing the three states are [119].

$$\frac{\partial c_f}{\partial t} + \nabla\cdot\left(c_f \mathbf{v^f}\right) = D_f \nabla^2 c_f + Q_{sta} - \frac{k_{on} c_e c_f}{\Phi} + k_{off} c_b \tag{23}$$

$$\frac{dc_b}{dt} = \frac{k_{on} c_e c_f}{\Phi} - k_{off} c_b - k_{int} c_b \tag{24}$$

$$\frac{dc_{int}}{dt} = k_{int} c_b. \tag{25}$$

The free drug that travels in the tumor interstitial space, c_f, can be transferred due to convection and diffusion, where D_f is the diffusion coefficient of the drug in the interstitial space and v^f is the fluid velocity. Moreover, the free drug is transferred across the tumor vessel wall (Q_{sta}). The remaining terms describe the binding, unbinding and internalization of the drug; c_e is the concentration of cell surface receptors and k_{on}, k_{off} and k_{int} are the

binding, unbinding and internalization rate constants, respectively; Φ is the volume fraction of cells accessible to the drug.

Drug transport across the tumor vessel wall: Starling's approximation

Starling's approximation was employed for the transport of drugs across the vessel walls

$$Q_{sta} = P_{er}S_V(C_{iv}\text{-}c_f) + L_pS_V(P_V\text{-}p_i)(1\text{-}\sigma_f)C_{iv} \quad (26)$$

where P_{er} is the vascular permeability of the drug, σ_f the reflection coefficient and C_{iv} is the vascular concentration of the drug expressed as a bolus injection:

$$C_{iv} = \exp(-(t-t_0)/k_d) \quad (27)$$

where t_0 is the time of drug injection and k_d the blood circulation decay. The parameters L_p, P_{er} and σ_f are expressed as a function of the vessel wall pores and the size of the drug [82,120]:

$$L_p = \frac{\gamma r_0^2}{8\eta L_{vw}} \quad (28)$$

$$P_{er} = \frac{\gamma H D_0}{L_{vw}} \quad (29)$$

$$\sigma_f = 1-W \quad (30)$$

where γ is the fraction of the vessel wall surface area occupied by pores, r_0 the pore radius, η the viscosity of blood plasma and L_{vw} the thickness of the vessel wall. H and W describe the steric and hydrodynamic interactions of the drug with the pores of the vessel wall that hinder diffusive and convective transport, respectively, and D_0 is the diffusion coefficient of a particle in free solution given by the Stokes–Einstein equation. By ignoring electrostatic interactions, H and W become [120],

$$H = \frac{6\pi F}{K_t} \quad (31)$$

$$W = \frac{F(2-F)K_s}{2K_t} \tag{32}$$

where F is the partition coefficient expressed as,

$$F = (1-\lambda)^2 \tag{33}$$

where λ is the ratio of the drug size to the vessel wall pore size and K_t and K_s are expressed as [120]

$$\binom{K_t}{K_s} = \frac{9}{4}\pi^2\sqrt{2}(1-\lambda)^{-5/2}\left[1 + \sum_{n=1}^{2}\binom{a_n}{b_n}(1-\lambda)^n\right] + \sum_{n=0}^{4}\binom{a_{n+3}}{b_{n+3}}\lambda^n \tag{34}$$

Solution of model equations

At all internal boundaries/interfaces of the computational domains, COMSOL automatically assigned continuity. For the calculation of the displacement fields and stresses, the external surfaces of the brain were considered to have a fixed boundary ($\mathbf{u} = 0$). For the transport equations, a no flux boundary condition was assumed at the external surface of the brain. The values of the model parameters are summarized in Table 10.

Results

Elastography data affect mechanical stress distribution and induce anisotropic tumor growth

We first set out to examine how the incorporation of elastography data by the model affects the magnitude and distribution of intratumoral mechanical stresses and the growth pattern of the tumor. Figure 6 illustrates the comparison of a tumor with a constant averaged shear modulus and a tumor based on the elastography data for isotropic growth, as well as the effect of anisotropic growth.

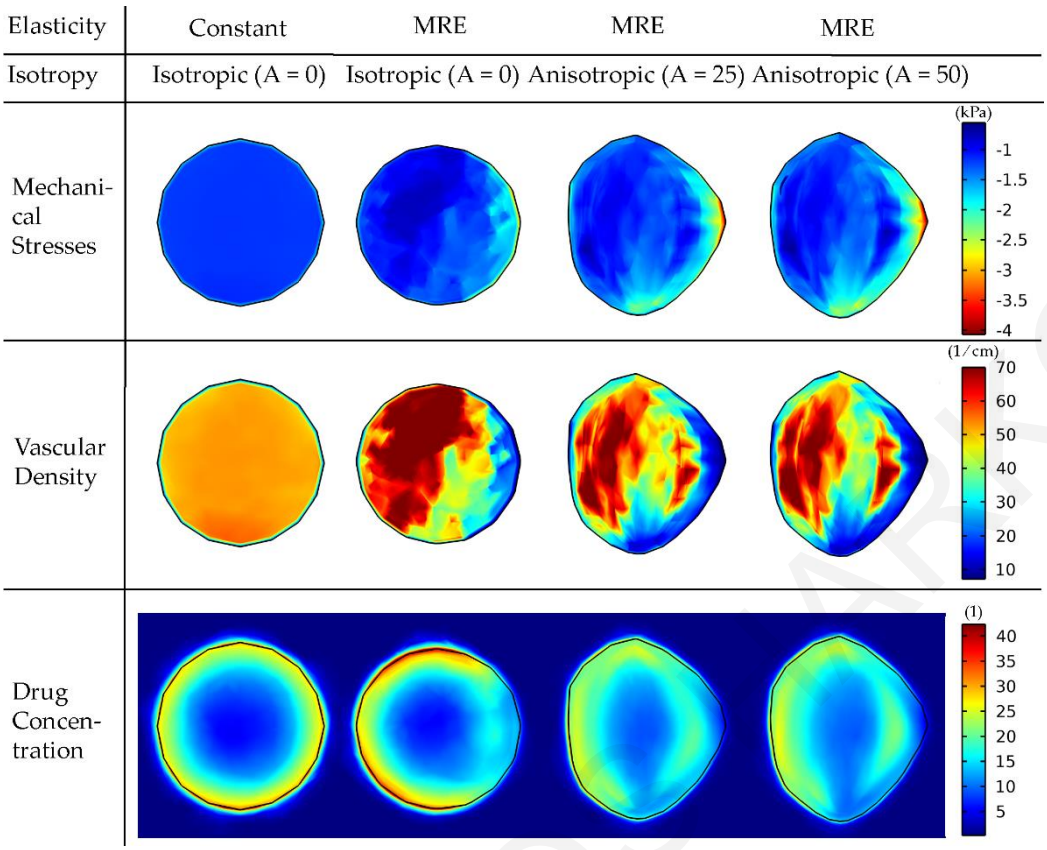

Figure 6: Mechanical stress, vascular density and drug concentration taken up by cancer cells for elastography data of patient 1. A cut plane at the center of the tumor is displayed to visualize the interior of the tumor. Results are presented at day 43 of the simulation. Comparison among isotropic and anisotropic tumor growth by varying the degree of anisotropy (A) is shown. For the constant elasticity case, the average value of the shear modulus was used in the tumor region and the average value of the normal brain for the rest of the brain. A drug of 2 nm in diameter was used to simulate small therapeutic molecules, whereas the tumor vessel wall pore size was set to 200 nm. The bulk mechanical stress is displayed (i.e., the trace of the stress tensor), and the negative sign denotes compression.

The incorporation of elastography data into the model results in a non-uniform distribution of mechanical stresses, which, in turn, affects the functional vascular density (due to vessel compression, Equation (22) and, thus, the distribution of the drug taken up by cancer cells. The non-uniform spatial distribution of the vasculature can be observed in Table 1 when comparing the standard deviation of the vasculature of the constant modulus case to that of the cases where MRE data were used. The constant case has a 2.6–2.7 times smaller standard deviation and, thus, a narrower variation in the vascular density values and a more uniform distribution. The standard deviation of the drug's spatial distribution in the constant modulus

case is higher compared to the MRE cases due to the lack of vessel compression at the periphery, where the highest drug transport is observed.

Table 1: Mean and standard deviation values of the spatial distribution of the vascular density and drug concentration in the tumor for the 4 cases considered in Figure 6.

		Constant-Isotropic (A = 0)	**MRE-Isotropic (A = 0)**	**MRE-Anisotropic (A = 25)**	**MRE-Anisotropic (A = 50)**
Vascular Density (1/cm)	Mean	50.263	47.560	46.933	45.524
	Standard Deviation	7.014	18.942	18.267	19.261
Drug Concentration	Mean	18.954	17.726	18.471	18.282
	Standard Deviation	6.292	5.970	4.436	4.723

Incorporation of anisotropic growth (i.e., $A > 0$) allows for the development of more realistic, non-spherical tumor shapes and growth towards the region of lower stresses. Interestingly, an increase in the anisotropic parameter, A, does not have a large effect on the shape of the tumor. The overlap of the tumor shapes is displayed in Figure 7. By evaluating the similarity with the Sorensen–Dice coefficient of the two anisotropic cases, we get a value of 0.9748. Therefore, it seems that the effect of elastography data on the model predictions is dominant compared to the effect of the degree of anisotropy.

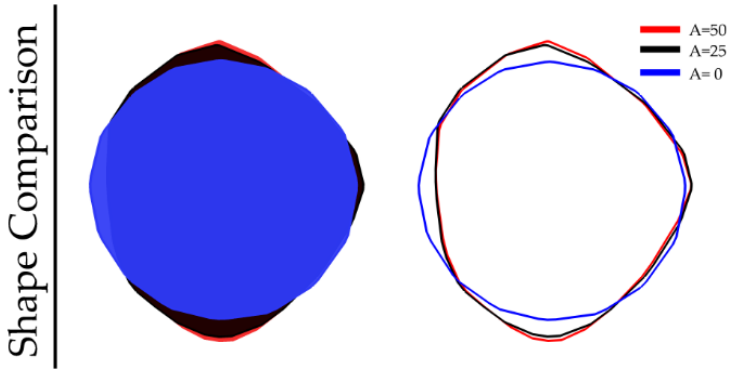

Figure 7: Overlap of the tumor shapes displayed in Figure 6 for the isotropic (A = 0) case and anisotropic (A = 25 and A = 50) cases.

Subsequently, we repeated the simulations using the MRE data of the other four patients (Figure 8), with each inducing a different stress distribution in the tumor, which, in turn, caused a different anisotropic tumor growth and, thus, different non-spherical tumor shapes.

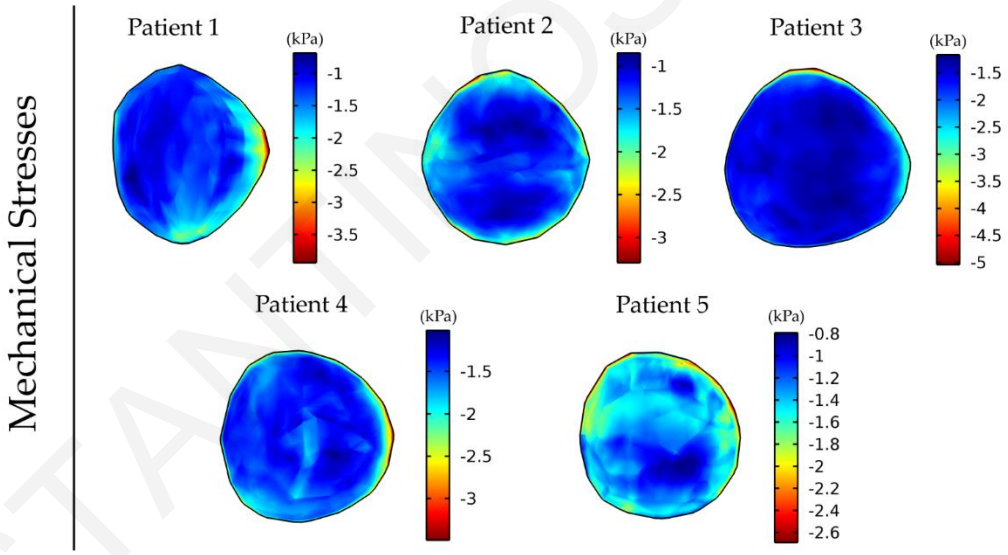

Figure 8: Distribution of intratumor mechanical stress at day 43 of the simulation for anisotropic tumor growth (A = 25). For the tumor region, the corresponding patient's elastography data were used, and elastography data for a healthy subject were used for the rest of the brain. The bulk stress (trace of the stress tensor) is presented, and the negative sign denotes tissue compression.

Elastography data reveal distinct functional vascular density distribution among patients

Vessel compression owing to mechanical stresses causes a reduction in the vessel diameter that limits the area of the lumen available for blood flow. This can have a detrimental effect on tumor perfusion and the functionality of the vessels as the higher the magnitude of stresses the more compressed the vessels become. Figure 9 shows the variation in the magnitude and distribution of the vascular density for the five different patient elastography datasets as a result of the differences in the intratumoral distribution of mechanical stresses (Figure 8). The mean and standard deviation values of the vascular density inside the tumor for the five patients can be found in Table 2.

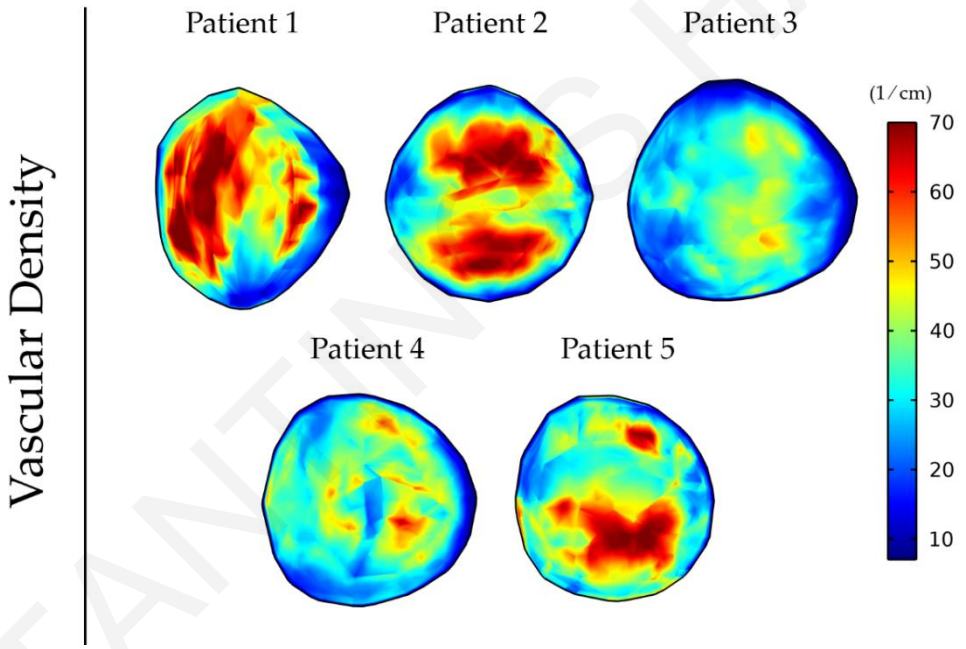

Figure 9: Vascular density at day 43 of the simulation for anisotropic tumor growth (A = 25) when incorporating the elastography data of the five patients.

Table 2: Mean values and standard deviation vascular density and drug concentration inside the tumor domain of the 5 patients at day 43 of the simulation.

		Patient 1	Patient 2	Patient 3	Patient 4	Patient 5
Vascular Density (1/cm)	**Mean**	46.933	40.110	29.515	32.882	38.723
	Standard Deviation	18.267	16.336	11.619	12.976	18.025
Drug Concentration	**Mean**	18.471	16.159	13.352	14.291	16.265
	Standard Deviation	4.436	4.080	4.361	3.229	4.932

Elastography data affect intratumoral drug distribution

Abnormal development of vessels during tumor-induced angiogenesis results in vessel hyper-permeability and openings in the tumor vessels wall that can be hundreds of nanometers large [121]. For larger vessel wall pores, the tumor interstitial fluid pressure is uniformly elevated and equals the vascular pressure owing to fluid communication between the vascular and extravascular space of the tumor (Figure 10) [18]. As a result, there is no pressure gradient across the tumor vessel wall nor inside the tumor. Furthermore, there is a steep pressure gradient at the periphery of the tumor as the fluid pressure drops from high values in the tumor interior to normal levels at the interface with the host tissue. For smaller pores in the vessel wall, the distribution of the interstitial fluid pressure is smoother and does not reach the value of the vascular pressure. These observations are well documented in the literature and are typical for the pathophysiology of solid tumors [9,10]. Our data suggest that the incorporation of MRE data does not change the magnitude and elevation of the interstitial fluid pressure.

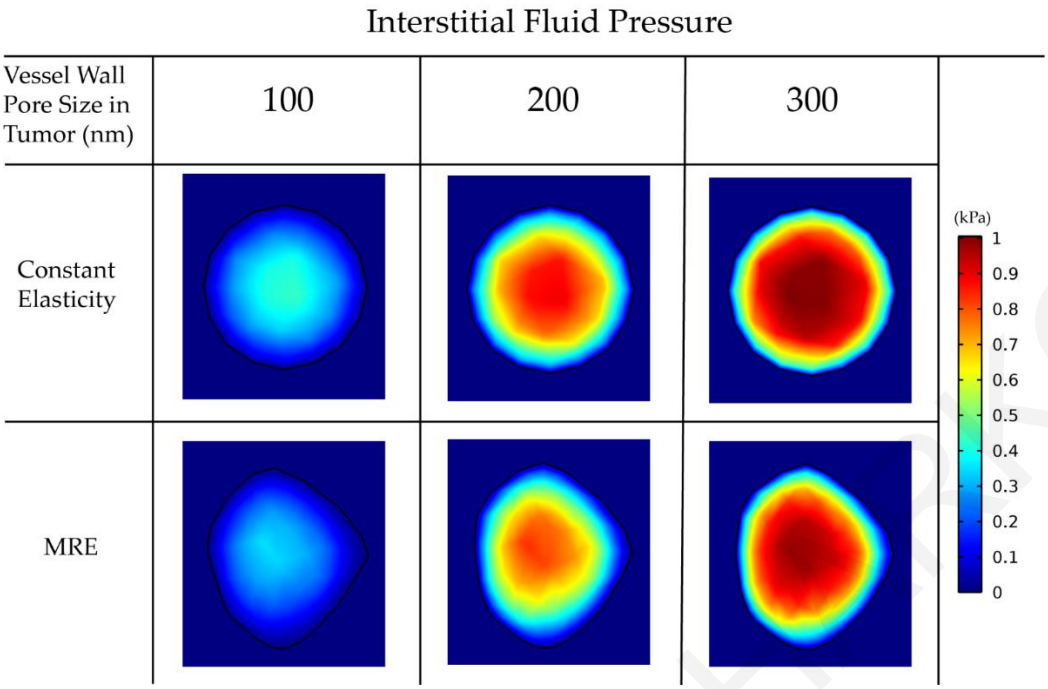

Figure 10: Interstitial fluid pressure for various vessel wall pore sizes. A comparison among the isotropic-constant elastic properties case and the anisotropic-elastography case (for patient 1) is shown.

For larger pores, the lack of pressure gradients eliminates drug transport through convection inside the tumor, and, thus, diffusion becomes the dominant transport mechanism (Equation(26)). Thus, the drug accumulates at the tumor periphery, where both convection and diffusion are prominent, and is washed out from the tumor to the host tissue (Figure 11).

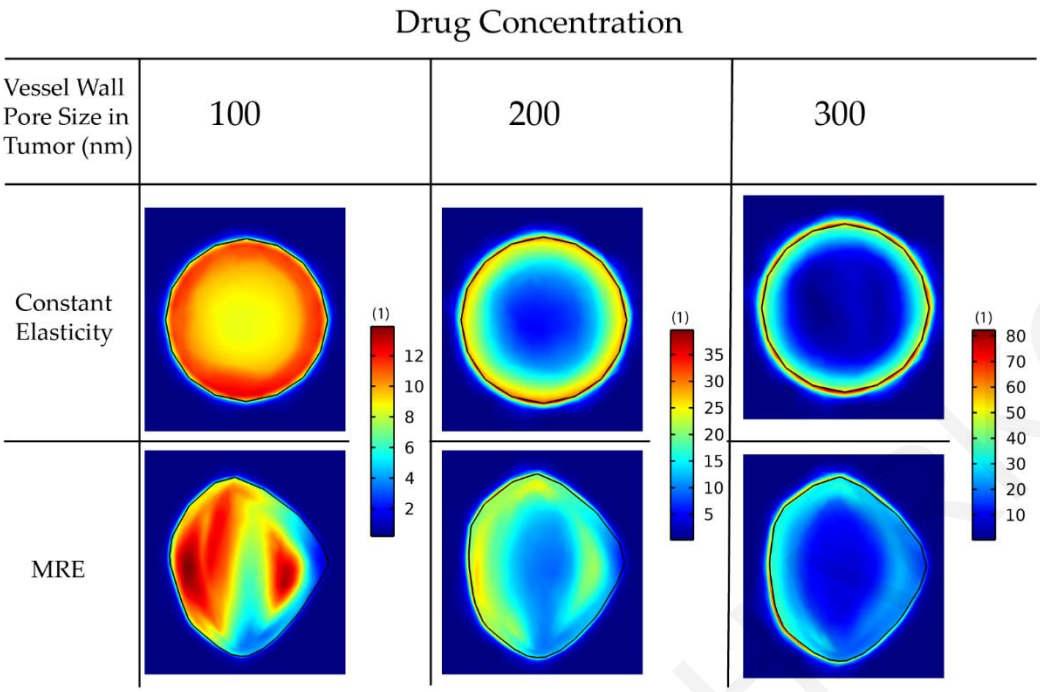

Figure 11: Drug concentration taken up by cancer cells for various wall pore sizes of the tumor vessels. A comparison between the isotropic-constant elastic properties case and the anisotropic-elastography case (patient 1) is shown. All results are displayed at day 43 of the simulation following a drug injection at day 41. The size of the drug is 2 nm.

In Table 3, we observe a decrease in the mean values and the standard deviation as we decrease the vessel wall pore size inside the tumor. That means that the establishment of a smooth pressure gradient for smaller vessel wall pore sizes resulted in a more uniform distribution of the drug inside the tumor.

Table 3: Mean and standard deviation values of the spatial distribution of drug concentration in the tumor for the 6 cases considered in Figure 11.

	Vessel Wall Pore Size in Tumor (nm)	**100**	**200**	**300**
Constant Elasticity Drug Concentration	**Mean**	10.185	18.954	24.223
	Standard Deviation	0.919	6.292	14.162
MRE Drug Concentration	**Mean**	9.361	18.282	23.736
	Standard Deviation	2.656	4.723	8.886

Importantly, incorporation of MRE data can affect model predictions of drug distribution independently of the size of the vessel walls (Figure 11). This is further observed by the mean and standard deviation of the spatial distribution of the drug in the constant versus the MRE cases (Table 3). The use of MRE data in the model leads to predictions of heterogeneous mechanical stress and vascular density distribution. Regions of lower functional vascular density exhibit reduced drug delivery, which results in a heterogenic distribution of the drug.

Next, we repeated the simulations for the delivery of drugs of different sizes: 2 nm, 70 nm and 150 nm, accounting for small molecules and for nanoparticles (Figure 12).

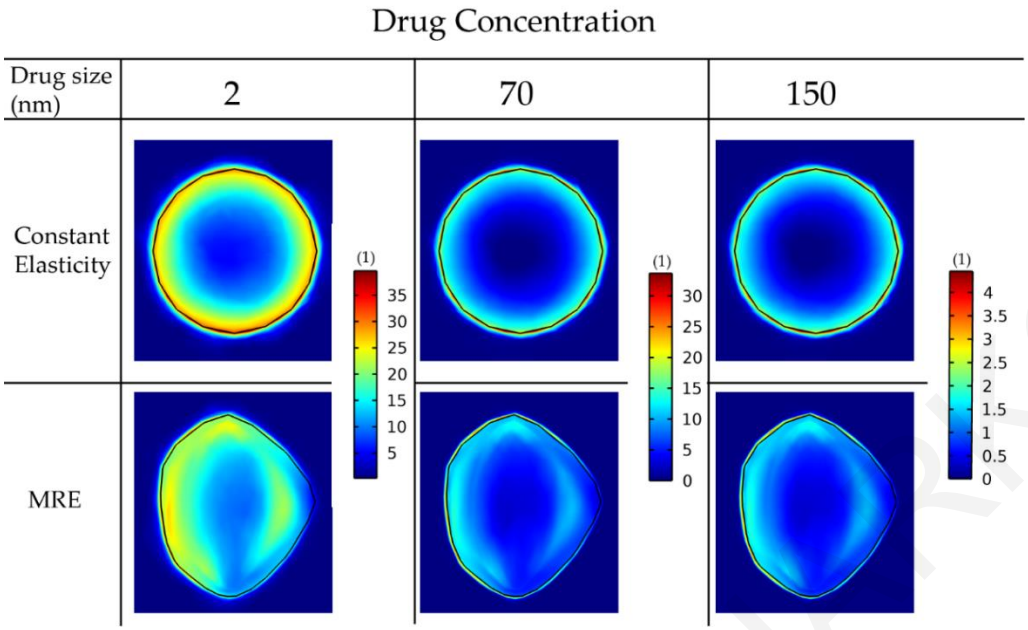

Figure 12: Drug concentration taken up by cancer cells for various drug sizes. A comparison among the isotropic-constant elastic properties case and the anisotropic-elastography case (patient 1) is shown. All results are displayed at day 43 of the simulation following a drug injection at day 41. The vessel wall pore size was set to 200 nm.

For the constant elastic properties scenario, the drug distribution is symmetric in the radial direction. This is not the case when the MRE data are included, in which regions of lower functional vascular density exhibit reduced drug delivery. The reduced drug delivery in the MRE cases can be further observed by the decrease in the standard deviation when comparing them with the corresponding constant elasticity values (Table 4). Moreover, smaller drugs can be transferred faster through the pores of the vessels and delivered in larger amounts to cancer cells. Alternative versions of Figure 11 and Figure 12 using the same colorbar for all the drug sizes can be found in Figure 13 and Figure 14.

Table 4: Mean and standard deviation values of the drug concentration inside the tumor domain of the 6 cases of Figure 12.

	Drug Size (nm)	2	70	150
Constant Elasticity Drug Concentration	**Mean**	18.954	9.221	1.201
	Standard Deviation	6.292	4.413	0.575
MRE Drug Concentration	**Mean**	18.282	8.957	1.185
	Standard Deviation	4.723	3.114	0.413

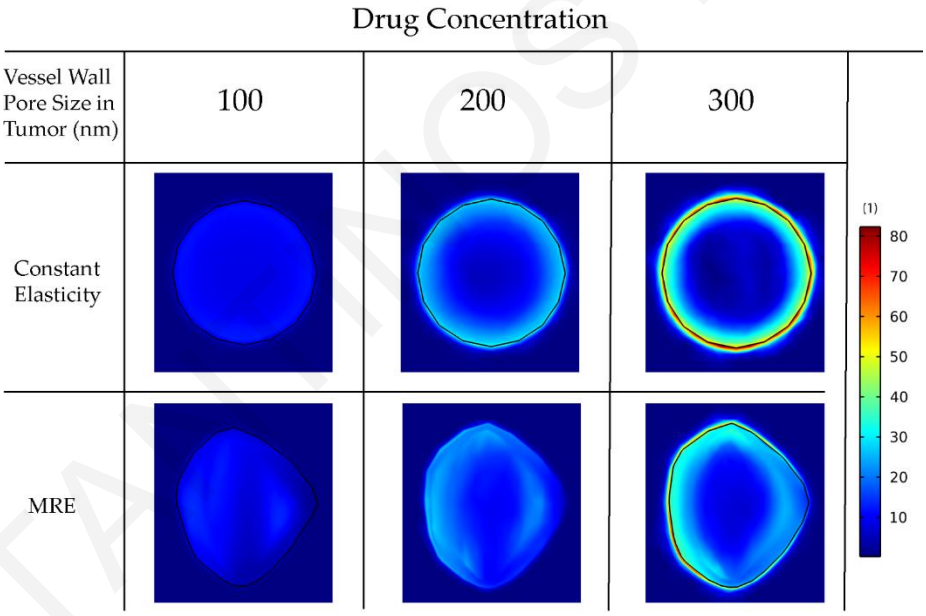

Figure 13: Second version of Figure 11 where the same colorbar was used for all figures.

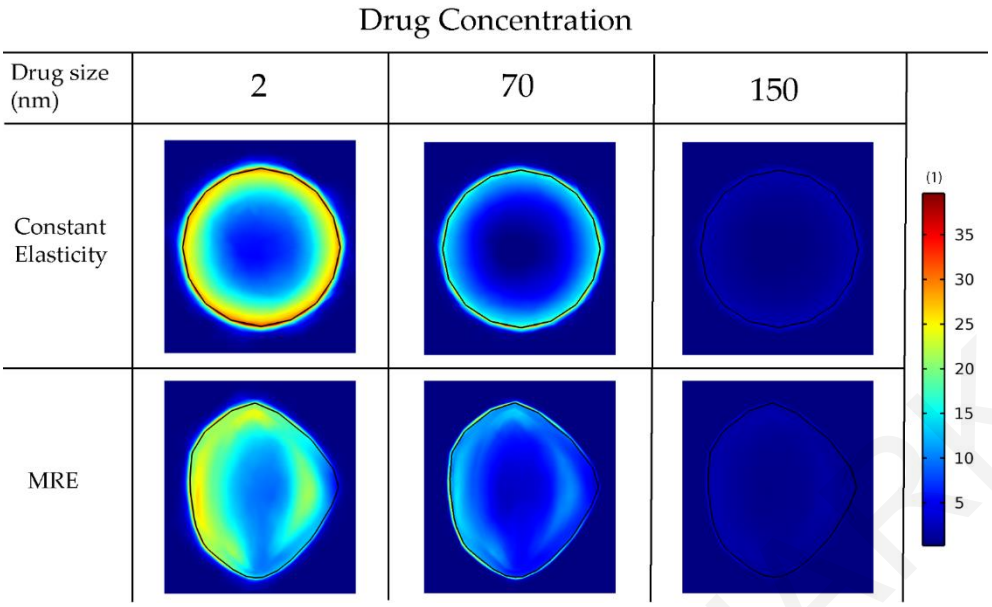

Figure 14: Second version of Figure 12 where the same colorbar was used for all figures.

Finally, we employed the elastography data of all the patients to investigate the different patterns of drug delivery within patients (Figure 15).

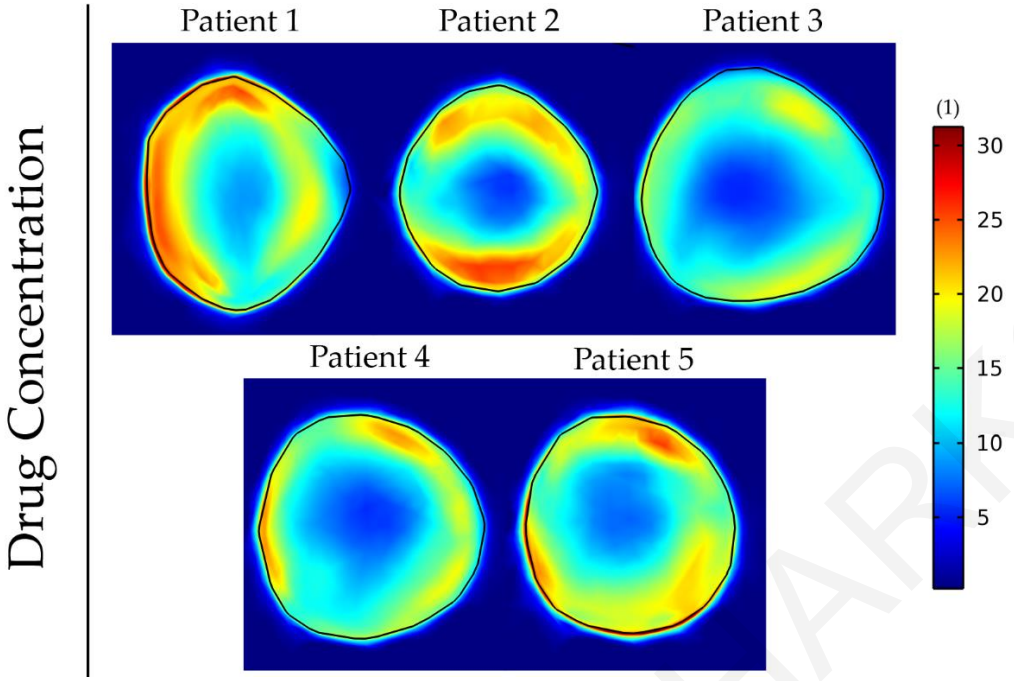

Figure 15: Drug concentration taken up by cancer cells at day 43 of the simulation for anisotropic tumor growth (A = 25). All results are displayed at day 43 of the simulations following a drug administration at day 41. The size of the drug is 2 nm, and the vessel wall pore size was set to 200 nm.

The results show that the incorporation of patient-specific elastography data can affect the delivery and intratumoral distribution of the drugs. Regions of lower functional vascular density vary among patients, and this results in a distinct drug distribution for each patient. To compare these five cases, we evaluated the fraction of the tumor that receives a drug concentration greater than a specific value (Table 5). This fraction varies by more than 10-fold among the patients. The analysis was also repeated for the cases displayed in Figure 11 and Figure 12 and can be found in Table 6 and Table 7, respectively. These results further support that tumor elastic properties can affect drug delivery.

Table 5: Fraction of the tumorthat receives a drug concentration greater than 20 (dimensionless units) for the 5 patients at day 43 of the simulation.

	Patient 1	Patient 2	Patient 3	Patient 4	Patient 5
Volume Fraction (Drug Concentration > 20)	0.375	0.173	0.027	0.038	0.206

Table 6: Fraction of the tumor that receives drug concentration greater than 20 for the 6 cases of Figure 11.

	Vessel Wall Pore Size in Tumor (nm)	100	200	300
Volume Fraction (Drug Concentration > 20)	**Constant Elasticity**	0	0.464	0.560
	MRE	0	0.373	0.666

Table 7: Fraction of the tumor that receives drug concentration greater than 20 for the 6 cases of Figure 12.

	Drug Size (nm)	2	70	150
Volume Fraction (Drug Concentration > 20)	**Constant Elasticity**	0.464	0.001	0
	MRE	0.373	0.002	0

Discussion

The important role of mechanical forces in tumor progression and therapy is well established [5–8,18,74,75,82]. Yet, the incorporation of tissue mechanics in mathematical models of brain tumors is not thoroughly studied. Here, we developed a methodology for more accurate calculation of brain tumor mechanics and highlighted its importance for vascular changes and the delivery of therapeutic agents. We included MRE data for a more realistic incorporation of the mechanical properties of both the tumor and host tissue, which led to a more accurate calculation of the intratumoral distribution of mechanical stresses. In addition, to further improve the accuracy of our calculations, we applied a methodology for anisotropic tumor growth, allowing the tumor to grow in non-spherical shapes. We considered that mechanical stresses induce vessel compression and modeled the delivery of drugs of various sizes.

The incorporation of elastography data resulted in a non-uniform distribution of mechanical stresses. The incorporation of anisotropic growth allowed the development of a more realistic non-spherical tumor shape and growth towards the regions of lower stresses. The non-uniform mechanical stresses induced a non-uniform distribution of vascular density due to vessel compression. This resulted in a non-symmetric distribution of drugs where regions of lower functional vascular density exhibited reduced drug delivery. Stress distribution, vascular density distribution and drug delivery are unique for each patient's MRE data, and, thus, the inclusion of MRE data allows patient-specific predictions.

Smaller pores of the vessel wall induced a smoother distribution of interstitial fluid pressure. The incorporation of MRE data did not change the magnitude and elevation of interstitial fluid pressure. Smoother pressure gradients caused a more uniform distribution of drug inside the tumor. In addition, our results suggest that smaller drugs can be transferred faster through the pores of the vessels and delivered in larger amounts to the cells compared to larger drugs. Overall, our findings can be used to improve treatment response assessment and evaluation of pharmacological strategies as MRE is a noninvasive imaging technique that can be added to patients' MR examination. MRE is an emerging imaging technique that has been used in several studies of patients with brain tumors [122]. Currently, there is no commercial system available for brain MRE, limiting its potential as a routine part of brain cancer imaging. The patients in our study were all imaged prior to any treatment, but using

MRE on patients after surgical tumor resection is clinically feasible and currently ongoing at our institution as part of a clinical trial and with minimal implications (NCT03951142).

Several simplifying assumptions were made in this study. For the host tissue, elastography data of a healthy subject were used because the clinical patient scans did not cover the entire brain, only 4.65 cm, covering the tumor. Because the patients differ from healthy subjects in terms of MRE values [99], more accurate results would have been obtained if the specific patient's elastography of the host tissue was used. In addition, patients' MRE values were obtained at one time point during tumor development and, thus, in the model, the elastic properties were assumed constant during tumor progression. That is not usually the case. Due to changes in the cellular and extracellular matrix components, the compression of the tumor and the host tissue changes during tumor progression. These effects can result in changes in the stiffness of the tumor [8,74,123,124]. The incorporation of temporal variations in the elastic properties would be expected to change our results quantitatively. However, the main conclusions of our study concerning the role of mechanical forces in tumor vasculature and drug delivery are not expected to be altered by this. Moreover, the timepoint of the injection of chemotherapy was also an assumption. The same timepoint of injection was used for all the cases to enable direct comparison among different simulations. Additionally, although a larger number of patients could have improved our model predictions, with the use of 5 patents we were able to identify interpatient variations in model predictions due to the different material properties from each patient. Finally, the isotopic neo-Hookean constitutive equation might not be sufficient to fully describe the mechanical response of brain tumors because of the heterogenous structure of the GBM. However, studies have shown that the state of stress of the tumor is largely determined by the properties of the host and tumor tissue and not from the selection of the constitutive equation being used [6].

In conclusion, the presented methodology and results led to the conclusion that incorporating the tissue elastic properties assessed by MRE and anisotropic growth into mathematical models can result in more accurate predictions of the distribution of mechanical stresses in tumors. This produces an improved mathematical description of subsequent events that are closely related to the development of mechanical stresses, including the heterogeneity in the

functional vasculature of the tumor and intrapatient variations in tumor perfusion and delivery of drugs.

Chapter 3: Mathematical modeling of intratumoral immunotherapy yields strategies to improve the treatment outcomes

This study has been published in the journal PLOS Computational Biology: Harkos C, Stylianopoulos T, Jain RK. Mathematical modeling of intratumoral immunotherapy yields strategies to improve the treatment outcomes. PLOS Computational Biology. 2023;19: e1011740. https://doi.org/10.1371/journal.pcbi.1011740

Summary

Intratumoral injection of immunotherapy aims to maximize its activity within the tumor. However, cytokines are cleared via tumor vessels and escape from the tumor periphery into the host-tissue, reducing efficacy and causing toxicity. Thus, understanding the determinants of the tumor and immune response to intratumoral immunotherapy should lead to better treatment outcomes. In this chapter, we developed a mechanistic mathematical model to determine the efficacy of intratumorally-injected conjugated-cytokines, accounting for properties of the tumor microenvironment and the conjugated-cytokines. The model explicitly incorporates i) the tumor vascular density and permeability and the tumor hydraulic conductivity, ii) conjugated-cytokines size and binding affinity as well as their clearance via the blood vessels and the surrounding tissue, and iii) immune cells - cancer cells interactions. Model simulations show how the properties of the tumor and of the conjugated-cytokines determine treatment outcomes and how selection of proper parameters can optimize therapy. A high tumor tissue hydraulic permeability allows for the uniform distribution of the cytokines into the tumor, whereas uniform tumor perfusion is required for sufficient access and activation of immune cells. The permeability of the tumor vessels affects the blood clearance of the cytokines and optimal values depend on the size of the conjugates. A size >5 nm in radius was found to be optimal, whereas the binding of conjugates should be high enough to prevent clearance from the tumor into the surrounding tissue. In conclusion, development of strategies to improve vessel perfusion and tissue hydraulic conductivity by reprogramming the microenvironment along with optimal design of conjugated-cytokines can enhance intratumoral immunotherapy.

Introduction

ICIs have transformed the treatment of cancer. To date 8 different ICIs have been approved alone or in combination with other therapies for ~80 indications [19]. However, less than 20% of patients currently benefit from these treatments [23]. Moreover, many patients develop immune-related adverse events, some of which can be fatal [24]. The abnormal and immunosuppressive TME not only hinders the delivery of ICIs, but also renders them ineffective once they accrue in tumors [125]. One approach to overcome these challenges is to normalize the tumor vasculature and microenvironment using anti-angiogenic agents [126]. Indeed 7 different combinations of ICIs and anti-angiogenic agents have been approved by the US FDA recently and multiple trials are currently testing this approach [127,128]. Another approach to improve the outcome of immunotherapies is the direct injection of immunostimulatory agents, tethered to a polymer or another substrate, into the tumor [129–131]. Agents being evaluated for this purpose include pro-inflammatory cytokines, such as, IL2 and IL12 [132–134].

The goal of intratumoral injection of pro-inflammatory cytokines is to maximize their activity within the tumor while minimizing systemic exposure. After the cytokines are administered intratumorally, they can be cleared via the tumor-associated vasculature and the lymphatic system as well as escape from the tumor margin into the surrounding host tissue, resulting in potentially toxic levels in the circulation and the host organ [135–137]. A promising approach to increase tumor exposure and reduce adverse effects to normal tissues, is controlled release of cytokines from a polymer-conjugate injected into a tumor. One example of this approach is to fuse cytokines to collagen binding proteins, so that they are bound to collagen fibers within the tumor and do not clear rapidly from the tumor margin or by the vasculature. This strategy has been successful in enhancing treatment efficacy in preclinical studies [21,22,138]. Apart from the binding properties of the cytokine agent, its local exposure depends also on properties of the TME [1,2,139–141]. Specifically, the uniformly elevated IFP within the tumors (resulting from vascular hyperpermeability and dysfunctional lymphatics) decreases to normal values at the tumor-host tissue margin, causing steep pressure gradients at the tumor periphery and resulting in fluid flux from the tumor into the surrounding tissue. This can wash out the injected cytokines and reduce their concentration in the tumor region [1,2,139–141]. In addition, the hyper-permeability of

tumor vessels might lead to the intravasation of the conjugated-cytokines into the vessels and their clearance via the circulation, a process that depends not only on the pore size of the vessel walls but also on the size, charge, configuration, and binding characteristics of the conjugated-cytokines [142–144]. Despite their importance in the effectiveness of intratumoral injection of cytokines, the role of these tumor parameters (i.e., vessel permeability, hydraulic conductivity, vessel density) and properties of the conjugated-cytokines (i.e., binding affinity, size) and their effects on the efficacy of intratumor injection of cytokines remain unexplored.

We have previously developed mathematical models of fluid and solute transport in tumors to investigate the role of vascular permeability, diffusion coefficient and hydraulic conductivity, binding and metabolism, interstitial fluid pressure, solid stresses as well as lymphatics [1,11–13,42,45]. Other *in silico* studies have examined the interactions of immune cells with cancer [145,146]. In addition, a recent intratumoral injection model examined the optimal cytokine design that increases intratumoral activity [22]. Although this model incorporated the binding-affinity of the conjugated-cytokines to their target, their transport into the blood circulation accounting for the conjugated-cytokines size and affinity, as well as temporal changes in model variables, they did not account for pathophysiological features and the spatial heterogeneity of the TME and the surrounding host tissue. To this end, building on our previous work, here we developed a mathematical model for intratumoral injection of conjugated-cytokines that accounts for i) spatiotemporal variations in model parameters, ii) the vascular and lymphatic function, iii) the hydraulic conductivity of the tumor and host tissue, iv) the interstitial fluid pressure, v) convection and diffusion within the tumor, from the tumor interstitial space to the blood vessels and the surrounding tissue, accounting explicitly for the size of the conjugated-cytokines, their binding affinity and vascular permeability, and vi) immune cells and cancer cells interactions. Two conjugated-cytokines cases were modeled: i) cytokines fused with mouse serum albumin (MSA) conjugated to the collagen binding protein, lumican [21], and ii) cytokines bound to aluminium hydroxide (alum) via ligand exchange between hydroxyls on the surface of alum and phosphoserine residues tagged to the cytokine by an alum-binding peptide [20]. We first assessed the robustness of our model by comparing model predictions with tumor growth data from these two independent studies [20,21]. Subsequently, we used the model to investigate the effect of the conjugated-cytokines size and binding affinity in conjunction

with properties of the TME, on the efficacy of intratumorally injected conjugated-cytokines in reducing tumor growth. We further analyzed spatiotemporal changes in the concentration of the conjugated-cytokines and immune cells for a better understanding of the underlying mechanisms.

Materials and methods

The modeling framework consists of two steps. We first model the short time period immediately after the injection of the conjugated-cytokines from the needle into the tumor. Then, after the removal of the injection needle, we model the transport of the conjugated-cytokines into the tumor, its clearance through the blood vessels and tumor margin, as well as the growth of the tumor over a long time period. The first model simulates the injection of conjugated-cytokines inside a spherical tumor surrounded by host tissue (Figure 16 and Figure 17). The conjugated-cytokine concentration profiles developed after the injection from the needle are used as initial conditions for the second model. The second model simulates cancer cell proliferation, the immune response and tumor growth for melanoma and fibrosarcoma tumors (Figure 16 and Figure 18). The model also accounts for transport of fluid and cytokines within the tumor, between the tumor and the host tissue as well as across the tumor vessel walls (Figure 16a). The model was developed and solved in COMSOL Multiphysics (COMSOL, Inc., Burlington, MA, USA) using the finite element method.

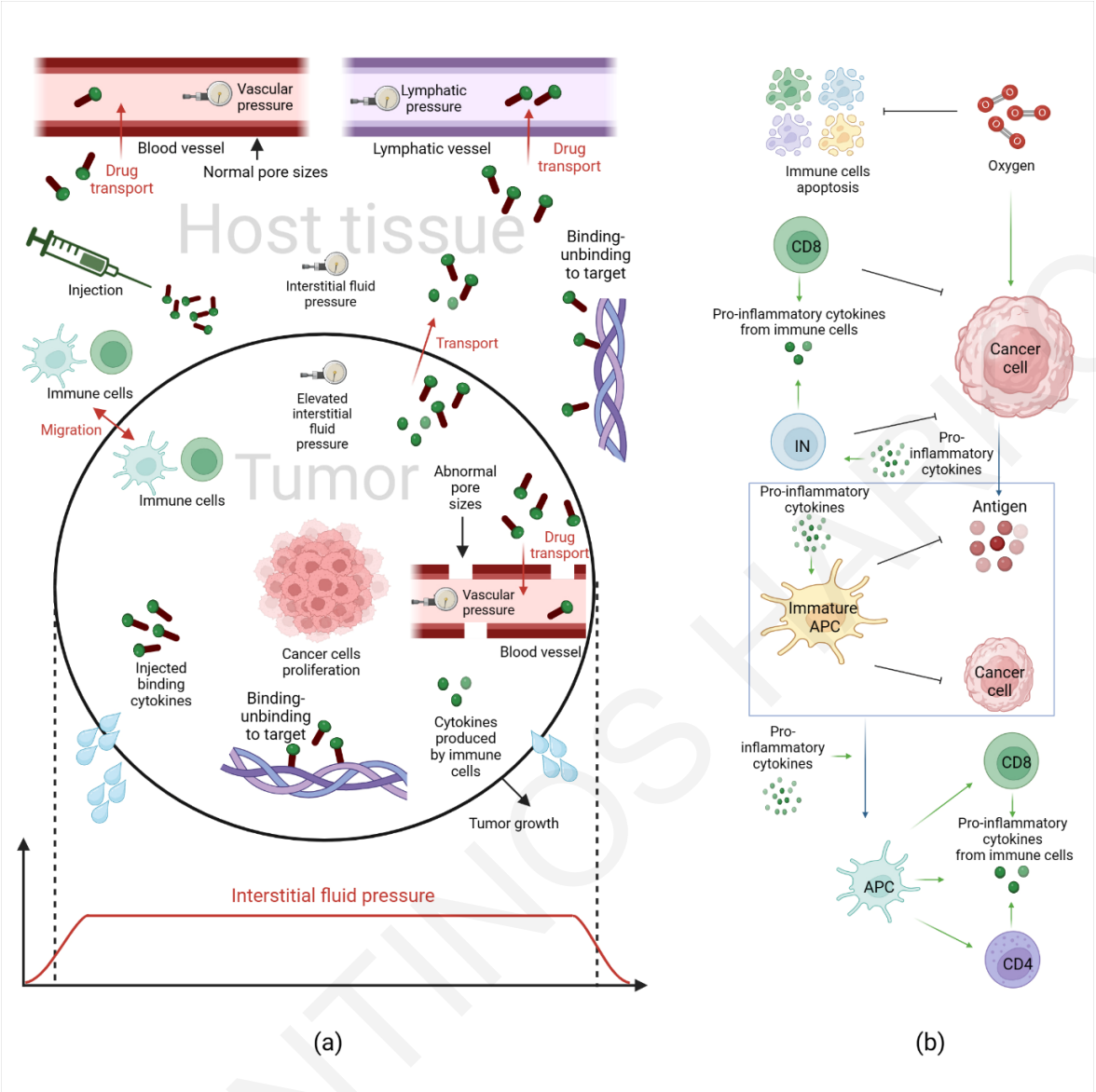

Figure 16: Model methodology. (a) Shcematic of various transport mechanisms considered in the model. The conjugated-cytokines are injected in the tumor region and can be transported via convection and diffusion to the host tissue and across the tumor vessel walls. Hyperpermeability of the tumor blood vessels and the lack of functional lymphatic vessels elevates interstitial fluid pressuse, inducing pressure gradients at the tumor periphery that drive transport of the conjugated-cytokines from the tumor to the host tissue via convection. The injected conjugated-cytokines can bind and unbind to the target (e.g., collagen fibers) in both tumor and host tissue. Cytokines produced by the immune cells can disperse via convection and difusion as well. Also immune cells can migrate (i.e., diffuse) from the tumor tissue to the host tissue and the reverse depending on the concentration gradients. (b) Model components of the immune system: IN represents the innate immune cells that induce cytolysis and produce antigen, e.g., Natural Killer cells. Immature APCs are the immature antigen presenting cells that can become antigen presenting cells (APCs). CD4 and CD8 represent effector CD4+ and CD8+ T cells. Production and

activation of immune cells are affected by cytokines. The immune cells also produce cytokines. Oxygen supply increases cancer cells' proliferation and tumor growth and decreases the apoptosis rate of the immune cells. Created with BioRender.com

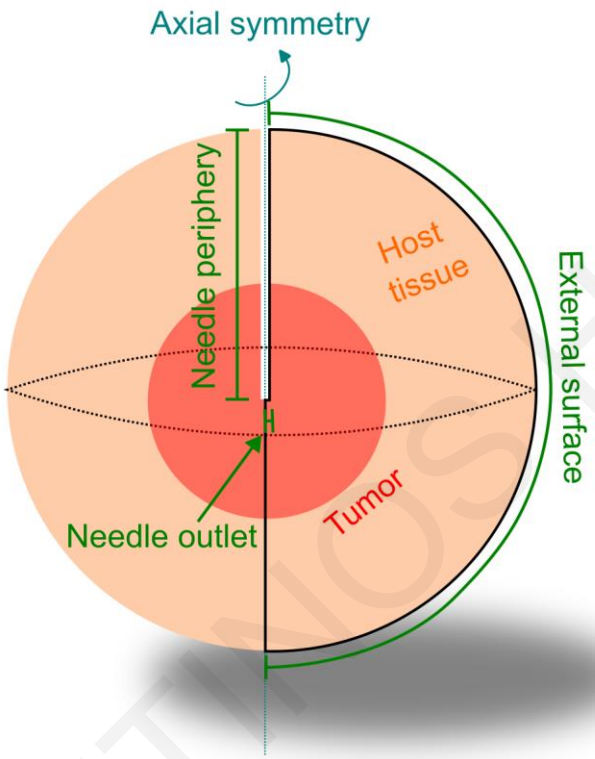

Figure 17: Computational domain with axial symmetry. The domain includes the tumor region and the host tissue. The needle reaches the center of a spherical tumor.

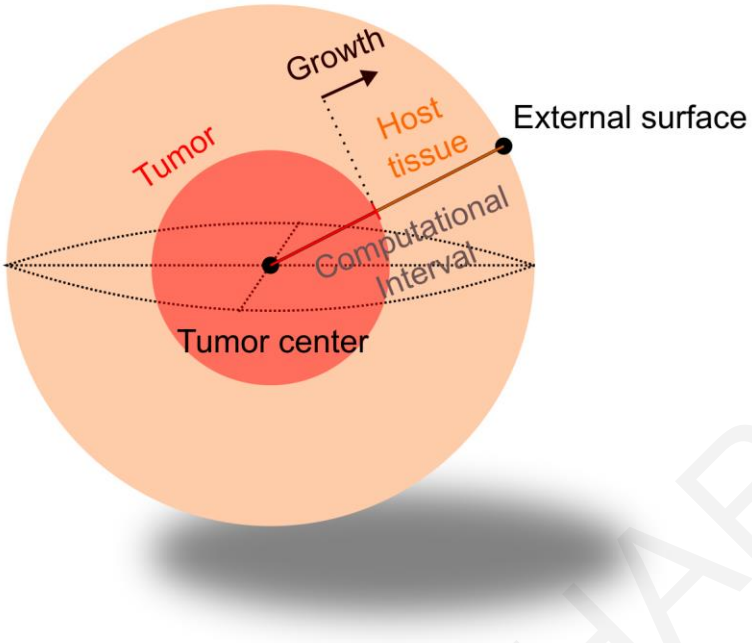

Figure 18: Computational domain with spherical symmetry. The interval includes the tumor region and the host tissue. The 1D tumor interval forms a 3D spherical tumor. The tumor grows as a sphere and deforms the host tissue.

Cytokine transport

The conjugated-cytokines can be in a free state or bound to the target (bound state). Both convection and diffusion are considered for the transport of the free conjugated-cytokines within the tumor and the host region. The diffusion coefficient of the conjugated-cytokines are determined by experimental data based on the conjugate size [147]. Also, the conjugated-cytokines that are not bound can intravasate into the vessels through diffusion and convection based on Starling's approximation for mass transfer [11,45,148]. The transport properties of the conjugated-cytokines across the tumor vessel wall (i.e., vascular permeability and reflection coefficient) are determined explicitly by the relative ratio of the conjugate size to the size of the pores of the vessel wall, so that we can account for tumors with low, moderately, and highly permeable vessels as well as for conjugated-cytokines of varying size. For each conjugated-cytokine case, cytokines fused with mouse serum albumin conjugated to lumican and cytokines bound to aluminium hydroxide, the molecular weight were taken from the respective study [20,21] to determine their diffusion coefficient and

transport properties across the tumor vessel walls. The rate of clearance from blood was also determined by the conjugate size based on previous work [149]. Furthermore, due to the different conjugate design and the different nature of target (collagen vs alum) for each conjugated-cytokine case, the respective binding affinity was used. In addition to cancer cells, the model includes innate and adaptive immune cells. These cells produce pro-inflammatory cytokines in addition to the injected cytokine, so that the total population of pro-inflammatory cytokines includes the cytokines produced by the immune system, the injected conjugated-cytokines that are free to move and the injected conjugated-cytokines that are bound. The total pro-inflammatory cytokines can enhance the immune system's response to kill cancer cells and reduce tumor growth. The types of immune cells and immune cell – cancer cell interactions considered in our model are shown in Figure 16b and described below.

Immune response

The simulation starts with a highly immunosuppressed TME by assuming initially no antigen presenting cells (APCs) or activated effector cells (e.g., effector CD4+ and CD8+ T cells), and predicts how the function of immune cells with positive effect on killing cancer cells impacts tumor growth. Due to the complex nature of the immune system and the immune cells - cancer cells interactions, we considered the immune cells in certain categories for simplicity. These include innate and adaptive immune cells. The innate cells are divided into two categories: cells that can induce cytolysis, such as Natural Killer (NK) cells, this category of cells can kill cancer cells and produce antigen, and the immature antigen presenting cells (IAPCs) that includes the dendritic cells and a sub-set of macrophages. When IAPCs interact with cancer cells or antigens they become APCs. The higher the number of APCs the more CD4+ and CD8+ T cells will reach the tumor and host tissue. In addition, and for simplicity, we did not include an explicit model of lymph nodes for the activation of T cells. Instead, we assumed that T cell activation takes place external to the tumor in lymph nodes where the T cells encounter APCs, but the activated T cells return to the same location in the tumor from which the APCs depart. Effector CD8+ T cells kill cancer cells and further increase the concentration of antigens in the region. Both CD4+ and CD8+ T cells produce pro-inflammatory cytokines to further increase the immune response (Figure 16b).

Interstitial fluid flow

Fluid flow within the tumor and host tissue is governed by Darcy's law, taking into account the displacement of both the tumor and the surrounding normal tissue due to the growth of the tumor. Continuity of fluid velocity and fluid flux is applied at the tumor/host tissue interface [11]. The model also accounts for fluid flux across the tumor vessel walls based on Starling's approximation [2,11,41,150]. The hydraulic conductivity of the tumor vessel wall is calculated based on the vessel walls pore size, following our previous research [41,45].

Oxygen transport

The model considers oxygen transport from the vessels into the tumor and host tissue and transport within the tissue. Overall tumor growth depends on cancer cell number (concentration), which is determined by cancer cell proliferation (as a function of tissue oxygenation) and cancer cell killing by immune cells [151,152]. Details about the model variables as well as the baseline and initial values of the model parameters are given in

Table 11 and Table 12.

Modeling of intratumoral injection

The model equations are solved using COMSOL Multiphysics (COMSOL, Inc. Burlington, MA, USA). At the tumor center, the initial cancer cell density was assumed to have its peak value and then it decreases alongside the straight line due to a step function. The domain above a threshold cancer cell density is assumed as the tumor region and below that, the host tissue.

The parameters change from their abnormal-tumor value to their normal value as a function of the cancer cell density. The values change at the threshold cancer cell density using a step function. The step functions are used to certify continuity of the model variables. A 2D geometry with axial symmetry was modeled. The geometry includes the tumor, the host tissue and a 28 gauge needle reaching the tumor center. Conjugated-cytokines are injected from the needle outlet. Flux source was assumed for the needle outlet and no flux for the needle periphery.

Interstitial pressure-fluid velocity

Normal and tumor tissues have properties similar to those of a porous medium. Brinkman's equation describes the flow in porous medium in cases where the velocity gradients are non-negligible and reads:

$$\frac{\rho}{\epsilon_p}\frac{\partial \mathbf{v^f}}{\partial t} = -\nabla p_i + \nabla \cdot \left[\frac{\mu}{\epsilon_p}\left(\nabla \mathbf{v^f} + (\nabla \mathbf{v^f})^{\tau}\right) - \frac{2}{3}\frac{\mu}{\epsilon_p}(\nabla \cdot \mathbf{v^f})\mathbf{I}\right] - \left(\frac{1}{k_{th}} + \frac{Q_m}{\epsilon_p^2}\right)\mathbf{v^f} \quad (35)$$

Where μ is the dynamic viscosity, ρ is the density, p_i is the interstitial pressure, v^f is the fluid velocity and k_{th} is the hydraulic conductivity of the interstitial space [113]. For incompressible fluid flow the conservation of mass reads:

$$\rho \nabla \cdot \mathbf{v^f} = Q_m \quad (36)$$

$$Q_m = \rho\left(L_p S_v(p_v - p_i) - L_{pl} S_{vl}(p_i - p_{vl})\right) \quad (37)$$

Where the first term of Q_m describes the fluid flux entering from the blood vessels and the second term the flux exiting through the lymphatic system. L_p is the blood vessels' hydraulic conductivity, and p_v is the vascular pressure. L_{pl}, S_{vl} and p_{vl} are the corresponding parameters for the lymphatic vessels [116].

Intratumorally injected conjugated-cytokines

$$\frac{\partial Ic_f}{\partial t} + \nabla \cdot \left(-D_{Ic_f}\nabla \mathbf{Ic_f} + \mathbf{v^f} Ic_f\right) = -\frac{k_{on} c_e Ic_f}{\Phi} + k_{off} Ic_b + Q_{Ic} \quad (38)$$

$$\frac{dIc_b}{\partial t} = \frac{k_{on} c_e Ic_f}{\Phi} - k_{off} Ic_b \quad (39)$$

The free conjugated-cytokines that travel in the tumor interstitial space, Ic_f, can be transferred due to convection and diffusion, where D_{Ic_f} is the diffusion coefficient of the drug in the interstitial space and v^f is the fluid velocity. Moreover, the free conjugated-cytokines are transferred across the tumor blood vessel and lymphatic vessel wall (Q_{Ic}). The remaining terms describe the binding and unbinding of the conjugated-cytokines: c_e is the

concentration of collagen, k_{on}, k_{off} are the binding and unbinding rate constants, respectively and Φ is the volume fraction [153].

Conjugated-cytokines in the blood compartment

The injected conjugated-cytokines concentration in the blood is described as,

$$\frac{dIc_{blood}}{dt} = \frac{\iiint_V - Q_{Ic} dV_{dom}}{V_{blood}} - \delta_{clear} Ic_{blood} \quad (40)$$

Where $\iiint_V - Q_{Ic} dV_{dom}$ is the total rate of mass of the agonist that can be transported from the tumor and host tissue to the blood. Q_{Ic} is the mass rate at each point of the tumor and host tissue domain and is integrated for the calculation of the total mass rate leaving from the tumor and host tissue. V_{blood} is the volume of blood and δ_{clear} the rate of clearance from blood.

Transport from tumor and host tissue to blood

Transport across the vessel and lymphatic vessel wall based on Starling's approximation:

$$Q_{Ic} = P_{er} S_v (Ic_{blood} - Ic_f) + L_p S_v (p_v - p_i)(1 - \sigma_f) Ic_{blood} - \delta_{Ic_f} Ic_f \quad (41)$$

where P_{er} is the vascular permeability of the conjugated-cytokines, σ_f the reflection coefficient and δ_{Ic_f} the rate constant that describes the rate in which the conjugated-cytokines exit through the lymphatic vessels.The parameters L_p, P_{er} and σ_f are expressed as a function of the vessel wall pores and the size of the conjugated-cytokines [82,120] :

$$L_p = \frac{\gamma r_0^2}{8 \mu L_{vw}} \quad (42)$$

$$P_{er} = \frac{\gamma H D_0}{L_{vw}} \quad (43)$$

$$\sigma_f = 1 - W \quad (44)$$

where γ is the fraction of the vessel wall surface area occupied by pores, r_0 the pore radius, μ the viscosity and L_{vw} the thickness of the vessel wall. H and W describe the steric and hydrodynamic interactions of the conjugated-cytokines with the pores of the vessel wall that

hinder diffusive and convective transport respectively and D_0 is the diffusion coefficient of a particle in free solution given by the Stokes-Einstein equation. By ignoring electrostatic interactions H and W become [120]:

$$H = \frac{6\pi F}{K_t} \tag{45}$$

$$W = \frac{F(2 - F)K_s}{2K_t} \tag{46}$$

where F is the partition coefficient expressed as:

$$F = (1 - \lambda)^2 \tag{47}$$

where λ is the ratio of the conjugated-cytokines size to the vessel wall pore size and K_t and K_s are expressed as [120]:

$$\binom{K_t}{K_s} = \frac{9}{4}\pi^2\sqrt{2}(1\text{-}\lambda)^{-5/2}\left[1 + \sum_{n=1}^{2}\binom{a_n}{b_n}(1\text{-}\lambda)^n\right] + \sum_{n=0}^{4}\binom{a_{n+3}}{b_{n+3}}\lambda^n. \tag{48}$$

Molecular radius of agonist

The radius of the injected agonist is expressed as [154]:

$$\log_{10}R = -0.31 + 0.43\log_{10}M_w \tag{49}$$

where M_w is the molecular weight of agonist.

Needle outlet boundary conditions

$$-\mathbf{n}\cdot\left(-D_{Ic_f}\boldsymbol{\nabla}\mathbf{Ic_f} + \mathbf{v^f}Ic_f\right) = Ic_{f_{In}}\cdot V_{in} \tag{50}$$

$$\mathbf{v^f} = -V_{in}\mathbf{n} \tag{51}$$

Where V_{in} is the inflow velocity, $Ic_{f_{In}}$ is the initial concentration of injected cytokines.

Needle periphery boundary conditions

$$-\mathbf{n}\cdot\left(-\mathrm{D}_{\mathrm{Ic_f}}\nabla\mathbf{Ic_f}+\mathbf{v^f}\mathrm{Ic_f}\right)=0 \tag{52}$$

$$\mathbf{v^f}=0 \tag{53}$$

External surface boundary conditions

$$\mathrm{Ic_f}=0 \tag{54}$$

$$\mathrm{p_i}=0 \tag{55}$$

Modeling of immune response and tumor growth

The model equations are solved using COMSOL Multiphysics (COMSOL, Inc. Burlington, MA, USA). At the tumor center, the initial cancer cell density was assumed to have its peak value and then it decreases alongside the straight line due to a step function. The domain above a threshold cancer cell density is assumed as the tumor region and below that, the host tissue.

The parameters change from their abnormal-tumor value to their normal value as a function of the cancer cell density. The values change at the threshold cancer cell density using a step function. The step functions are used to certify continuity of the model variables. Equations were solved at a 1D geometry with spherical symmetry. At the left side of the 1D interval is the tumor center. As we move away from the tumor center we move towards the host tissue. Furthermore, previously used Equations (40) - (49) are also applied on the immune response and tumor growth model.

Kinematics of tumor growth

The growth stretch ratio is calculated as [44]:

$$3\frac{1}{\lambda_g}\frac{\mathrm{d}\lambda_g}{\mathrm{dt}}=\frac{\mathrm{R}_{\overline{\mathrm{T}}}}{\overline{\mathrm{T}_0}} \tag{56}$$

Where λ_g is the growth stretch ratio $\mathrm{R}_{\overline{\mathrm{T}}}$ the rate of change of the concentration of cancer cells and $\overline{\mathrm{T}_0}$ the initial concentration of cancer cells.

The tumor growth is implemented using deformation of the spatial frame mesh relative to the material frame mesh with a prescribed mesh displacement of

$$\mathbf{d_x} = \mathbf{x} - \mathbf{X} = \lambda_g \mathbf{X} - \mathbf{X} \tag{57}$$

Where x the spatial frame coordinates and X the material frame coordinates. The solid velocity is calculated as:

$$\mathbf{v^s} = \frac{d\mathbf{x}}{dt}$$

Where t is the time.

Interstitial pressure-fluid velocity

Normal and tumor tissues have properties similar to those of a porous medium. According to Darcy's law and the mesh movement due to solid velocity, the interstitial fluid velocity is given by:

$$\mathbf{v^f} = -k_{th} \boldsymbol{\nabla} \mathbf{p_i} + \mathbf{v^s} \tag{58}$$

where k_{th} is the hydraulic conductivity of the interstitial space [116]. The mass balance gives [115,155]:

$$\boldsymbol{\nabla} \cdot v^f = L_p S_v (p_v - p_i) - L_{pl} S_{vl} (p_i - p_{vl}) \tag{59}$$

The first term of the right-hand side of the equation describes the fluid flux entering from the blood vessels and the second term the flux exiting through the lymphatic system. L_p is the blood vessels' hydraulic conductivity, and p_v is the vascular pressure. L_{pl}, S_{vl} and p_{vl} are the corresponding parameters for the lymphatic vessels [116].

Intratumorally injected conjugated-cytokines

$$\frac{\partial Ic_f}{\partial t} + \boldsymbol{\nabla} \cdot \left(-D_{Ic_f} \boldsymbol{\nabla} \mathbf{Ic_f} + \mathbf{v^f} Ic_f \right) = -\frac{k_{on} c_e Ic_f}{\Phi} + k_{off} Ic_b + Q_{Ic} \tag{60}$$

$$\frac{\partial Ic_b}{\partial t} + \boldsymbol{\nabla} \cdot (\mathbf{v^s} Ic_b) = \frac{k_{on} c_e Ic_f}{\Phi} - k_{off} Ic_b \tag{61}$$

The free conjugated-cytokines that travel in the tumor interstitial space, Ic_f, can be transferred due to convection and diffusion, where D_{Ic_f} is the diffusion coefficient of the conjugated-cytokines in the interstitial space and $\mathbf{v^f}$ is the fluid velocity. Moreover, the free conjugated-cytokines are transferred across the tumor blood vessel and lymphatic vessel wall (Q_{Ic}). The remaining terms describe the binding and unbinding of the conjugated-cytokines: c_e is the concentration of collagen, k_{on}, k_{off} are the binding and unbinding rate constants, respectively and Φ is the volume fraction [153].

Pro-inflammatory cytokines from immune cells

The pro inflammatory cytokines produced by the immune cells can be transported by convection and diffusion:

$$\frac{\partial c_c}{\partial t} + \boldsymbol{\nabla} \cdot \left(-D_{c_c}\boldsymbol{\nabla c_c} + \mathbf{v^f} c_c\right) = k_{In}In + k_{T^E}T^E + k_{Th^E}Th^E + k_{APC}APC - \delta_{c_c}c_c \quad (62)$$

Where the right-hand side terms describe the production of pro inflammatory cytokines by innate immune cells, effector CD8+ and CD4+ Tcells and antigen presenting cells. The last term describes the degradation of cytokines.

Total pro-inflammatory cytokines

The total pro-inflammatory cytokines are a combination of the injected cytokines, the injected cytokines bound to collagen and the pro-inflammatory cytokines produced by the immune cells.

$$c = M_w Ic_f + M_w Ic_b + c_c \quad (63)$$

The cytokines related to the injected agonist are solved in $\frac{mol}{m^3}$ and the cytokines by the immune cells in $\frac{kg}{m^3}$ thus the molecular wight M_w converts the units to enable the summation.

Trafficking of immune cells

Normalization of the tumor micro-environment increases trafficking of immune cells when combined with immunotherapy. When the vascular density doubles from $50cm^{-1}$ to $100cm^{-1}$ the source of immune cells increases by 1.367. By assuming that the function is

1 for the host tissue value of ($70\mathrm{cm}^{-1}$). The trafficking functions reads pro-inflammatory cytokines produced by the immune cells [156].

$$\mathrm{T_f} = 0.0273\mathrm{Sv} - 0.9138 \tag{64}$$

where $\mathrm{S_v}$ represents the functional vascular density measured in cm^{-1}.

Immature antigen presenting cells

The immature antigen presenting cells are expressed as:

$$\begin{aligned}\frac{\partial \mathrm{IAPC}}{\partial \mathrm{t}} + \boldsymbol{\nabla} \cdot (-\mathrm{D_{IAPC}} \boldsymbol{\nabla IAPC} + \mathbf{v^s} \mathrm{IAPC}) = \lambda_{\mathrm{IAPC}} \mathrm{T_f} \left(\frac{\mathrm{c}}{\mathrm{K_{cAPC}} + \mathrm{c}}\right) - \delta_{\mathrm{IAPC}} \mathrm{IAPC} \\ -\chi_{\mathrm{APC}} \left(\frac{\mathrm{c}}{\mathrm{K_{cAPC}} + \mathrm{c}}\right) \left(\mathrm{n_{In}} \mathrm{IAPC} \overline{\mathrm{T}} + \mathrm{n_{A_g}} \mathrm{IAPCA_g}\right)\end{aligned} \tag{65}$$

Where the first right-hand term describes the source of immature antigen presenting cells, the second term the degradation and the last term the reduction due to activation. The activation to antigen presenting cells depends on the pro-inflammatory cytokines and the interaction of immature antigen presenting cells with the tumor cells and antigen.

Antigen presenting cells

The antigen presenting cells are expressed as:

$$\begin{aligned}\frac{\partial \mathrm{APC}}{\partial \mathrm{t}} + \boldsymbol{\nabla} \cdot (-\mathrm{D_{APC}} \boldsymbol{\nabla APC} + \mathrm{v^s} \mathrm{APC}) = \\ \chi_{\mathrm{APC}} \left(\frac{\mathrm{c}}{\mathrm{K_{cAPC}} + \mathrm{c}}\right) \left(\mathrm{n_{In}} \mathrm{IAPC} \overline{\mathrm{T}} + \mathrm{n_{A_g}} \mathrm{IAPCA_g}\right) - \delta_{\mathrm{APC}} \mathrm{APC}\end{aligned} \tag{66}$$

Where the first right-hand term describes the increase of antigen presenting cells due to the activation from immature antigen presenting cells and the last term is a degradation term.

Effector CD4+ T cells

The effector CD4+ T cells are expressed as:

$$\frac{\partial \mathrm{Th^E}}{\partial \mathrm{t}} + \boldsymbol{\nabla} \cdot (-\mathrm{D_{Th^E}} \mathbf{\nabla Th^E} + \mathrm{v^s Th^E}) = \mathrm{m_{APC}} \mathrm{T_f} \mathrm{APC} - \delta_{\mathrm{Th^E}} \mathrm{Th^E} \tag{67}$$

Where the first term describes the source of effector CD4+ T cells which is assumed to be analog to the concentration of antigen presenting cells responsible for the activation of CD4+ T cells in the lymph nodes. The last term is the degradation of CD4+ T cells.

Effector CD8+ T cells

The effector CD8+ T cells are expressed as:

$$\frac{\partial \mathrm{T^E}}{\partial \mathrm{t}} + \boldsymbol{\nabla} \cdot (-\mathrm{D_{T^E}} \boldsymbol{\nabla} \mathbf{T^E} + \mathbf{v^s} \mathrm{T^E}) = \mathrm{m_{APC}} \mathrm{T_f APC} - \delta_{\mathrm{T^E}} \mathrm{T^E} \tag{68}$$

Where the first term describes the source of effector CD8+ T cells which is assumed to be analog to the concentration of antigen presenting cells responsible for the activation of CD8+ T cells in the lymph nodes. The last term is the degradation of CD8+ T cells.

Innate cells

The innate immune cells that induce cytolysis are expressed as:

$$\frac{\partial \mathrm{In}}{\partial \mathrm{t}} + \boldsymbol{\nabla} \cdot (-\mathrm{D_{In}} \boldsymbol{\nabla} \mathbf{In} + \mathbf{v^s} \mathrm{In}) = \lambda_{\mathrm{In}} \mathrm{T_f} \left(\frac{\mathrm{c}}{\mathrm{K_{cAPC}} + \mathrm{c}} \right) - \delta_{\mathrm{In}} \mathrm{In} \tag{69}$$

Where the first term describes production of innate cells which depends on the concentration of pro-inflammatory cytokines.

Cancer cells

The concentration of cancer cells is expressed as:

$$\frac{\partial \overline{\mathrm{T}}}{\partial \mathrm{t}} + \boldsymbol{\nabla} \cdot \left(-\mathrm{D_{\overline{T}}} \boldsymbol{\nabla} \overline{\mathbf{T}} + \mathbf{v^s} \overline{\mathrm{T}} \right) = \mathrm{R_{\overline{T}}} = \mathrm{k_1} \left(\frac{\mathrm{c_{ox}}}{\mathrm{K_2} + \mathrm{c_{ox}}} \right) \overline{\mathrm{T}} - (\mathrm{n_{In}} \mathrm{In} + \mathrm{n_{In}} \mathrm{IAPC} + \mathrm{n_{ad}} \mathrm{T^E}) \overline{\mathrm{T}} \tag{70}$$

Where the first right-hand side term describes the proliferation of cancer cells due to oxygen and the last term describes the killing of cancer cells by innate cells, immature antigen presenting cells and effector CD8+ T cells.

Antigen

The concentration of cancer cells is expressed as:

$$\frac{\partial A_g}{\partial t} + \boldsymbol{\nabla} \cdot \left(-D_{A_g} \boldsymbol{\nabla A_g} + \mathbf{v^f} A_g\right) = (n_{In} In + n_{ad} T^E)\overline{T} - n_{A_g} IAPC A_g \quad (71)$$

Where the first right-hand side term describes the production of antigen induced by the cytolytic effect of innate cells and effector CD8+ T cells. The last term describes the antigen uptake by the immature antigen presenting cells.

Oxygen transport

The rate of change of oxygen concentration in the tissue was modeled with a convection diffusion equation that includes a source and a sink term [117,118], . The source term is due to oxygen supply from the blood vessels and the sink term describes oxygen consumption by cancer cells:

$$\frac{\partial c_{ox}}{\partial t} + \boldsymbol{\nabla} \cdot \left(-D_{c_{ox}} \boldsymbol{\nabla c_{ox}} + \mathbf{v^f} c_{ox}\right) = -\frac{A_{ox} c_{ox}}{c_{ox} + k_{ox}} \frac{\overline{T}}{\overline{T_0}} + P_{erox} S_v (c_{iox} - c_{ox}) \quad (72)$$

where S_v is the vascular density, D_{ox} the oxygen diffusion coefficient, A_{ox} and k_{ox} are oxygen uptake parameters, c_{iox} is the oxygen concentration in the vessels, v^f is the fluid velocity and P_{erox} is the vascular permeability of oxygen defined as the oxygen diffusion coefficient divided by the length of the vessel wall.

Immune cell death rate

According to experimental data [157], a 40 times decrease in oxygen concentration (from 20% to 0.5%) doubled the apoptotic rate of immune cells. Thus the degradation rates are expressed as:

$$\delta_{IAPC} = \delta_{IAPC_0} + 1.025 \cdot \left(1 - \frac{c_{ox}}{c_{iox}}\right) \cdot \delta_{IAPC_0} \quad (73)$$

$$\delta_{APC} = \delta_{APC_0} + 1.025 \cdot \left(1 - \frac{c_{ox}}{c_{iox}}\right) \cdot \delta_{APC_0} \quad (74)$$

$$\delta_{Th^E} = \delta_{Th_0^E} + 1.025 \cdot \left(1 - \frac{c_{ox}}{c_{iox}}\right) \cdot \delta_{Th_0^E} \quad (75)$$

$$\delta_{T^E} = \delta_{T_0^E} + 1.025 \cdot \left(1 - \frac{c_{ox}}{c_{iox}}\right) \cdot \delta_{T_0^E} \quad (76)$$

$$\delta_{In} = \delta_{In_0} + 1.025 \cdot \left(1 - \frac{c_{ox}}{c_{iox}}\right) \cdot \delta_{In_0} \quad (77)$$

Tumor center boundary conditions

Due to the symmetry at the tumor center of the 1D geometry with spherical symmetry no flux boundary conditions were used thus no diffusive or convective transport. No flux boundary conditions were applied to all partial differential equations.

$$-D_{c_{ox}} \nabla \mathbf{c_{ox}} + \mathbf{v^f} c_{ox} = 0 \quad (78)$$

$$-k_{th} \nabla \mathbf{p_i} + \mathbf{v^s} = 0 \quad (79)$$

$$-D_{In} \nabla \mathbf{In} + \mathbf{v^s} In = 0 \quad (80)$$

$$-D_{IAPC} \nabla \mathbf{IAPC} + \mathbf{v^s} IAPC = 0 \quad (81)$$

$$-D_{c_c} \nabla \mathbf{c_c} + \mathbf{v^s} c_c = 0 \quad (82)$$

$$-D_{T^E} \nabla \mathbf{T^E} + \mathbf{v^s} T^E = 0 \quad (83)$$

$$-D_{Th^E} \nabla \mathbf{Th^E} + \mathbf{v^s} Th^E = 0 \quad (84)$$

$$-D_{APC} \nabla \mathbf{APC} + \mathbf{v^s} APC = 0 \quad (85)$$

$$-D_{\overline{T}} \nabla \overline{\mathbf{T}} + \mathbf{v^s} \overline{T} = 0 \quad (86)$$

$$-D_{A_g} \nabla \mathbf{A_g} + \mathbf{v^s} A_g = 0 \quad (87)$$

$$-D_{Ic_f} \nabla \mathbf{Ic_f} + \mathbf{v^s} Ic_f = 0 \quad (88)$$

$$\mathbf{v^s} Ic_b = 0 \quad (89)$$

External surface boundary conditions

For the external surface boundary condition. Oxygen was assumed to have a constant value of the normal tissue.

$$c_{ox} = c_{iox} \tag{90}$$

No flux boundary condition was applied for the solution of the fluid pressure, according to the Darcy law and the domain deformation by the solid velocity.

$$-k_{th}\nabla \mathbf{p_i} + \mathbf{v^s} = 0 \tag{91}$$

No flux boundary conditions were applied for the innate immune cells and the cytokines produced by the immune cells. This was done because it was assumed that there is not a mass flux of these concentrations at the external surface.

$$-D_{In}\nabla \mathbf{In} + \mathbf{v^s}In = 0 \tag{92}$$

$$-D_{IAPC}\nabla \mathbf{IAPC} + \mathbf{v^s}IAPC = 0 \tag{93}$$

$$-D_{c_c}\nabla \mathbf{c_c} + \mathbf{v^s}c_c = 0 \tag{94}$$

The external surface is away from the tumor region and it is not reached by the cancer cells. Thus, the cancer cells density was assumed 0 as well as all the effector cells and the antigen that depend on the existence of tumor cells.

$$T^E = 0 \tag{95}$$

$$Th^E = 0 \tag{96}$$

$$APC = 0 \tag{97}$$

$$\overline{T} = 0 \tag{98}$$

$$A_g = 0 \tag{99}$$

The external surface is away from the tumor region and thus it is not reached by the injected cytokines. Thus, the injected cytokines and the cytokines that bound to target were assumed 0.

$$\mathrm{Ic_f} = 0 \tag{100}$$

$$\mathrm{Ic_b} = 0 \tag{101}$$

Fitting of the model to experimental data

For each fitting we calculated the sum of the squared difference of the values between the measured $\mathrm{V_{exp}}$ and simulated $\mathrm{V_{calc}}$ tumor volumes divided by the number of experimental values N,

$$\mathrm{Er} = \frac{\sum_i \left[\mathrm{V_{exp,i}} - \mathrm{V_{calc,i}}\right]^2}{\mathrm{N}} \tag{102}$$

We repeated this calculation for all fittings in order to calculate $\mathrm{Er_{tot}}$.

$$\mathrm{Er_{tot}} = \mathrm{Er_{exp1,control}} + \mathrm{Er_{exp2,control}} + \mathrm{Er_{exp1,drug}} + \mathrm{Er_{exp2,drug}} \tag{103}$$

When $\mathrm{Er_{tot}}$ becomes zero, the simulated volume curves match exactly with the experimental points. Thus, we minimize this value using the COMSOL with MATLAB interface (LiveLink for MATLAB) in order for Matlab to find the optimum parameters that can be used in the COMSOL model. Specifically, prior to the optimization, manual adjustments of the estimation parameters were made so that the experimental values were close to the numerical values. Then a Nelder-Mead optimization was used with MATLAB's fminsearch function to calculate the optimum parameters by reducing total error.

Results

Model calibration and determination of model parameters values

The values of the model parameters that could not be obtained from previous studies (Table 12) were determined by fitting the model to tumor growth data from two published studies [20,21]. These studies included a control group that did not receive any treatment (control)

and a group that received intratumoral injection of conjugated-cytokines as a drug. For the control groups, the variables related to the injected conjugated-cytokines become zero so that the pro-inflammatory cytokines in the tissue are produced only by the immune cells (Equation (63)). We did not consider any other variation of model parameters between the control and injected cytokines group. All tumor growth curves were fitted simultaneously to optimize the global fit. An optimization algorithm in MATLAB (The Mathworks, Inc., Natick, MA, United States) using the COMSOL with MATLAB interface was employed for the fitting.. As shown in Figure 19 the model can reproduce tumor growth data with a good accuracy ($R^2 \sim 1$).

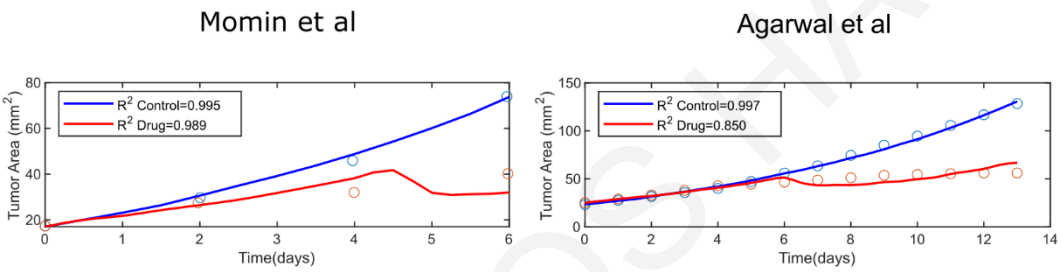

Figure 19: Experimental data (circles) of tumor growth and model predictions (solid line) for control tumors (blue) and tumors treated with intratumoral injection of conjugated-cytokines (red) by Momin et al. (B16F10 tumor cells) [21] and Agarwal et al. (Ag104A tumor cells) [20].

Due to the complexity of the model that includes various interactions and mechanisms, the behavior of the model variables is not intuitive. Thus, we generated plots to further investigate the changes in the model variables that led to the reduction of the tumor growth after the injection of therapy. Model predictions for the spatial distribution of cytokines are presented in Figure 20, whereas predictions for IFP, antigen concentration, CD8+ T cells and NK cells are presented in Figure 21 for both studies. Day 0 corresponds to the time of the intratumoral injection of the conjugated-cytokines. The concentration of the total cytokines decreased after the injection as expected.

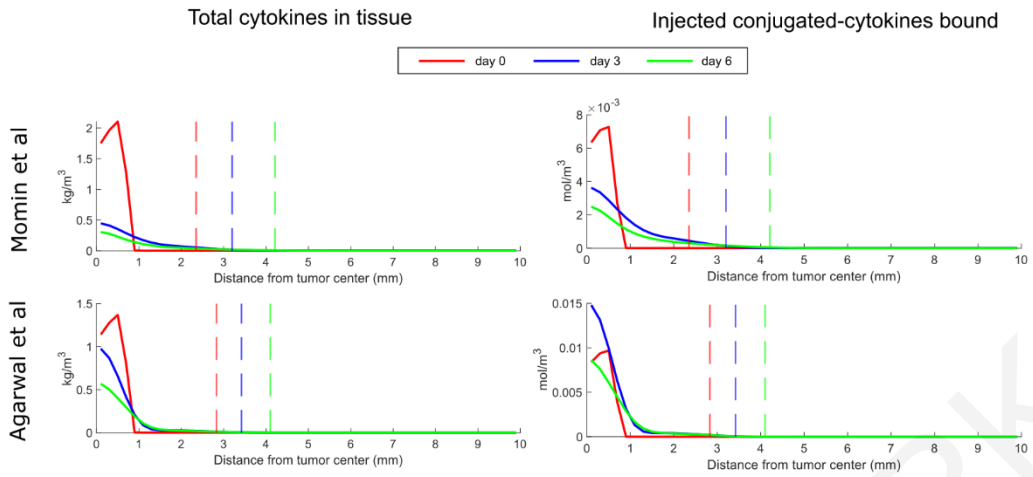

Figure 20: Results for the total amount of cytokines and the bound conjugated-cytokines for various time points for each study. The plots represent the distribution in the radial direction. The value 0 in the x axis corresponds to the tumor center. As we move along the x axis, we move away from the tumor center towards the host tissue. Plots include both the tumor region and host tissue that surrounds the tumor. The vertical dashed lines show the tumor boundary at the given time points.

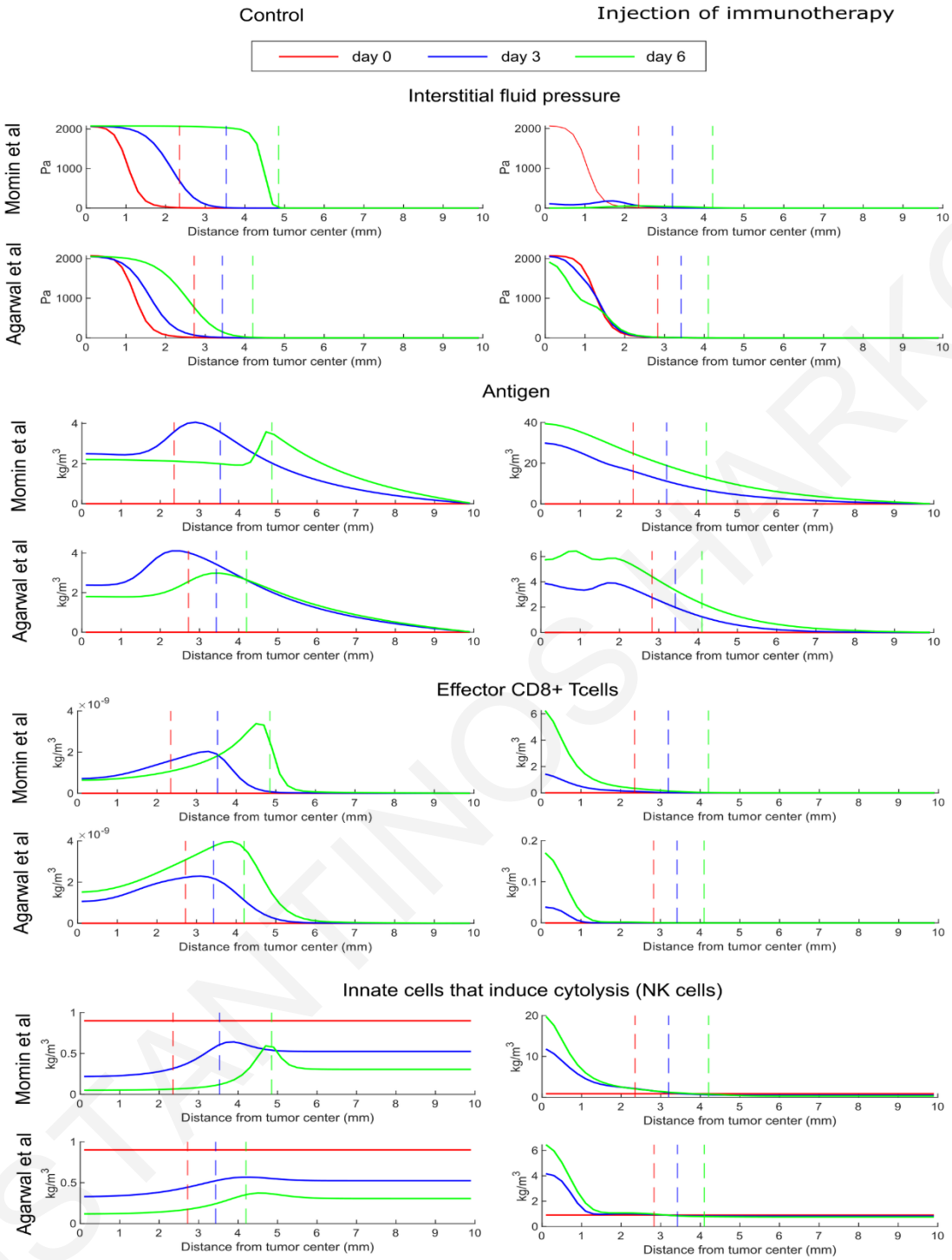

Figure 21: Results at various time points for each optimization case. The plots represent the distribution in the radial direction. The value 0 in the x axis corresponds to the tumor center. As we move along the x axis, we move away from the tumor center towards the host tissue. Plots include both the tumor region and host tissue that surrounds the tumor. The vertical dashed lines represent the tumor boundary.

The IFP was elevated within the tumor, reaching the levels of microvascular fluid pressure at the tumor center and droped to normal values at the tumor margin (Figure 21, control). This spatial distribution of IFP created a fluid flux at the tumor margin towards the host tissue, resulting in increased concentration of antigen, effector CD8+ T cells and NK cells at the interface of the tumor with the host tissue compared to the tumor interior (control group). Intratumoral injection of cytokines can reduce the IFP levels, which is more evident in the case of Momin et al. [21] where the efficacy of the treatment is more pronounced and induced considerably higher amounts of innate and adaptive immune cells compared to the respective control cases. In the treatment case, the spatial distribution of immune cells changed compared to the control and most immune cells can be found at the center of the tumor where the concentration of cytokines and antigens is the highest.

Dependence of treatment efficacy on conjugated-cytokines properties

Subsequently, we aimed to investigate how changing the properties of the conjugated-cytokines can affect the efficacy of treatment. Specifically, we varied the size and binding affinity of the drug and the model predictions are presented in Figure 22 for varying the conjugated-cytokines radius, rs, from 1 to 8 nm and when the binding rate constant, kon, is increased/decreased by an order of magnitude.

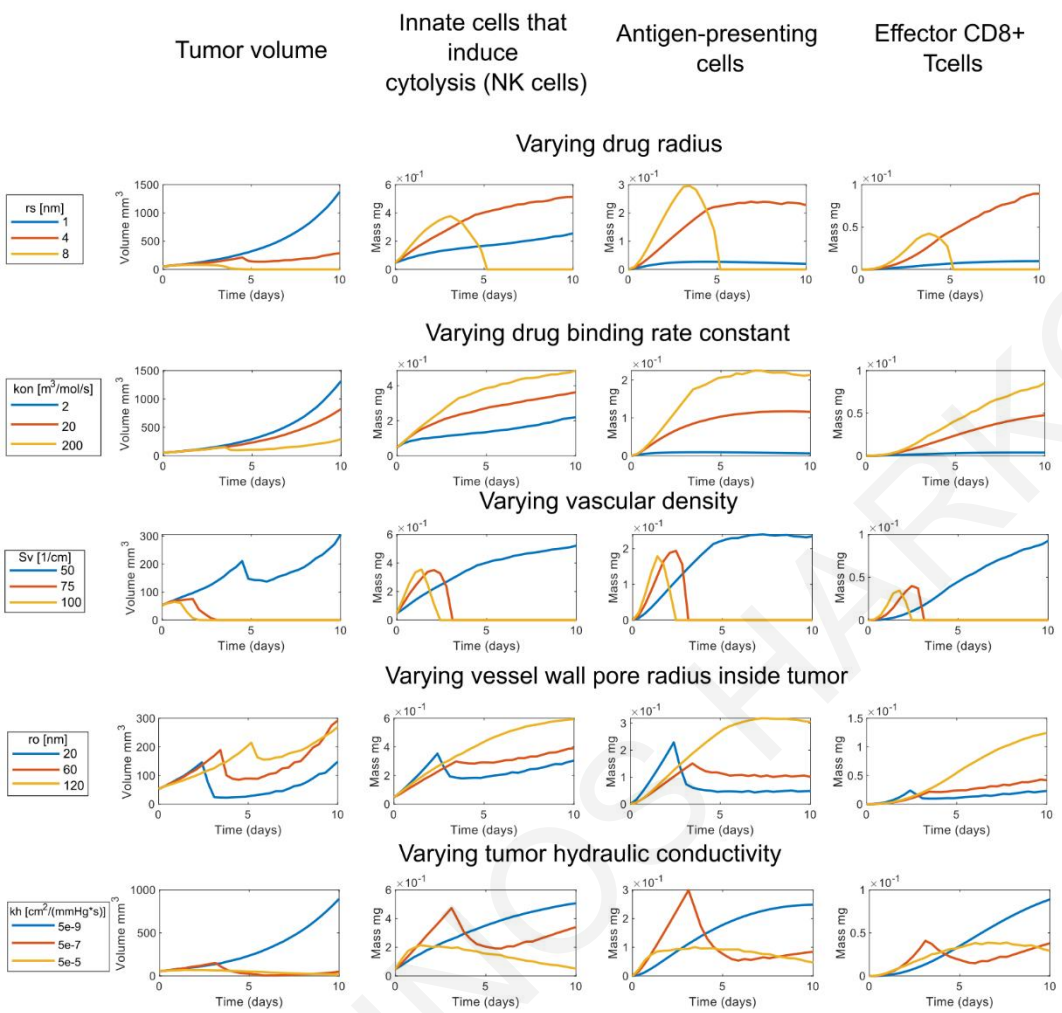

Figure 22: The impact of various model components to tumor growth by varying a single parameter. Figure presents the tumor growth through time and the number of innate cells that induce cytolysis (NK cells), antigen presenting cells and effector CD8+ T cells when varying: the injected conjugate radius, the conjugate binding rate constant, the vascular density inside the tumor region, the vessel wall pore radius inside tumor, and the hydraulic conductivity inside the tumor region. The baseline values of the parameters for these simulations are: rs=3.85[nm], kon=100 [m^3/mol/s], Sv=50[1/cm], r_0=100 [nm], kh=4.13e-8 [cm^2/mmHg/s].

Changes in both the size of conjugated-cytokines from 1 to 8 nm in radius and the binding rate constant from 2 to 200 m^3/mol/s altered the tumor growth rate and induced significant changes in the number of immune cells. Cytokine conjugates of small size were cleared fast from the tumor owing to increased diffusion within the tumor and intravasation into blood vessels and thus, cannot induce a significant anti-tumor immune response. Increasing the

size of the drug to 4-8 nm in radius dramatically reduced tumor volume and even eliminated tumor. Increases in binding rate constant hindered the clearance of the cytokines and thus, improved anti-tumor immune responses, by increasing the number of intratumoral CD8+ T cells soon after intratumoral administration of cytokines.

Role of the tumor microenvironment in treatment efficacy

Next, we set out to study how varying the physical and physiological properties of the TME can improve the efficacy of injected conjugated-cytokines. Specifically, we varied the vascular density and tumor vessel wall permeability (i.e., the size of the pores in the tumor vessel walls) as well as the hydraulic conductivity of the tumor. The tumor functional vascular density was varied from 50 to 100 cm^{-1} [158], the radius of the pores of the tumor vessel walls from 20 nm to 120 nm [159,160], and the tumor hydraulic conductivity from $5x10^{-9}$ to $5x10^{-5}$ cm^2/mmHg-s [160]. As shown in Figure 22, a 50% increase in the functional vascular density and thus, tumor perfusion, was sufficient to potentiate anti-tumor immunity. In the model and in agreement with the literature, increase in perfusion increased the number of immune cells in the tumor at early times after cytokines injection (Figure 22), which led to complete tumor elimination. Subsequently the immune cells left the tumor and their numbers go down to zero. Elimination of tumor is also predicted when the hydraulic conductivity of the tumor was increased. The increase in the tumor hydraulic conductivity increased the interstitial velocity and thus, allowed for better penetration of the conjugated cytokines in all regions of the tumor. This resulted in a robust anti-tumor immune response and a dramatic reduction in tumor volume.

Finally, the vessel wall pore size determined the transport of the conjugates across the tumor vessel wall. Tumors hinder the transport of nano-sized drugs across the tumor vessels [144]. Model predictions agree with previous findings in that tumors with more permeable vessels allowed the transvascular transport of nano-sized therapeutics and in our case allowed the clearance of the conjugated cytokines, which reduced treatment efficacy (Figure 22). Interestingly, the model predicted that even though the tumor responded to therapy at early times after cytokines administration and thus, the tumor volume decreased, at longer times the tumor regrew, which implies the need for repeated intratumoral administration of cytokines. Interestingly, vascular normalization strategies aim to reduce vessel permeability

to large molecule/nanoparticles, whereas stroma normalization strategies improve tumor hydraulic conductivity, in both cases improving perfusion [161].

To further investigate the effect of the properties of the TME and the injected conjugated-cytokines, we varied two parameters simultaneously to generate tumor volume diagrams as shown in Figure 23. From these diagrams, firstly, we conclude that increasing the tumor hydraulic conductivity enhanced the efficacy of conjugated cytokines even of small size and low binding affinity (Figure 23a and Figure 23b). Furthermore, increasing the size of the drug and thus, decreasing both the diffusion of the conjugated-cytokines within the tumor tissue and their extravasation into the blood vessels results in reduced tumor volumes for various values of the hydraulic conductivity. Interestingly, increasing the drug size for a tumor with low hydraulic conductivity can induce a similar effect with a smaller drug in a tumor environment with high hydraulic conductivity (Figure 23b). Additionally, reduced tumor volumes can be achieved for lower binding capabilities of the conjugated-cytokines by decreasing the vessel wall pores. Also, increasing the binding rate constant to more than 50 m^3/mol/s can reduce tumor volume independent of the vessel wall pore size (Figure 23c). By also increasing the drug size we can achieve improved therapeutic efficacy independently from the vessel wall pore size as well (Figure 23d). Finally, increasing vascular density, while also increasing either the binding affinity or the size of the conjugated cytokines can enhance the efficacy of the treatment (Figure 23e and Figure 23f). From all the analysis, can be inferred that conjugated-cytokines larger than 5 nm in radius with binding rate constant above 50 m^3/mol/s can induce better therapeutic outcomes.

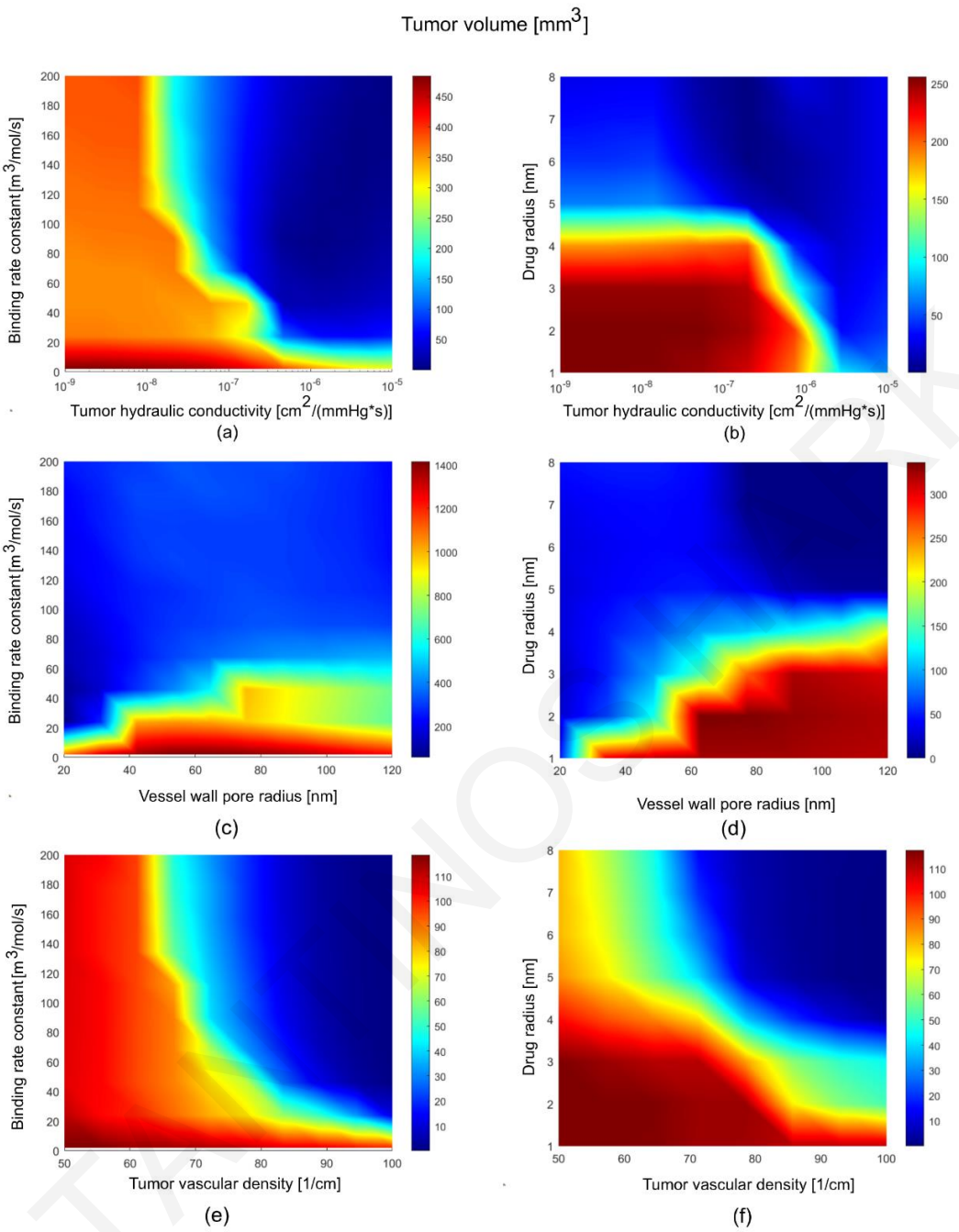

Figure 23: Diagrams of the efficacy of conjugated-cytokines injection as a function of tumor physiological properties and conjugate radius and binding affinity. Each point in the diagrams represents the tumor volume of a different simulation. The tumor volume is measured either at the end of the simulations (day 10) or at the time point where at least one of the simulations reached complete cure (i.e., tumor volume becomes zero). For each simulation only the parameters shown in the two axes were varied. (a) The hydraulic conductivity in the tumor region was varied relative to the binding of the injected conjugate (day 7.5) and (b) the conjugate radius (day 5.2). (c) The tumor vessel wall pore radius was varied relative to the binding of the injected conjugate (day 10) and (d) the conjugate radius (day

6.0). (e) The tumor vascular density was varied relative to the binding of the injected conjugate (day 3.2) and (f) the conjugate radius (day 2.9).

Discussion

Our model simulations support the hypothesis that intratumoral injection of tethered cytokines is a promising strategy to control tumor growth. Previous mathematical models showed that by increasing molecular size and/or matrix-targeting affinity of the injected cytokines improves therapeutic efficacy [22]. Our study agrees with these findings, predicting that by increasing the molecular size, the effective diffusion of the injected conjugated-cytokines decreases and thus, they remain within the tumor at higher concentrations. Also, the exposure within the tumor region increases when increasing the binding affinity and thus, making it more difficult for the cytokines to escape from the tumor. Therefore, both molecular weight and binding will lower the effective diffusion rate of the injected drug and only convection can distribute the drug uniformly from the injection site to throughout the tumor. Additionally, our study extends the modeling framework by adding spatiotemporal variations in model parameters, pathophysiological properties of the TME, IFP gradients, convection-diffusion within the tumor and host tissue and across the vessel walls, and cancer-immune cells interactions. Our results suggest that these additional considerations shed further light on the outcome of the treatment. For example, incorporation of the immune system revealed that the injected conjugated-cytokines boost the activation of the adaptive immune cells and also support innate immune cells to further activate the adaptive immune system.

Our results also highlight the fact that normalizing pathophysiological features of the TME can improve therapeutic effects. Abnormal blood vessels is a hallmark of solid tumors [162]. Blood vessel abnormalities include hyperpermeability of the tumor vessel wall, as a result of increased levels of proangiogenic factors released under tumor hypoxic conditions, and/or vessel compression/collapse due to the accumulation of mechanical forces in the tumor [1,163]. In both cases, tumor vessel perfusion is reduced. Tumor hydraulic conductivity is often low in fibrotic, desmoplastic tumors, such as triple-negative breast cancer, pancreatic cancer and sarcomas. The excessive collagen matrix and hyaluronan in these tumors hinder the transport of fluid within the tumor interstitial space and thus, decrease the hydraulic

conductivity. Stroma normalization strategies aim to target these components of the extracellular matrix either directly or by reprogramming cancer-associated fibroblasts. Therefore, stroma normalization can decompress vessels, improving functional vascular density and increasing the hydraulic conductivity of the tumor [1,163]. Increase in the hydraulic conductivity also enhances convective transport and makes the distribution of the conjugated-cytokines in the tumor more uniform. Our model simulations show that modulation of the TME to reduce vascular permeability, improves perfusion and increases hydraulic conductivity. These strategies should be considered to improve therapeutic outcomes of intratumorally injected cytokines. The strategy to normalize the TME should be tailored to its specific pathophysiological characteristics: abundant hyperpermeable vessels or abundant extracellular matrix or both. Our model simulations also agree with published data, highlighting that the conjugate size and binding capability have a large impact on the outcome of therapy. This is promising because by designing the optimal conjugate, the treatment could be improved. Furthermore, combination with a TME-normalizing strategy would further add to the efficacy of the treatment.

Although the model predicted reduced tumor growth due to the administration of conjugated-cytokines, at longer times the tumor recovered. Repeating intratumoral administration might further maintain therapeutic effects and increase efficacy. However, multiple injections might increase systemic accumulation of the conjugated-cytokines, leading to toxic effects [164]. Modulation of the TME and designing conjugated-cytokines with increased molecular size and/or matrix-targeting affinity reduces toxic accumulation and might increase the number of the permiting injections without causing toxic effects. In general, there might be a minimum time of exposure of a certain concentration of the conjugated-cytokines inside the tumor, for the therapy to be effective. This threshold could be akin to the Allee effect [165–167], where below a certain exposure time of this minimum concentration, the treatment is not effective enough to trigger a sufficient immune response to combat the cancer cells. There might be also a minimum exposure time of a certain concentration of the cytokines in the blood that causes toxicity. Thus, when considering intratumoral injection of conjugated-cytokines this level should not be exceeded. Both these thresholds may vary from patient to patient, which makes the development of a personalized adaptive therapy framework that includes the monitoring of the individual's tumor and immune response a promising approach to optimize therapeutic effects.

Our model also has some limitations as we made several assumptions to keep the model simple. The tumor was assumed to grow as a sphere, which is not usually the case. In addition, the model did not account for the drug-conjugate surface charge and configuration, which along with the conjugate size, can affect its transport properties [163,168,169]. Furthermore, the vessel wall pore radius was assumed uniform, while there must be a distribution. Transport properties, such as the interstitial diffusivity of the conjugates, depend not only on their size but also on the density (i.e., porosity) of the tumor interstitial space that varies among tumor types [147]. In this study we did not consider changes in the diffusion coefficient of the conjugates due to variations among tumor types. We also assumed very few intratumor immune cells and none of them activated at the beginning of the simulation. This may not be the case for many tumors. Also, our model did not account for the fact that immune cells can secrete immunosuppressive cytokines. Furthermore, our model does not explicitly incorporate the draining lymph node and effector T cell priming or the cancer cells leaving the tumor via the blood vessels and peri-tumoral lymphatics. In principle, we can relax these assumptions by incorporating additional parameters into our model. However, this is likely to change the results only quantitatively, whereas the conclusions reached in this study related to the parameters that affect the efficacy of intratumoral injection of conjugated-cytokines would remain unchanged.

Chapter 4: Investigating the synergistic effects of immunotherapy and normalization treatment in modulating tumor microenvironment and enhancing treatment efficacy

This study has been published in the Journal of Theoretical Biology: Harkos C, Stylianopoulos T. Investigating the synergistic effects of immunotherapy and normalization treatment in modulating tumor microenvironment and enhancing treatment efficacy. Journal of Theoretical Biology. 2024; 111768. https://doi.org/10.1016/j.jtbi.2024.111768

Summary

We developed a comprehensive mathematical model of cancer immunotherapy that takes into account: i) Immune checkpoint blockers (ICBs) and the interactions between cancer cells and the immune system, ii) characteristics of the tumor microenvironment, such as the tumor hydraulic conductivity, interstitial fluid pressure, and vascular permeability, iii) spatial and temporal variations of the modeled components within the tumor and the surrounding host tissue, iv) the transport of modeled components through the vasculature and between the tumor-host tissue with convection and diffusion, and v) modeling of the tumor draining lymph nodes were the antigen presentation and the development of cytotoxic immune cells take place. Our model successfully reproduced experimental data from various murine tumor types and predicted immune system profiling, which is challenging to achieve experimentally. It showed that combination of ICB therapy and normalization treatments, that aim to improve tumor perfusion, decreases interstitial fluid pressure and increases the concentration of both innate and adaptive immune cells at the tumor center rather than the periphery. Furthermore, using the model, we investigated the impact of modeled components on treatment outcomes. The analysis found that the number of functional vessels inside the tumor region and the ICB dose administered have the largest impact on treatment outcomes.

Introduction

In solid tumors, the rapid proliferation of cancer cells within the confined space of the host tissue along with the accumulation of stromal cells and extracellular matrix components (e.g., collagen and hyaluronan) can result in stiffening of the tumor and compression of

intratumoral blood vessels [2–4,170,171]. Furthermore, the structure of the tumor vasculature exhibits abnormalities, such as the increased spacing between endothelial cells, the loss or loosening of the basement membrane and the absence of perivascular cells, which lead to the hyper-permeability of the vessel walls. The compression and the hyper-permeability of the vessels can reduce significantly the amount of blood vessels, resulting in hypo-perfusion [1,172]. Also, a consequence of the hyper-permeability of the tumor blood vessels is the uniform elevation of the IFP in the tumor interior that reaches the values of the microvascular pressure [2,140]. Due to the elevation of IFP, the pressure gradients across the vessel wall are decreased, that hinders the transvascular transport of macromolecules and nano-sized drugs to the tumor, making it a significant obstacle to drug delivery [11–13,139,144,158,168].

Among other drugs, the abnormal microenvironment in the tumor region hinders the delivery of ICBs [163]. In contrast to chemotherapy that targets cancer cells to eliminate their proliferation, immunotherapy enhances the ability of the host immune system to kill more effectively tumor cells [19]. ICBs that target the immune checkpoints: CTLA4, PD1 and PDL1 demonstrated robust efficacy in many types of cancer, especially in melanoma and non-small cell lung cancer (NSCLC) [173]. Nonetheless, fewer than 20% of patients presently experience advantages from these therapies [23]. Furthermore, a significant number of patients encounter immune-related adverse effects, including potentially fatal ones [24]. Improving the delivery of ICBs by restoring the abnormalities of the tumor microenvironment has shown promise in improving ICB efficacy in the preclinical setting [174–177] and pertinent clinical trials have been initiated (clinicaltrials.gov identifier: NCT03563248). Addressing these difficulties involves a strategy of normalizing the tumor vasculature and microenvironment to increase vessels functionality [126]. To achieve this, agents that reprogram cancer-associated fibroblasts to reduce the production of collagen and hyaluronan have been employed successfully [163,178,179]. As a result, some of the tumor blood vessels are decompressed, perfusion is enhanced and therapy is improved [180]. Such agents that have been used in preclinical tumor models to improve the efficacy of ICB treatment includes clinically approved drugs, such as the antihypertensives bosentan and losartan [177,181] and the antihistamines tranilast and ketotifen [175,176,182–184].

Mathematical modeling can be employed to provide mechanistic insights of the effects of tumor normalization on the efficacy of ICBs. *In silico* studies have modeled ICBs by examining the interactions and temporal changes of immune cells and cancer cells using ODEs [185]. Other studies, in addition to temporal changes considered spatial changes inside the tumor domain to investigate the role of exosomes and combination therapy of ICBs with cancer vaccines [145,146]. These studies, however, do not model the tumor draining lymph nodes, which are the primary sites of the development of anti-tumor immunity [186]. Studies that model the tumor draining lymph nodes focus on the pharmacokinetics and pharmacodynamics of antibodies [187,188]. We and co-workers have previously developed mathematical models to investigate the role of vascular permeability, diffusion coefficient and hydraulic conductivity, binding and metabolism, interstitial fluid pressure as well as lymphatics in the delivery of nano-sized drugs, including antibodies [1,11–13,42,45,189]. Based on our previous modeling work, here we developed a model that considers: i) the delivery of ICBs and the interactions of cancer cells with immune cells ii) properties of the tumor microenvironment, including the functional tumor vessels, the hydraulic conductivity, the interstitial fluid pressure and the permeability of the vessels, iii) spatial and temporal variations of the modeled components inside the tumor and the surrounding host tissue, iv) transport of modeled components through the vasculature and between the tumor-host tissue with convection and diffusion and v) modeling of the tumor draining lymph nodes were the antigen presentation and the development of cytotoxic immune cells (specific on targeting the cancer cells) takes place. We used the model to derive insights of the role of parameters of the tumor microenvironment that are involved in normalization strategies to enhance ICB therapy.

Materials and methods

Modeled compartments and implementation

At this study, we introduced a novel approach where the mathematical model consisted of three compartments: the central blood compartment, the tumor draining lymph nodes and the tumor - host tissue compartment (Figure 24 and Figure 25). The blood and tumor draining lymph nodes compartments were assumed to have homogeneous concentrations of the modeled variables. Thus, for those two compartments a set of ODEs was solved. For the

tumor – host tissue compartment, we introduced a set of partial differential equations solved with the finite element method by considered not only temporal but also spatial variations of the modeled variables. The model equations for all compartments were solved using COMSOL Multiphysics (COMSOL, Inc. Burlington, MA, USA).

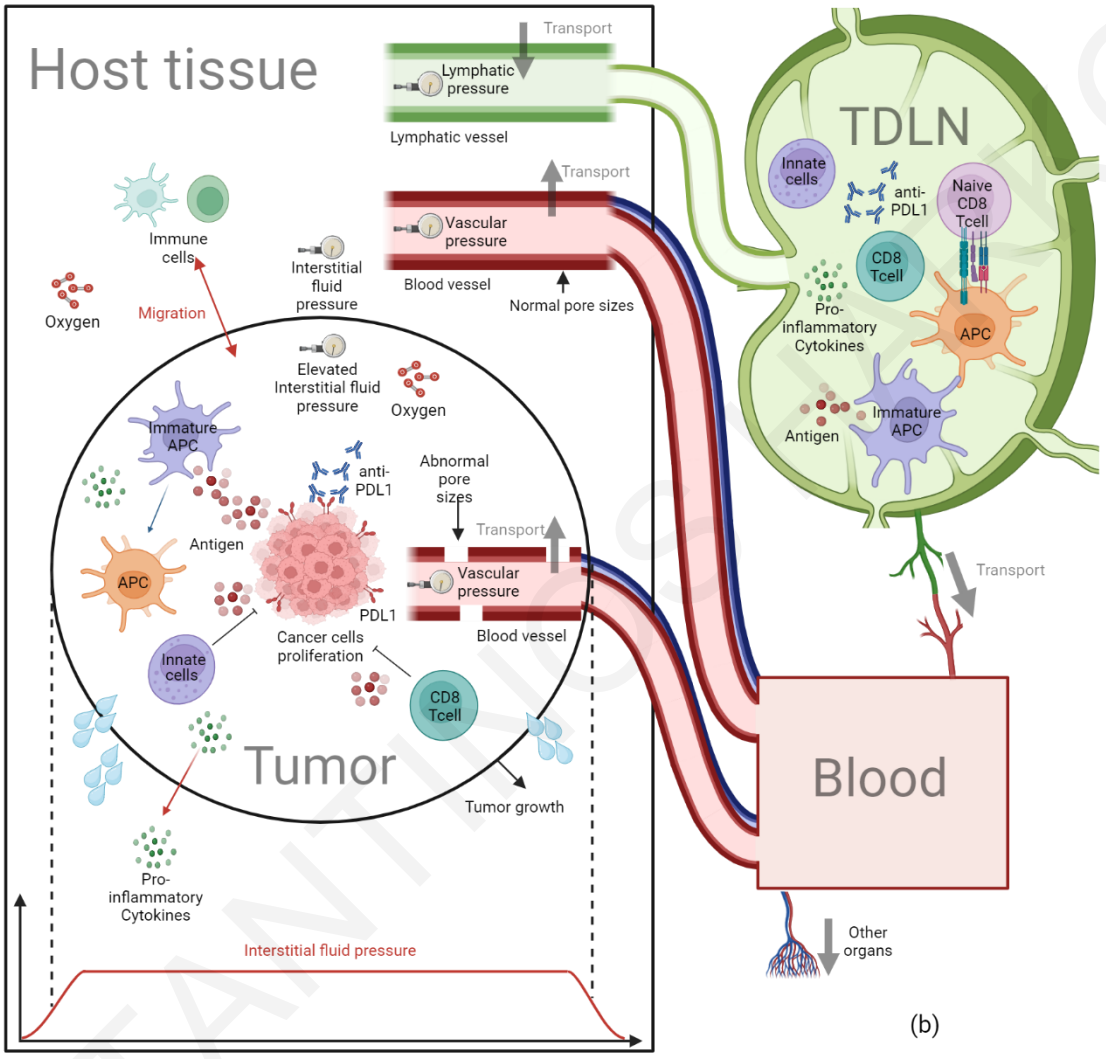

Figure 24: Schematic representation of the model. Transport of immune cells, cytokines and anti-PDL1 antibodies from the blood compartment to the tumor and host tissue through the vasculature and from the tumor and host tissue to the tumor draining lymph nodes through the lymphatic vessels. Modeling of the interstitial fluid pressure (IFP) which is elevated inside the tumor and also consideration of convective and diffusive transport across the vessels and between the tumor and host tissue. The model considers both adaptive and innate immune cells, antigen uptake and antigen presentation in the lymph nodes. Created with BioRender.com

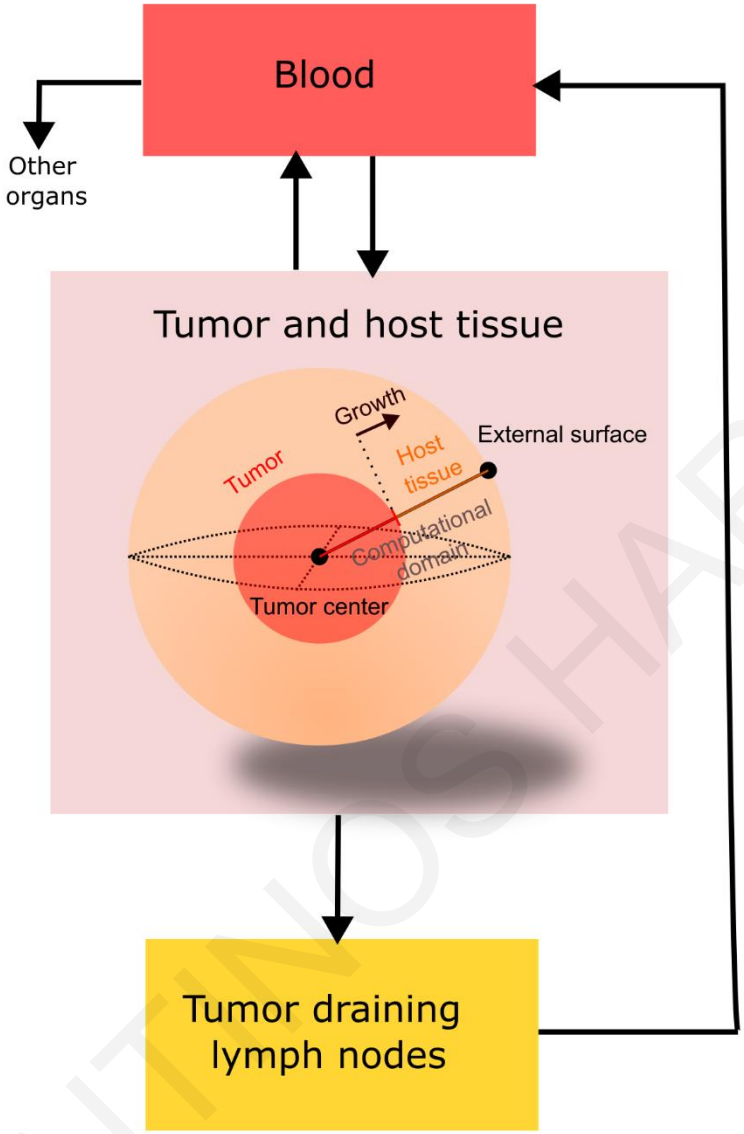

Figure 25: Schematic of the modeled compartments. In the blood and tumor draining lymph nodes a uniform distribution of modeled variables was assumed. Thus, ordinary differential equations were solved in contrast to the tumor and host tissue compartment where partial differential equations were applied. For the tumor - host tissue compartment spherical symmetry was assumed and thus it was solved in 1-dimension where the tumor grows as a sphere at the expense of the host tissue.

The tumor and host tissue domain were modeled as an 1D geometry with spherical symmetry (Figure 25). The left boundary of the 1D interval is the tumor center. Moving along the line and away from the tumor center, the tumor reaches the host tissue domain. At the center of the tumor, it was assumed that the density of cancer cells is at its maximum, subsequently

diminishing as we reach the host tissue through a step function. The area where the density of cancer cells surpasses a certain threshold (Table 13) is defined as the tumor region, while the region below this threshold belongs to the host tissue. Within this framework, the parameters transition from their aberrant tumor values to their normal values in correlation with the density of cancer cells, with the shift occurring at the threshold cancer cell density through the utilization of a step function with a transition zone. These step functions serve to ensure the continuity of the model variables. The tumor region expands or shrinks due to the deformation of the spatial frame mesh caused by changes in the concentration of the cancer cells.

Modeling of the immune system

We developed model equations to incorporate the most important functions of the immune cells. Due to the complexity of the immune system, we grouped the immune cells into certain groups and solved for a single variable for each group, as shown in Figure 24. One group are the innate cells that induce cytolysis. This category includes the cells of the innate immunity, such as the natural killer (NK) cells that can induce cytolysis to tumor cells. After the cytolysis of a tumor cell, antigen is produced. Antigen is transported to the tumor draining lymph nodes through the lymphatic vessels. Another category is the immature antigen presenting cells (IAPC) that includes cells like Dendritic cells and Macrophages, which can uptake tumor antigen and become antigen presenting cells (APC). APCs interact with the naïve CD8+ Tcells in tumor draining lymph nodes and become effector CD8+ Tcells. The effector CD8+ Tcells are cells of the adaptive immunity that in our case are activated specifically for targeting the tumor cells. The effector CD8+ Tcells are transported from the lymph nodes to the blood and then back to the tumor-host tissue domain through the blood vessels where they can kill cancer cells and produce more antigen.

Implementation of therapy

The model also considered intravascular injection of anti-PDL1 antibodies. Those antibodies are transported from the blood to the tumor - host tissue region and target the PDL1 receptor on the tumor cells. The PD-L1 on the surface of the tumor cells interacts with the PD-1 on the immune cells and suppresses their activity. Anti-PDL1 inhibits the association of PD-L1 with the PD-1, enhancing tumor cells killing by the immune cells. In the model, we

considered separately the concentration of the cancer cells which have anti-PDL1 bound on their receptors. These cancer cells with anti-PDL1 are more easily recognized and killed by the immune cells compared to the rest of the cancer cells.

As mentioned earlier anti-fibrotic medications, such as tranilast, enhances drug delivery by decompressing blood vessels and thus, improving perfusion. In the model, we assumed that anti-fibrotic medication induces an increase in the functional vascular density. The functional vascular density S_v is a continuous function that models the amount of the vascular surface area of the functional vessels per unit volume. The functional vessels transfer therapeutics in the tumor region as well as the immune cells and enhance antitumor immunity.

Optimization and reproduction of experimental data

To reproduce the experimental tumor growth data [184] shown in Figure 26, we employed an optimization algorithm using LiveLink for Matlab (The Mathworks, Inc., Natick, MA, United States). The optimization algorithm was used to derive parameters not found in literature, following a similar approach as previously [189]. In the experimental study, the normalization agent, tranilast, was employed for the treatment of breast (4T1, E0771), melanoma (B16F10) and fibrosarcoma (MCA205) tumors to enhance anti-PDL1 immunotherapy. The dataset includes the four different cancer cell lines. For each cell line (Figure 26), there is a control group that did not receive therapy (blue), a group that received anti-PDL1 treatment (red) and a group that received tranilast in combination with anti-PDL1 treatment (black).

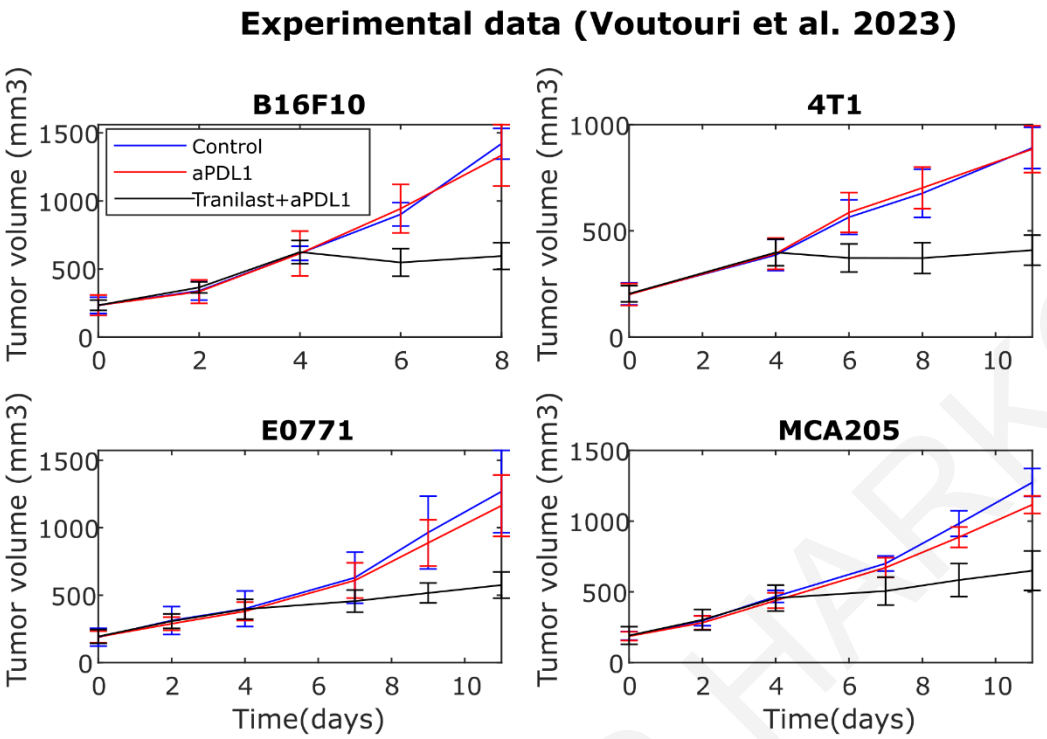

Figure 26: Experimental data used for model calibration/ parameter estimation from [184]. The data include murine breast (4T1, E0771), melanoma (B16F10) and fibrosarcoma (MCA205) tumors. For each cell line we use data from three different groups. A control group, a group that received anti-PDL1 treatment and another group that received combinational therapy of tranilast with anti-PDL1. The y axis represents the tumor volume in mm^3 and the x axis the time in days.

Parameters whose values could not be found in literature, were derived with the use of the optimization algorithm by fitting the model to the experimental data (Table 13). Assuming that various types of immune cells share the same values of the model parameters that they have in common, the number of parameters whose value has to be determined (Table 13) reduces drastically from tens of parameters to just a few. Furthermore, it was assumed that the immune system follows the same behavior in the four cell lines shown in Figure 26 and thus, the values of the model parameters were kept the same. Therefore, the optimization was applied to fit the experimental data of the four cell lines (Figure 26) simultaneously. This was done to calibrate the model parameters across many datasets rather than generating a set of parameters for each experiment with the use of fewer datapoints.

Blood compartment

Pro-inflammatory cytokines

The pro inflammatory cytokines inside the blood compartment are expressed as:

$$V_b \frac{dc^b}{dt} = -\iiint_{Vt} Q_{mc}\, dV_t + Q^{l\to b} c^l + \left(k_{In} In^b + k_{CD8} CD8^b - \delta_c c^b\right) V_b \tag{104}$$

where the first right-hand side term describes the transport between the blood and the tumor compartment. Q_{mc} describes the transport of cytokines across the vessel wall (in the tumor and host tissue compartment) and V_t is the volume of tumor and host tissue compartment. The second term describes the transport of cytokines from the lymphatic compartment to the blood. $Q^{l\to b}$ is the volumetric flow rate from lymph nodes to blood and c^l is the concentration of pro-inflammatory cytokines inside the tumor draining lymph nodes. The following terms describe the production of pro inflammatory cytokines by Innate immune cells and effector CD8+ Tcells. Where k_{In} and k_{CD8} are the production rates of pro-inflammatory cytokines by innate immune cells and effector CD8+ Tcells. In^b and $CD8^b$ are the concentrations of these cells inside the blood compartment. The last term describes the degradation of cytokines. V_b is the blood volume.

Innate cells

The innate immune cells that induce cytolysis inside the blood compartment are expressed as:

$$V_b \frac{dIn^b}{dt} = \lambda_{In}\left(\frac{c^b}{K_{cIn} + c^b}\right) V_b - \iiint_{Vt} z_{In}^{b\to t}\, T_f In^b dV_t + Q^{l\to b} In^l - \delta_{In} In^b V_b \tag{105}$$

where the first right-hand side term describes the production of innate cells, which depends on the concentration of pro-inflammatory cytokines inside the blood c^b. λ_{In} is a parameter describing the production of innate immune cells and K_{cIn} is the half saturation concentration. The second term describes the extravasation of innate cells from the blood to the tumor compartment. Where T_f trafficking function, $z_{In}^{b\to t}$is the extravasation rate constant.

The following term describes the transport of innate cells from the lymphatic compartment to the blood. The last term describes the degradation of the innate cells inside the blood where δ_{In} is the degradation rate constant.

Immature antigen presenting cells

The immature antigen presenting cells in the blood compartment are expressed as:

$$V_b \frac{dIAPC^b}{dt} = \lambda_{IAPC}\left(\frac{c^b}{K_{cAPC} + c^b}\right)V_b - \iiint_{Vt} z_{IAPC}^{b\to t}\, T_f IAPC^b dV_t + Q^{l\to b} IAPC^l - \delta_{IAPC} IAPC^b V_b \quad (106)$$

where the first right-hand side term describes production of immature antigen precenting cells. Λ_{IAPC} is a parameter describing the production of those cells and K_{cAPC} is the half saturation concentration. The second term describes the extravasation of immature antigen presenting cells from the blood to the tumor compartment. $z_{IAPC}^{b\to t}$ is the extravasation rate constant. The following term describes the transport of immature antigen presenting cells from the lymphatic compartment to the blood. The last term describes the degradation where δ_{IAPC} is the degradation rate constant.

Effector CD8+ Tcells

The effector CD8+ T cells inside the blood compartment are expressed as:

$$V_b \frac{dCD8^b}{dt} = -\iiint_{Vt} z_{CD8}^{b\to t}\, T_f CD8^b dV_t + Q^{l\to b} CD8^l - \delta_{CD8} CD8^b V_b \quad (107)$$

This equation follows the same approach with the equations of innate immune cells and immature antigen precenting cells except for the term of the production inside the blood due to that the effector CD8+ T cells are produced inside the lymph nodes due to antigen presentation.

Anti-PD-L1

The concentration of anti-PDL1 in the blood compartment is expressed as:

$$V_b \frac{aPDL1^b}{dt} = g_{aPDL1} V_b - \iiint_{Vt} Q_{ma}\, dV_t + Q^{l\to b} aPDL1^l - \delta_{aPDL1} aPDL1^b V_b \quad (108)$$

where the first right-hand side term describes the source of anti-PDL1. Where g_{aPDL1} is a source parameter. The second term is the transport of anti-PDL1 from the blood to the tumor. More specifically Q_{ma} describes the transport of anti-PDL1 across the vessel wall. In the same manner as the previous equations, the following term describes the transport from the tumor to the tumor draining lymph nodes to the blood and the last term describes the degradation of anti-PDL1 in the blood.

Tumor draining lymph nodes compartment

Pro-inflammatory cytokines

The pro inflammatory cytokines inside the tumor draining lymph nodes compartment system are expressed as:

$$V_l \frac{dc^l}{dt} = \iiint_{Vt} z_c^{t\to l} c^t dV_t - Q^{l\to b} c^l + \left(k_{In} In^l + k_{CD8} CD8^l + k_{APC} APC^l\right) V_l \quad (109)$$

where the first right-hand side term describes the transport between the tumor and the tumor draining lymph nodes. $z_c^{t\to l}$ is the rate constant of lymphatic drainage of pro-inflammatory cytokines inside tumor and host tissue compartment c^t. The following term describes the transport of cytokines from the lymphatic compartment to the blood. $Q^{l\to b}$ is the volumetric flow rate from the lymph nodes to the blood. The last terms describe the production of pro inflammatory cytokines by innate immune cells In^l, effector CD8+ Tcells $CD8^l$ and antigen presenting cells APC^l in the lymph nodes. The k parameters describe the rate of production of pro-inflammatory cytokines from each immune cell. V_l is the volume of the tumor draining lymph nodes.

Innate cells

The innate immune cells that induce cytolysis in the tumor draining lymph nodes are expressed as:

$$V_l \frac{dIn^l}{dt} = \iiint_{Vt} z_{In}^{t \to l} \, In^t dV_t - Q^{l \to b} In^l \tag{110}$$

where the first term describes the transport of innate cells from the tumor compartment to the tumor draining lymph nodes. $z_{In}^{t \to l}$ is the rate constant of lymphatic drainage of innate cells in the tumor and host tissue compartment In^t. The last term describes the transport of innate cells from the tumor draining lymph nodes to the blood compartment.

Immature antigen presenting cells

The immature antigen presenting cells in the tumor draining lymph nodes are expressed as:

$$\begin{aligned} V_l \frac{dIAPC^l}{dt} = & \iiint_{Vt} z_{IAPC}^{t \to l} \, IAPC^t dV_t - Q^{l \to b} IAPC^l \\ & - \chi_{APC} \left(\frac{c^l}{K_{cAPC} + c^l} \right) n_{A_g} IAPC^l A_g^l V_l \end{aligned} \tag{111}$$

where the first term describes the transport of immature antigen presenting cells from the tumor compartment to the tumor draining lymph nodes. $z_{IAPC}^{t \to l}$ is the rate constant of lymphatic drainage of immature antigen presenting cells inside tumor and host tissue compartment $IAPC^t$. The following term describes the transport of immature antigen presenting cells from the lymphatic system to the blood. The last term describes the reduction of immature antigen presenting cells due to activation. The activation of antigen presenting cells depends on the pro-inflammatory cytokines c^l and the interaction of immature antigen presenting cells $IAPC^l$ with antigen A_g^l inside the lymph nodes. N_{A_g} is the antigen uptake rate and χ_{APC} a parameter adjusting the activation of antigen precenting cells.

Antigen presenting cells

The antigen presenting cells in the tumor draining lymph nodes are expressed as:

$$\begin{aligned} V_l \frac{dAPC^l}{dt} = & \iiint_{Vt} z_{APC}^{t \to l} \, APC^t dV_t - \delta_{APC} APC^l V_l \\ & + \chi_{APC} \left(\frac{c^l}{K_{cAPC} + c^l} \right) n_{A_g} IAPC^l A_g^l V_l \end{aligned} \tag{112}$$

where the first term describes the transport of antigen presenting cells from the tumor compartment to the tumor draining lymph nodes. $z_{APC}^{t\to l}$ is the rate constant of lymphatic drainage of antigen presenting cells inside the tumor and host tissue compartment APC^{t}. The last terms describe the degradation (δ_{APC} the degradation rate constant) and source/production due to activation. The activation term of antigen presenting cells is the same as in Equation (111) with a plus sign. Because the activation decreases the immature antigen presenting cells and increases the antigen presenting cells

Antigen

The concentration of antigen in the tumor draining lymph nodes is expressed as:

$$V_l \frac{dA_g^l}{dt} = \iiint_{Vt} z_{Ag}^{t\to l} Ag^t dV_t - \delta_{A_g} A_g^l V_l - n_{A_g} IAPC A_g^l V_l \tag{113}$$

where the first right-hand side term describes the transport between the tumor and the tumor draining lymph nodes. $z_{Ag}^{t\to l}$ is the rate constant of lymphatic drainage of antigen inside tumor and host tissue compartment Ag^{t}. The last terms describe the degradation ($\delta_{A_g}$the degradation rate constant) and uptake by the immature antigen presenting cells.

Effector CD8+ Tcells

The effector CD8+ Tcells in the tumor draining lymph nodes are expressed as:

$$V_l \frac{dCD8^l}{dt} = \iiint_{Vt} z_{CD8}^{t\to l} CD8^t dV_t - Q^{l\to b} CD8^l + h_{CD8} APC^l CD8n V_l \tag{114}$$

where the first term describes the transport of effector CD8+ Tcells from the tumor compartment to the tumor draining lymph nodes. The following term describes the transport of effector CD8+ Tcells from the lymphatic system to the blood. The last term describes the source of effector CD8+ Tcells due to the antigen presentation by the antigen presenting cells to the I CD8+ Tcells $CD8n$. h_{CD8} is the activation rate constant of effector Tcells.

Anti-PD-L1

The concentration of anti-PDL1 in the tumor draining lymph nodes is expressed as:

$$V_l \frac{daPDL1^l}{dt} = \iiint_{Vt} z_{aPDL1}^{t\to l}\, aPDL1^t dV_t - Q^{l\to b} aPDL1^l \tag{115}$$

where the first term describes the transport of anti-PDL1 from the tumor compartment to the tumor draining lymph nodes. The second term describes the transport of anti-PDL1 from the lymphatic system to the blood.

Tumor and host tissue compartment

Pro-inflammatory cytokines

The pro inflammatory cytokines produced by the immune cells can be transported by convection and diffusion:

$$\begin{aligned}\frac{\partial c^t}{\partial t} + \boldsymbol{\nabla}\cdot\left(-D_{c^t}\boldsymbol{\nabla c^t} + \mathbf{v^f} c^t\right) &= Q_{mc} - z_c^{t\to l} c^t \\ &+ k_{In} In^t + k_{CD8} CD8^t + k_{APC} APC^t\end{aligned} \tag{116}$$

where the first and second right-hand side terms describe the transport between the blood and the tumor and between the tumor draining lymph nodes and the tumor, respectively. The last terms describe the production of pro inflammatory cytokines by innate immune cells In^t, effector CD8+ Tcells $CD8^t$ and antigen presenting cells APC^t in the tumor and host tissue compartment.

Transport of cytokines across the vessel wall

Transport across the vessel wall is based on Starling's Approximation:

$$Q_{mc} = P_{erc} S_v \left(c^b - c^t\right) + L_{pc} S_v (p_v - p_i)(1 - \sigma_{fc}) c^b \tag{117}$$

where $P_{erc}, S_v, L_{pc}, p_v, p_i, \sigma_{fc}$ are the vascular permeability of the cytokines, the vascular density, the hydraulic conductivity, the vascular pressure, the interstitial pressure and the reflection coefficient respectively. $c^b$and c^t are the concentrations of pro-inflammatory cytokines inside the blood and the tumor compartment respectively. The parameters L_{pc}, P_{erc} and σ_{fc} are expressed as a function of the vessel wall pores and the size of cytokines [41,190] :

$$L_p = \frac{\gamma r_0^2}{8\mu L_{vw}} \tag{118}$$

$$P_{erc} = \frac{\gamma H_c D_{0c}}{L_{vw}} \tag{119}$$

$$\sigma_{fc} = 1 - W_c \tag{120}$$

where γ is the fraction of the vessel wall surface area occupied by pores, r_0 the pore radius, μ the viscosity and L_{vw} the thickness of the vessel wall. H_c and W_c describe the steric and hydrodynamic interactions of cytokines with the pores of the vessel wall that hinder diffusive and convective transport respectively and D_{0c} is the diffusion coefficient of a particle in free solution given by the Stokes-Einstein equation. By ignoring electrostatic interactions H_c and W_c become [190]:

$$H_c = \frac{6\pi F}{K_{tc}} \tag{121}$$

$$W_c = \frac{F_c(2 - F_c)K_{sc}}{2K_{tc}} \tag{122}$$

where F_c is the partition coefficient expressed as:

$$F_c = (1 - \lambda_c)^2 \tag{123}$$

where λ_c is the ratio of the cytokines size to the vessel wall pore size and K_{tc} and K_{sc} are expressed as [190]

$$\binom{K_{tc}}{K_{sc}} = \frac{9}{4}\pi^2\sqrt{2}(1\text{-}\lambda_c)^{-5/2}\left[1 + \sum_{n=1}^{2}\binom{a_n}{b_n}(1\text{-}\lambda_c)^n\right] + \sum_{n=0}^{4}\binom{a_{n+3}}{b_{n+3}}{\lambda_c}^n \tag{124}$$

Innate cells

The innate immune cells that induce cytolysis in the tumor and host tissue are expressed as:

$$\frac{\partial In^t}{\partial t} + \boldsymbol{\nabla} \cdot (-D_{In^t}\boldsymbol{\nabla In^t} + \mathbf{v^s} In^t) = z_{In}^{b\to t} T_f In^b - z_{In}^{t\to l} In^t \tag{125}$$

where the first term describes the transport of innate cells from the blood compartment. The second term describes the transport to the tumor draining lymph nodes.

Immature antigen presenting cells

The immature antigen presenting cells in the tumor and host tissue are expressed as:

$$\frac{\partial \mathrm{IAPC^t}}{\partial \mathrm{t}} + \boldsymbol{\nabla} \cdot (-\mathrm{D_{IAPC^t}} \boldsymbol{\nabla} \mathbf{IAPC^t} + \mathbf{v^s} \mathrm{IAPC^t}) = \mathrm{z_{IAPC}^{b \to t} T_f IAPC^b} - \mathrm{z_{IAPC}^{t \to l} IAPC^t} - \chi_{\mathrm{APC}} \left(\frac{\mathrm{c^t}}{\mathrm{K_c + c^t}} \right) \left(\mathrm{n_{IAPC} IAPC^t \overline{T}} + \mathrm{w_a n_{IAPC} IAPC^t \overline{T}_L} + \mathrm{n_{A_g} IAPC^t A_g^t} \right) \quad (126)$$

where the first right-hand side term describes the transport of immature antigen presenting cells from the blood compartment and the second term describes the transport to the tumor draining lymph nodes. The last term describes the reduction of immature antigen presenting cells due to activation. The activation to antigen presenting cells depends on the pro-inflammatory cytokines $\mathrm{c^t}$and the interaction of immature antigen presenting cells $\mathrm{IAPC^t}$ with the tumor cells $\overline{\mathrm{T}}$, tumor cells with anti-PDL1 $\overline{\mathrm{T}}_{\mathrm{L}}$and antigen $\mathrm{A_g^t}$. $\mathrm{n_{IAPC}}$ and $\mathrm{n_{A_g}}$are the killing rate constant of tumor cells by immature antigen presenting cells and the antigen uptake parameter. $\mathrm{w_a}$ is the effectiveness of the killing of cancer cells bound by anti-PDL1 compared to cancer cells with free PDL1 receptors.

Antigen presenting cells

The antigen presenting cells in the tumor and host tissue are expressed as:

$$\frac{\partial \mathrm{APC}}{\partial \mathrm{t}} + \boldsymbol{\nabla} \cdot (-\mathrm{D_{APC}} \boldsymbol{\nabla} \mathbf{APC} + \mathbf{v^s} \mathrm{APC}) = -\mathrm{z_{APC}^{t \to l} APC^t} + \chi_{\mathrm{APC}} \left(\frac{\mathrm{c^t}}{\mathrm{K_c + c^t}} \right) \left(\mathrm{n_{IAPC} IAPC^t \overline{T}} + \mathrm{w_a n_{IAPC} IAPC^t \overline{T}_L} + \mathrm{n_{A_g} IAPC^t A_g^t} \right) \quad (127)$$

where the first right-hand side term describes the transport of antigen presenting cells to the tumor draining lymph nodes. The following term is a source term for the production of antigen presenting cells. The activation to antigen presenting cells is the same as the term of Equation (126) but with a positive sign.

Cancer cells

The concentration of cancer cells in the tumor and host tissue is expressed as:

$$\frac{\partial \overline{T}}{\partial t} + \boldsymbol{\nabla} \cdot \left(-D_{\overline{T}} \boldsymbol{\nabla} \overline{T} + \mathbf{v^s} \overline{T}\right) = R_{\overline{T}} =$$
$$k_1 \left(\frac{c_{ox}}{k_2 + c_{ox}}\right)\left(\overline{T} + \overline{T}_L\right) - \left(n_{In} In^t + n_{IAPC} IAPC^t + n_{CD8} CD8^t\right)\overline{T} \quad (128)$$
$$-k_{on} \overline{T} aPDL1^t + k_{off} \overline{T}_L$$

where the first right-hand side term describes the proliferation of the total cancer cells due to oxygen c_{Ox}. k_1 and k_2 are growth rate parameters. $\overline{T}_L$ are the cancer cells bound with anti-PDL1. The following term describes the killing of cancer cells by innate cells In^t, immature antigen presenting cells $IAPC^t$ and effector CD8+ Tcells $CD8^t$. With n we denote the killing rate parameter for each type of immune cell. The following term describes the binding of anti-PDL1 to the PDL1 receptors on the tumor cells and the last term describes the unbinding. Where k_{on} and k_{off} are the binding and unbinding rate constants and $aPDL1^t$ the concentration of anti-PDL1 in the tumor and host tissue compartment.

Cancer cells with anti-PDL1

The concentration of cancer cells with anti-PDL1 in the tumor and host tissue is expressed as:

$$\frac{\partial \overline{T}_L}{\partial t} + \boldsymbol{\nabla} \cdot \left(-D_{\overline{T}} \boldsymbol{\nabla} \overline{\mathbf{T}}_\mathbf{L} + \mathbf{v^s} \overline{T}_L\right) = R_{\overline{T}_L} = k_{on} \overline{T} aPDL1^t - k_{off} \overline{T}_L \quad (129)$$
$$-w_a \left(n_{In} In^t + n_{IAPC} IAPC^t + n_{CD8} CD8^t\right)\overline{T}_L$$

where the first right-hand side term describes the increase in cancer cells with anti-PDL1 due to the binding of anti-PDL1 to the available tumor cells. The following term describes the decrease due to unbinding. The last term describes the killing of cancer cells with anti-PDL1 by innate cells In^t, immature antigen presenting cells $IAPC^t$ and effector CD8+ Tcells $CD8^t$. w_a is a parameter describing how much more effective is the killing of cancer cells bound by anti-PDL1 compared to cancer cells with free PDL1 receptors.

Anti-PD-L1

The concentration of anti-PDL1 in the tumor and host tissue is expressed as:

$$\frac{\partial \mathrm{aPDL1^t}}{\partial \mathrm{t}} + \boldsymbol{\nabla} \cdot \left(-\mathrm{D_{aPDL1^t}} \boldsymbol{\nabla aPDL1^t} + \mathbf{v^f} \mathrm{aPDL1^t}\right) = \mathrm{Q_{ma}} - \mathrm{z_{aPDL1}^{t \to l}} \mathrm{aPDL1^t} - \mathrm{k_{on}} \overline{\mathrm{T}} \mathrm{aPDL1^t} + \mathrm{k_{off}} \overline{\mathrm{T}}_{\mathrm{L}} \quad (130)$$

where the first right-hand side term describes the transport of anti-PDL1 from the blood to the tumor and the last term the transport from the tumor to the tumor draining lymph nodes. The last two terms describe the decrease in anti-PDL1 due to the binding of anti-PDL1 to the available tumor cells and the decrease due to the unbinding.

Transport of anti-PDL1 across the vessel wall

Transport of anti-PDL1 across the vessel wall is given by the same set of equations as Equations (117)-(124) for the transport of cytokines.

Antigen

The concentration of antigen in the tumor and host tissue is expressed as:

$$\frac{\partial \mathrm{A_g^t}}{\partial \mathrm{t}} + \boldsymbol{\nabla} \cdot \left(-\mathrm{D_{A_g^t}} \boldsymbol{\nabla A_g^t} + \mathbf{v^f} \mathrm{A_g^t}\right) = -\mathrm{z_{Ag}^{t \to l}} \mathrm{Ag^t} + (\mathrm{n_{In}} \mathrm{In^t} + \mathrm{n_{CD8}} \mathrm{CD8^t}) \overline{\mathrm{T}} + \mathrm{w_a} (\mathrm{n_{In}} \mathrm{In^t} + \mathrm{n_{CD8}} \mathrm{CD8^t}) \overline{\mathrm{T}}_{\mathrm{L}} - \mathrm{n_{A_g}} \mathrm{IAPC^t} \mathrm{A_g^t} \quad (131)$$

Where the first and second right-hand side terms describe the transport between the tumor draining lymph nodes and the tumor. The following two terms describe the production of antigen induced by the cytolytic effect of innate cells $\mathrm{In^t}$ and effector CD8+ T cells $\mathrm{CD8^t}$ to the tumor cells $\overline{\mathrm{T}}$ and tumor cells with anti-PDL1 $\overline{\mathrm{T}}_{\mathrm{L}}$. The last term describes the antigen uptake by the immature antigen presenting cells.

Effector CD8+ Tcells

The effector CD8+ Tcells in the tumor and host tissue are expressed as:

$$\frac{\partial \mathrm{CD8^t}}{\partial \mathrm{t}} + \boldsymbol{\nabla} \cdot (-\mathrm{D_{CD8^t}} \boldsymbol{\nabla CD8^t} + \mathbf{v^s} \mathrm{CD8^t}) = \mathrm{z_{CD8}^{b \to t}} \mathrm{T_f} \mathrm{CD8^b} - \mathrm{z_{CD8}^{t \to l}} \mathrm{CD8^t} \quad (132)$$

where the first term of the right hand side describes the transport of effector CD8+ Tcells from the blood compartment. The second term describes the transport to the tumor draining lymph nodes.

Oxygen transport

The rate of change of oxygen concentration in the tissue was modeled with a convection diffusion equation that includes a source and a sink term [118,151], . The source term is due to oxygen supply from the blood vessels and the sink term describes oxygen consumption by cancer cells:

$$\frac{\partial c_{ox}}{\partial t} + \boldsymbol{\nabla} \cdot \left(-D_{ox}\boldsymbol{\nabla c_{ox}} + \mathbf{v^f} c_{ox}\right) = -\frac{A_{ox} c_{ox}}{c_{ox} + k_{ox}} \frac{\overline{T}}{\overline{T_0}} + P_{erox} S_v (c_{iox} - c_{ox}) \tag{133}$$

where A_{ox} and k_{ox} are oxygen uptake parameters, c_{iox} is the oxygen concentration in the vessels, $\overline{T_0}$ is the initial concentration of cancer cells and P_{erox} is the vascular permeability of oxygen defined as the oxygen diffusion coefficient divided by the length of the vessel wall.

Kinematics of tumor growth

The growth stretch ratio is calculated as [191]

$$3\frac{1}{\lambda_g}\frac{d\lambda_g}{dt} = \frac{R_{\overline{T}_L} + R_{\overline{T}}}{\overline{T_0}} \tag{134}$$

where λ_g is the growth stretch ratio $R_{\overline{T}}$ the rate of change of the concentration of cancer cells and $R_{\overline{T}_L}$ the rate of change of the concentration of cancer cells with anti-PDL1. $\overline{T_0}$ is the initial concentration of cancer cells. The tumor growth is implemented using deformation of the spatial frame mesh relative to the material frame mesh with a prescribed mesh displacement of [189]

$$\mathbf{d_x} = \mathbf{x} - \mathbf{X} = \lambda_g \mathbf{X} - \mathbf{X} \tag{135}$$

where $\mathbf{x}$ the spatial frame coordinates and $\mathbf{X}$ the material frame coordinates. The solid velocity is calculated as:

$$\mathbf{v^s} = \frac{d\mathbf{x}}{dt} \tag{136}$$

where t is the time.

Interstitial pressure-fluid velocity

Normal and tumor tissues have properties like those of a porous medium. According to Darcy's law and the mesh movement due to solid velocity, the interstitial fluid velocity is given by [189]:

$$\mathbf{v^f} = -k_{th}\mathbf{\nabla p_i} + \mathbf{v^s} \tag{137}$$

where k_{th} is the hydraulic conductivity of the interstitial space [192]. The mass balance gives [11,155]

$$\mathbf{\nabla \cdot v^f} = L_p S_v(p_v - p_i) - L_{pl} S_{vl}(p_i - p_{vl}) \tag{138}$$

The first term on the right-hand side of the equation describes the fluid flux entering from the blood vessels and the second term the flux exiting through the lymphatic system. L_p is the blood vessels' hydraulic conductivity, S_v the vascular density and p_v is the vascular pressure. L_{pl}, S_{vl} and p_{vl} are the corresponding parameters for the lymphatic vessels [143].

Trafficking of immune cells

Normalization of the tumor micro-environment increases trafficking of immune cells when combined with immunotherapy. When the vascular density doubles from 50cm^{-1} to 100cm^{-1} the source of immune cells increases by 1.367 [156]. By assuming that the function is 1 for the host tissue value of (70cm^{-1}). The trafficking function reads [156]:

$$T_f = 0.0273Sv - 0.9138 \tag{139}$$

where S_v represents the functional vascular density measured in cm^{-1}.

Molecular radius of agonist

The radius R of transported agonist is expressed as [154]:

$$\log_{10}R = -0.31 + 0.43\log_{10}M_w \tag{140}$$

where M_w is the molecular weight of agonist.

Boundary Conditions

Tumor center boundary conditions

Due to the symmetry at the tumor center of the 1D geometry with spherical symmetry no flux boundary conditions were used thus no diffusive or convective transport. No flux boundary conditions were applied to all partial differential equations.

$$-\mathrm{D}_{\mathrm{c_{ox}}}\boldsymbol{\nabla c_{ox}} + \mathbf{v^f}\mathrm{c_{ox}} = 0 \tag{141}$$

$$-\mathrm{k_{th}}\boldsymbol{\nabla p_i} + \mathbf{v^s} = 0 \tag{142}$$

$$-\mathrm{D_{In}}\boldsymbol{\nabla In^t} + \mathbf{v^s}\mathrm{In^t} = 0 \tag{143}$$

$$-\mathrm{D_{IAPC}}\boldsymbol{\nabla IAPC^t} + \mathbf{v^s}\mathrm{IAPC^t} = 0 \tag{144}$$

$$-\mathrm{D_c}\boldsymbol{\nabla c^t} + \mathbf{v^f}\mathrm{c^t} = 0 \tag{145}$$

$$-\mathrm{D_{CD8}}\boldsymbol{\nabla CD8^t} + \mathbf{v^s}\mathrm{CD8^t} = 0 \tag{146}$$

$$-\mathrm{D_{APC}}\boldsymbol{\nabla APC^t} + \mathbf{v^s}\mathrm{APC^t} = 0 \tag{147}$$

$$-\mathrm{D_{\overline{T}}}\boldsymbol{\nabla \overline{T}} + \mathbf{v^s}\overline{\mathrm{T}} = 0 \tag{148}$$

$$-\mathrm{D_{\overline{T}_L}}\boldsymbol{\nabla \overline{T}_L} + \mathbf{v^s}\overline{\mathrm{T}}_{\mathrm{L}} = 0 \tag{149}$$

$$-\mathrm{D_{A_g}}\boldsymbol{\nabla A_g^t} + \mathbf{v^f}\mathrm{A_g^t} = 0 \tag{150}$$

External surface boundary conditions

For the external surface of the host tissue the boundary condition of oxygen was assumed to have the constant value of the normal tissue.

$$\mathrm{c_{ox}} = \mathrm{c_{iox}} \tag{151}$$

No flux boundary condition was also applied for the fluid pressure, according to Darcy's law and the domain deformation by the solid velocity, $\mathbf{v^s}$.

$$-k_{th}\nabla \mathbf{p_i} + \mathbf{v^s} = 0 \quad (152)$$

No flux boundary conditions were applied for the cytokines, the innate immune cells that induce cytolysis In^t, the immature antigen presenting cells $IAPC^t$, the effector CD8+ Tcells $CD8^t$ and the cytokines c^t. This was done because it was assumed that there is no mass flux of these concentrations at the external surface.

$$-D_{In}\nabla \mathbf{In^t} + \mathbf{v^s}In^t = 0 \quad (153)$$

$$-D_{IAPC}\nabla \mathbf{IAPC^t} + \mathbf{v^s}IAPC^t = 0 \quad (154)$$

$$-D_{IAPC}\nabla \mathbf{CD8^t} + \mathbf{v^s}CD8^t = 0 \quad (155)$$

$$-D_c\nabla \mathbf{c^t} + \mathbf{v^f}c^t = 0 \quad (156)$$

The external surface is not reached by the cancer cells. Thus, the cancer cells density was assumed to be equal to zero as well as all the antigen and antigen precenting cells that depend on the existence of tumor cells.

$$APC^t = 0 \quad (157)$$

$$\overline{T} = 0 \quad (158)$$

$$\overline{T}_L = 0 \quad (159)$$

$$A_g^t = 0 \quad (160)$$

Results

Model calibration

To calibrate our model, we used the optimization algorithm to reproduce the set of experimental tumor growth data shown in Figure 26 [184]. The reproduction of experimental data with the model is shown in Figure 27. Using the optimization algorithm, we generated a set of parameters that reproduce these data with good accuracy (Table 13). Due to the different growth rates among cell lines, we used a different value for the growth rate

parameter of each cell line. For the groups that received anti-PDL1 treatment, we switched on the equations related to anti-PDL1. For the groups that also received tranilast, we increased the value of the functional vascular density for each cell line. Our algorithm predicts an increase in the functional vascular density of 3-5 times (Table 13). This is validated with experimental measurements of tumor perfusion where the administration of tranilast increased perfusion by the same factor [184]. Administration of only immunotherapy, not accompanied by the normalization agent (tranilast) did not have a significant impact on tumor growth. However, when ICB was combined with tranilast, a significant decrease in tumor growth was observed. The model predicted well the experimental tumor growth curves for all tumor types and conditions.

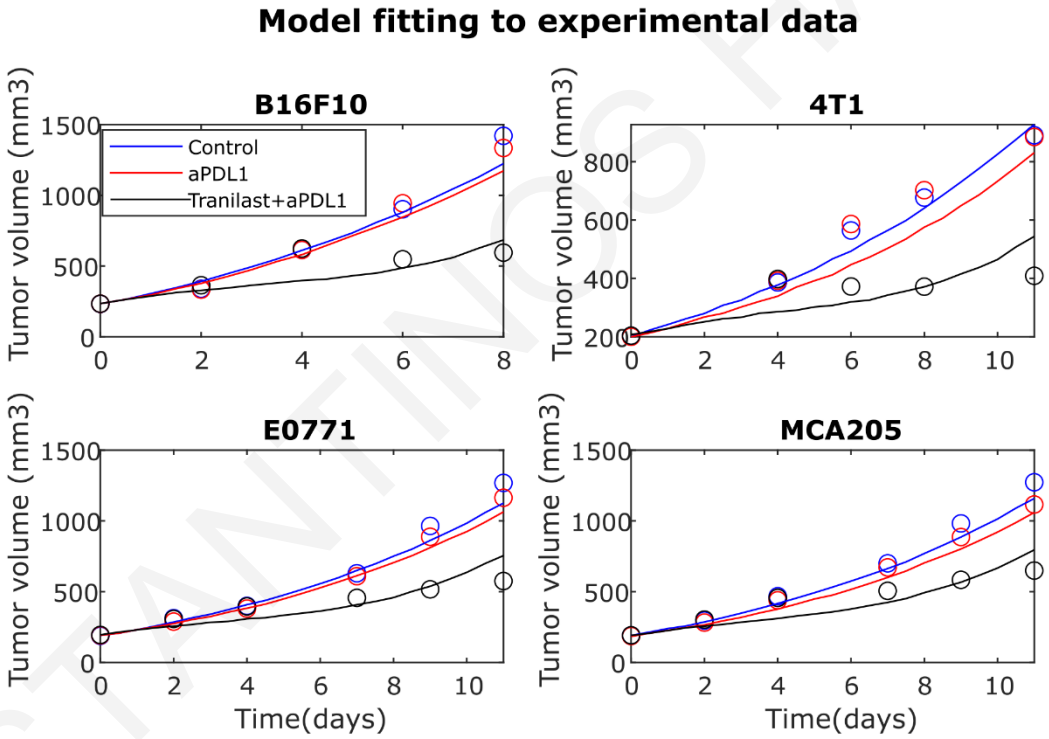

Figure 27: Model calibration with tumor growth curves of 4 different cell lines. The continuous lines represent the model predictions and the bullets the experimental results [184]. With blue color is the control group that did not receive therapy. With red color is a group thar received anti-PDL1 treatment and with black the group that received combinational therapy of tranilast and anti-PDL1. The model reproduces the results with an accuracy of Root mean square error (RMSE)=91, 88, and 113 for the control, anti-PDL1, anti-PDL1 + tranilast groups for the B16F10 tumors. With an accuracy of

RMSE=39, 91, 83 for the respective groups of 4T1 tumors, RMSE=73, 52, and 87 for E0771 and RMSE=66, 57, and 93 for MCA205.

Immune system response

As shown in Figure 28, due to the hyper-permeability of the tumor blood vessels the IFP is elevated in the tumor interior[2,140]. IFP reaches the value of the vascular pressure inside the tumor and decreases at the tumor margin. We observe at the control and anti-PDL1 cases that the region with IFP values the same as the vascular pressure (2 kPa) increases through time. In the case of tranilast and anti-PDL1 treatment at day 10, we observe a decrease in the region of elevated IFP. Due to the significant decrease in tumor volume in this group and boundary effects of the host tissue, where IFP is zero, the IFP in the tumor does not reach the levels of the vascular pressure.

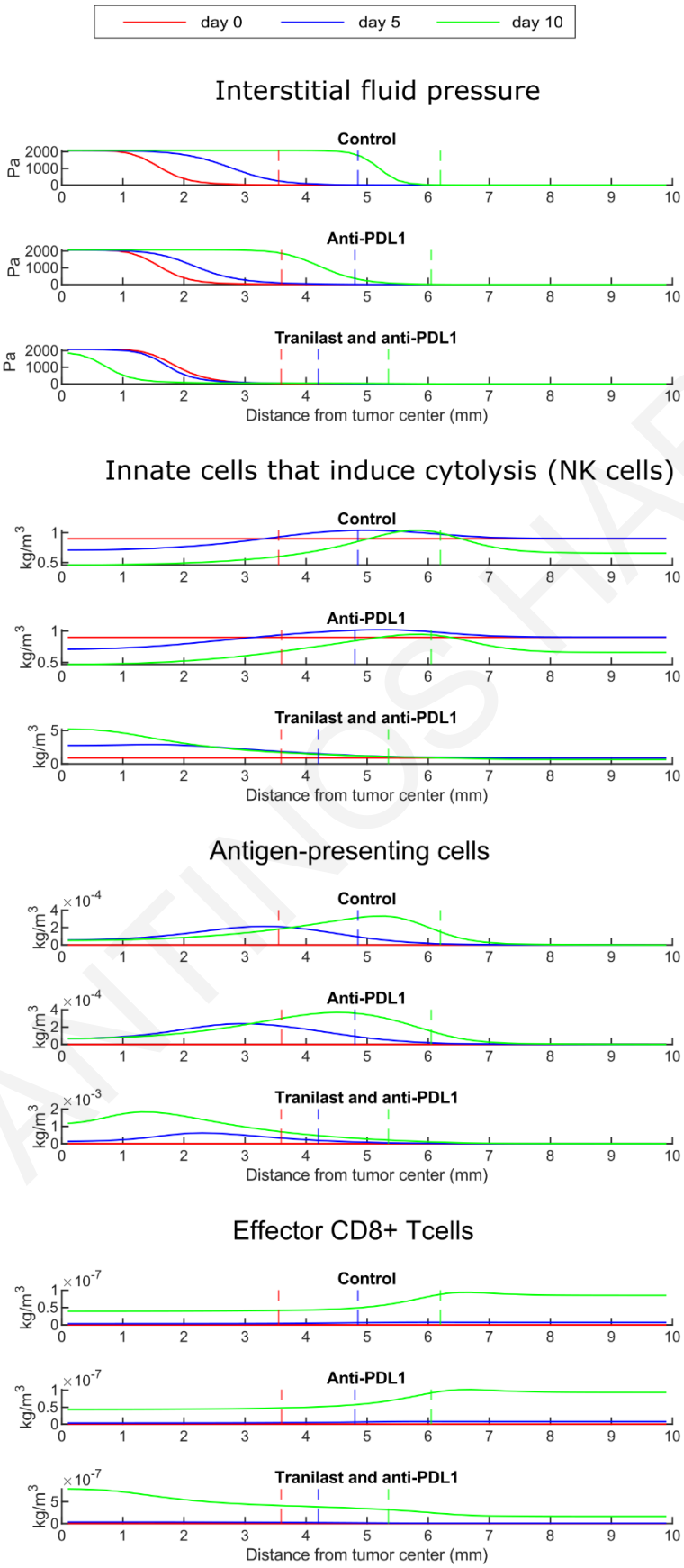

Figure 28: Distributions of the interstitial fluid pressure (IFP) and the concentrations of innate cells that induce cytolysis, Antigen presenting cells (APC) and Effector CD8+ Tcells for various time points. The x axis represents the distance from the tumor center with 0 being the tumor center. As we move along the axis, we reach the host tissue. The dashed lines show the tumor margin. The figure represents the results of the case of E0771 cell line which is the case with the highest fitting accuracy. The figure shows all 3 modeled groups: control group, the group thar received anti-PDL1 and the group which received combinational therapy (tranilast and anti-PDL1)

Furthermore, in contrast to the control and anti-PDL1 cases, the combined therapy increases the concentration of innate immune cells that induce cytolysis, such as NK cells on the left of the domain, at the tumor center. This can also be observed for the APCs. Additionally, there is an increase in the concentration of effector CD8+ Tcells inside the tumor region in the combinational therapy in contrast to the other groups where we observe larger amounts of CD8+ Tcells in the host tissue rather than the tumor region.

Impact of modeled components to treatment outcomes

Next, we investigated how model parameters related to properties of the tumor microenvironment and the binding affinity of the ICB antibodies affect treatment outcomes. We kept our baseline parameters (Table 13) and vary a single parameter at a time to generate the results of Figure 29 to Figure 32. The baseline values used are the values from the fitting of the model to the data for the E0771 tumors for the combinational therapy case. We used this cell line because the model reproduced the experimental data with the highest accuracy compared to the other cell lines. In Figure 29, we observe that increases in the functional vascular density can lead even to complete cure (Sv=200[1/cm]) where the tumor volume reaches zero. In this case the mass of the immune cells inside the tumor initially increases causing a robust anti-tumor immune response and then due to the reduction of the tumor domain, the mass of the immune cells reduces. The increase in the size of the pores of the tumor vessels from a radius of 10nm to 100nm and 200nm [144] , causes a slight decrease in the tumor volume because on one hand the increase in pore size allow for a larger amount of anti-PDL1 antibodies to pass through the larger pores but on the other hand the increase in pore-size would increase IFP, which hinders convective transport across the vessel wall

pores (Figure 30). This induces an increase in the mass of APCs and effector CD8+ Tcells inside the tumor.

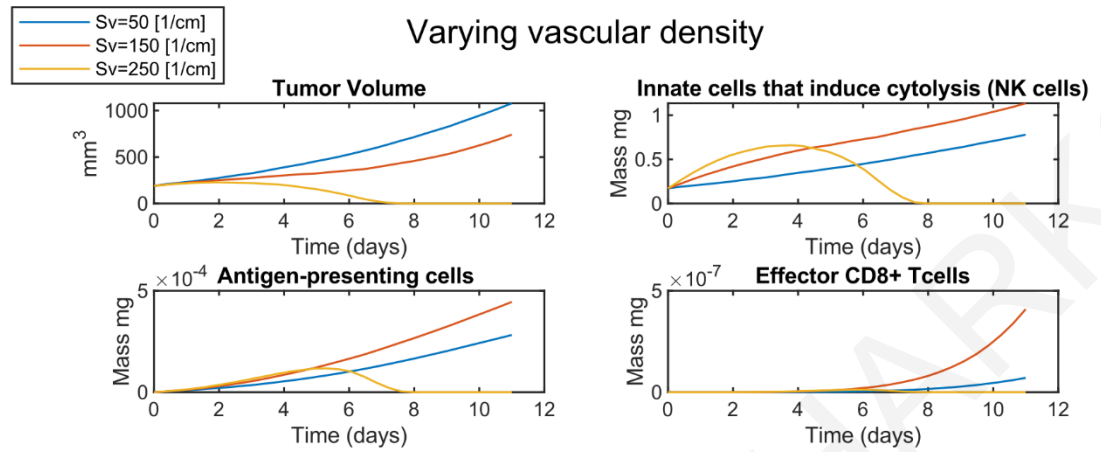

Figure 29: Parametric analysis the functional vascular density inside the tumor region (Sv),. The baseline values are the values from the fitting of the model to the data for the E0771 tumors and for the combinational therapy case. The figure represents the tumor volume and the mass inside the tumor of innate immune cells that induce cytolysis, APCs and effector CD8+Tcells.

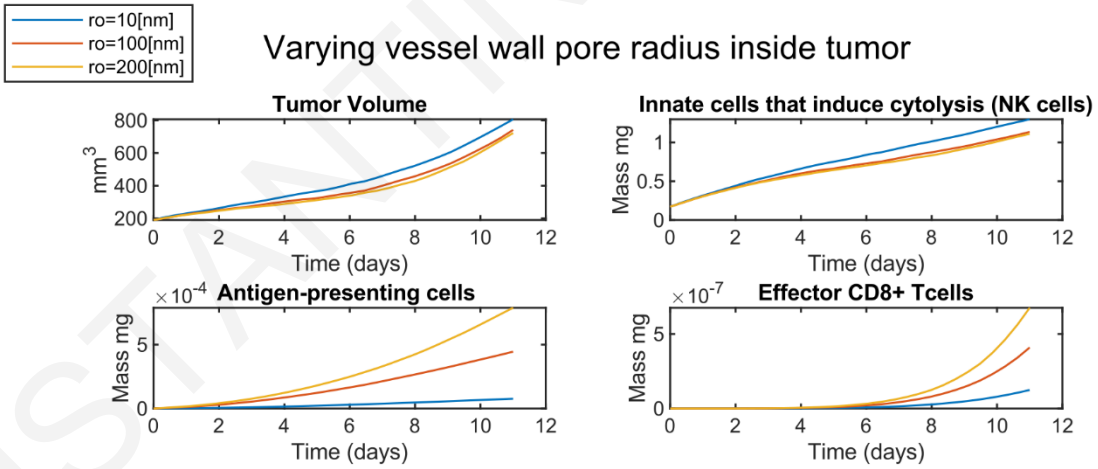

Figure 30: Parametric analysis for the vessel wall pore radius (r0). The baseline values are the values from the fitting of the model to the data for the E0771 tumors and for the combinational therapy case. The figure represents the tumor volume and the mass inside the tumor of innate immune cells that induce cytolysis, APCs and effector CD8+Tcells.

Next, we varied the ability of the anti-PDL1 drug to bind on the PDL1 ligand of the tumor cells from 1 to $1x10^6$[m3/mol/s] [145]. We observe a slight decrease in tumor growth when the binding is increased. Interestingly increasing the binding to more than 1 $x10^3$[m3/mol/s] does not seem to have an impact to tumor growth (Figure 31). In addition, increasing the amount of anti-PDL1 antibodies administered can lead to complete elimination of the tumor (Figure 32). In the case of complete treatment, the mass of the immune cells increases and then goes to zero due to the reduction of the tumor domain in a similar fashion as the case of increased functional vascular density.

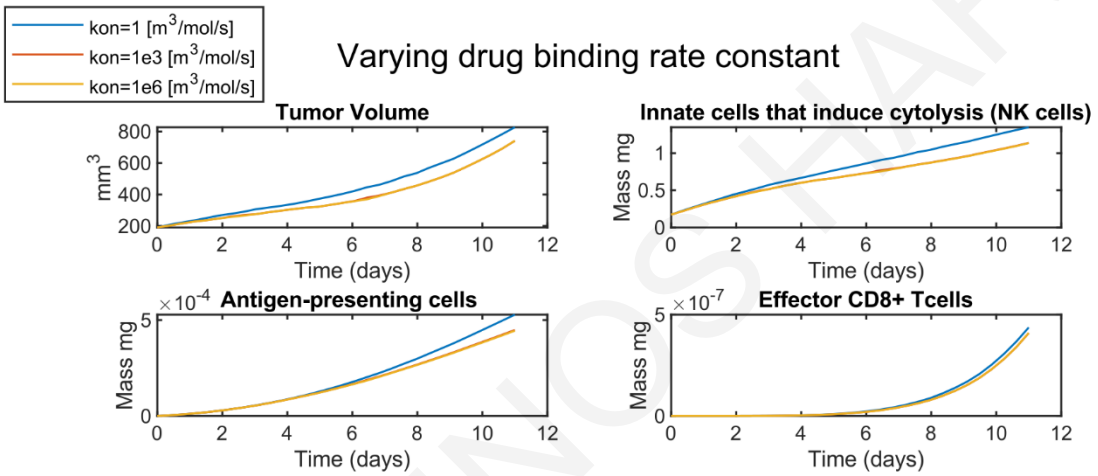

Figure 31: Parametric analysis for the binding rate constant of anti-PDL1 to the PDL1 of the tumor cells. The baseline values are the values from the fitting of the model to the data for the E0771 tumors and for the combinational therapy case. The figure represents the tumor volume and the mass inside the tumor of innate immune cells that induce cytolysis, APCs and effector CD8+Tcells.

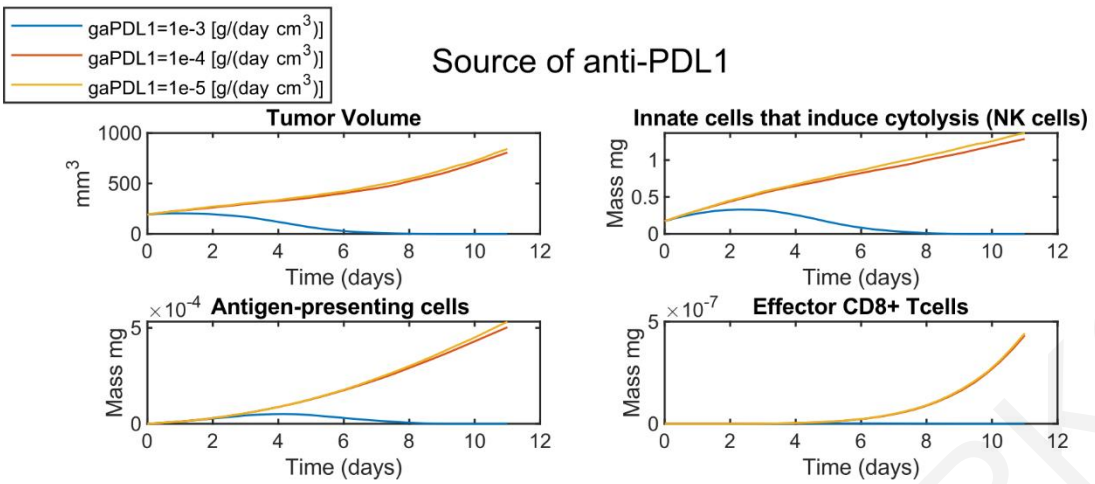

Figure 32: Parametric analysis the amount of anti-PDL1 administered (gaPDL1). The baseline values are the values from the fitting of the model to the data for the E0771 tumors and for the combinational therapy case. The figure represents the tumor volume and the mass inside the tumor of innate immune cells that induce cytolysis, APCs and effector CD8+Tcells.

Discussion

In this study, we modeled the interactions of immune cells and cancer cells by considering the tumor draining lymph nodes. The model was able to reproduce experimental data of four different tumor models that included a group that didn't received therapy a group that received ICB therapy and a group that received combinational therapy of ICB and normalization treatment. Our model predictions agree with experimental observations where the combinational therapy increased perfusion by 3-5 times [184]. It also agrees with previous studies that show a decrease in IFP due to the combinational therapy[177].

Furthermore, the model predicts the immune system profiling, which is hard to measure experimentally. It shows that combinational therapy increases the amount of innate and adaptive immune cells in the tumor center in contrast with the case of immunotherapy alone where the immune cells reach the tumor periphery rather than the tumor center. The number of functional vessels inside the tumor is also a crucial factor. The model predicts a reduction in tumor growth and even tumor elimination in tumors where more functional vessels exist. The size of the vessels' pores also affects treatment outcomes, with larger pores leading to larger amounts of APCs and CD8+ Tcells inside the tumor. Also developing drugs with

higher binding ability to cancer cells can increase the efficacy of the treatment although the model suggests that there is a limit where increasing the binding does not further improve treatment. Furthermore, increasing the amount of anti-PDL1 administered increases the intratumoral levels of anti-PDL1 and thus, which decreases further tumor volume.

Although our model provides valuable insights, it also has its limitations. We assumed that the tumor grows as a sphere and solved for spherical symmetry. The vessel wall pore radius was assumed to be uniform, which may not always be true because there is typically a distribution of pore sizes. Additionally, we did not consider variations in the diffusion coefficient of the ICBs based on tumor type. We also assumed no activated immune cells at the beginning of the simulation, which might not be the case. We also did not consider the impact of immune cells releasing immunosuppressive cytokines and avoided the consideration of more types of immune cells because that would introduce more unknown parameters. In addition, to reduce the amount of unknown parameters and to increase the number of datasets used for the parameters estimation, we assumed that the different types of immune cells share the same values of the parameters that they have in common, and that these values are the same among the four cell lines that were used for the calibration of the model. This assumption, however, might not always be the case. Additionally, if experimental data of the immune system derived as concentrations of cells in the tumor and host tissue volume existed, that could have enabled further validation of our model predictions. In conclusion, although we could make modifications to our model to account for some of these factors, doing so would likely only result in quantitative changes to our findings, leaving the overall conclusions of our study unaffected.

Chapter 5: Dissecting the impact of the gut microbiome on cancer immunotherapy

This study is in revision in the journal Nature Computational Science: Hadjigeorgiou GA[*], Harkos C[*], Mishra AK, Morad G, Johnson SB, Ajami NJ, Wargo JA, Munn LL, Stylianopoulos T and Jain RK. Dissecting the impact of the gut microbiome on cancer immunotherapy. Nature Computational Science. [*] Equal contribution. https://doi.org/10.21203/rs.3.rs-3647386/v1

Summary

The gut microbiome has emerged as a key regulator of response to cancer immunotherapy. However, there is a gap in our understanding of the underlying mechanisms by which the microbiome influences immunotherapy. To this end, we developed a mathematical model based on i) gut microbiome data derived from preclinical studies on melanomas after fecal microbiota transplant, ii) mechanistic modeling of antitumor immune response, and iii) robust association analysis of murine and human microbiome profiles with model-predicted immune profiles. Using our model, we could distill the complexity of these murine and human studies on microbiome modulation in terms of just two model parameters: the activation and killing rate constants of immune cells. We further investigated associations between specific bacterial taxonomies and antitumor immunity and immunotherapy efficacy. This model can guide the design of studies to refine mechanistic links between the microbiome and immune system.

Introduction

ICBs have transformed cancer treatment. To date eight different ICBs have been approved alone or in combination with other therapies for ~80 indications [19]. However, less than 20% of patients currently benefit from these treatments [23]. Moreover, many patients develop immune-related adverse events, some of which can be fatal [24]. The abnormal and immunosuppressive TME not only hinders the delivery of ICBs, but also renders them ineffective once they accrue in tumors [163]. An emerging approach to overcome this challenge is to reprogram the host microbiome [193,194].

The impact of the gut microbiome on immunotherapy outcome has been studied across several types of cancers [26,27,195–198], and an increasing number of clinical and preclinical studies have shown that the diversity, composition, and structure of the gut microbiome is associated with response and resistance to ICB [27,28]. Furthermore, recent experimental trials have demonstrated how FMTs can overcome resistance to ICBs [25,28–33]. Despite the strong evidence for the effects of the microbiome on the immune cells and the efficacy of ICBs, little is known about the underlying mechanisms [197]. Limited information and lack of consistency among studies about the positive or negative effects of specific bacteria on ICB efficacy highlight the need to understand how gut microbes affect ICB response.

Mathematical models have enhanced our understanding of not only tumor biology, but also that of other diseases [42,150,199,200]. For instance, mathematical models have been developed for the investigation of interactions among populations of microbes, determining which populations can prevail over others [201–203]. There are also models focusing on interactions among a small number of bacteria and specific populations of immune cells [204,205] or the interactions of the immune system with tumors [42]. Other models have investigated how interactions between cancer cells and immune cells influence the efficacy of immunotherapy for cancer as well as for cancer patients who have contracted COVID [145,199]. However, to our knowledge, none of the existing modeling frameworks have analyzed the effect of the microbiome on cancer immunotherapy. Elucidating the role of the microbiome on cancer immunotherapy requires an in-depth investigation of i) the mechanisms by which the microbiome affects activation of cells of both the innate and adaptive immune systems and ii) the positive or negative effects of the various bacterial taxa on immune effector cell function. A fundamental understanding of these processes has the potential to inform new therapeutic strategies. This task is challenging though, as it requires a detailed mathematical framework based on robust experimental data.

Here we developed a mathematical model of immune checkpoint blockade therapy to investigate the possible mechanisms by which the microbiome influences the immune system. The model accounts explicitly for interactions among cancer cells, adaptive immunity (i.e., CD4+, CD8+ T cells, regulatory T cells, and B cells), innate immunity (i.e.,

immature dendritic cells, neutrophils, natural killer cells, and macrophages) and cytokines [145,199,206–208] (see

Table 14 for a list of the model variables). We hypothesize that the gut microbiome affects the immune cells through two distinct processes: their activation and killing efficiency. These processes are incorporated through an activation rate, A_{rc} and a killing rate, K_{rc} (Figure 33). The values of most model parameters were taken from the literature (

Table 15). For unknown parameters related to the growth of the tumor and the effects of immunotherapy, the baseline values (Table 16) were determined by an optimization procedure to reproduce the average experimental tumor growth curves from relevant mouse studies [25,28,31]. We then used the model to simulate data from a FMT clinical trial in melanoma patients who progressed on immunotherapy prior to FMT [30] and murine models developed to evaluate the impact of responder and non-responder FMT on antitumor response [31] for which complete microbiome profiles were available. These simulations yield mechanistic insights about immune cell dynamics in individual subjects. Finally, we performed an association analysis between the immune profiles predicted by our model and the microbiome profile data to discover potential positive and negative dependencies among specific microbial populations and components of the immune system (Figure 33).

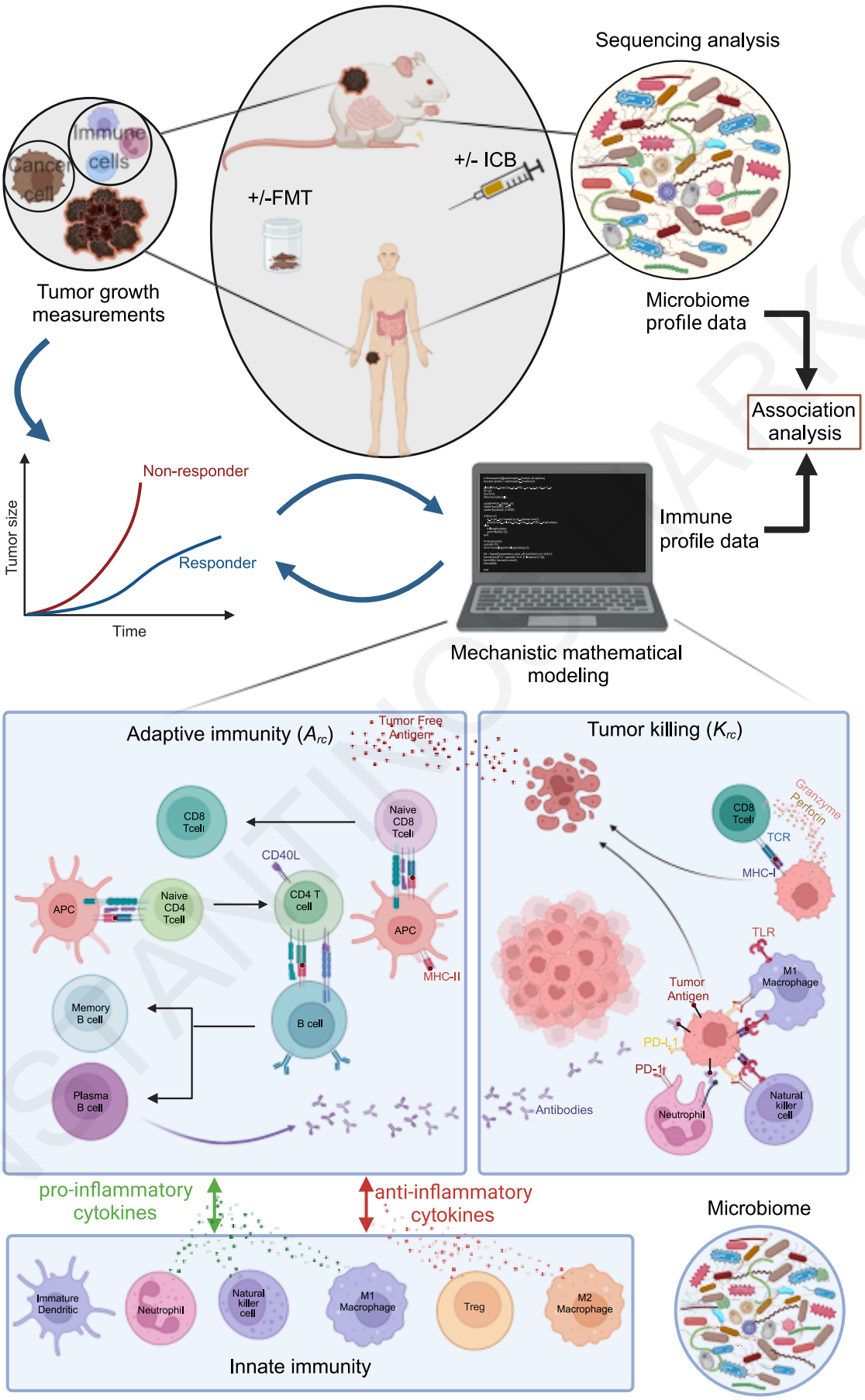

Figure 33: Description of the approach followed in this study to relate immune profiling with microbiome data and schematic of mathematical model components. Our approach involves the reproduction of tumor growth curves with the deterministic mathematical model to calibrate model parameters. The tumor growth data as well as the microbiome profiling data are derived from clinical and preclinical studies on melanomas after fecal microbiota transplant and administration of immunotherapy. The deterministic model generates the immune profile data for each tumor and the predicted immune profile is associated with the experimentally derived microbiome profiling data. Schematic of mathematical model's components. The arrows represent the interactions among model components. The intensity of each interaction is associated with the value of a model parameter. Some arrows represent the killing rate constant (Krc) and activation rate constant (Arc). The model includes the cytolytic effect of CD8+ T cells and Natural killer cells that induce the tumor cells to become antigen. M1 macrophages and immature dendritic cells interact with tumor cells and become antigen-presenting cells (APCs). APCs and Neutrophils interact with tumor cells and antigen inducing phagocytosis. APCs also activate naïve CD4+ and naïve CD8+ T cells to become effector CD4+ and CD8+ T cells, respectively. CD4+ T cells help the activation of Naïve B cells in becoming Plasma and Memory B cells. Plasma cells produce antibodies, which bind to tumor cells. Phagocytosis/apoptosis arrows represent the killing rate constant (Krc). The wider the stroke the higher the value of the Krc parameter. Also, some interactions are affected negatively by the binding of PD-1 to anti-PD-L1. Anti-PD-L1and anti-PD-1 reduce the binding of PD1 to PDL1, increasing the intensity of the interaction. In addition, the model incorporates the effects of pro- and anti-inflammatory cytokines and the regulatory effects of M2 macrophages and regulatory T cells (Tregs). Created with BioRender.com

Materials and methods

Mathematical model description

The mathematical model consists of a set of ordinary differential and algebraic equations that are solved in MATLAB. Each model variable represents a model component. The components are: immune cells, tumor cells, cytokines and antibodies, including anti-PD-L1 and anti-PD-1 antibodies (Figure 33). The model considers the effect of pro- and anti-inflammatory cytokines on immune cell functions, the activation of naïve immune cells, and the killing of cancer cells by immune cells. The model also includes cancer cells in three different states: alive cancer cells, dead cancer cells that released free tumor antigen, and cancer cells targeted with antibodies. In addition, we account for the binding of PD1 to PDL1 on the immune cell surface, which reduces their killing or activating potential. Injection of

anti-PD-L1 or anti-PD-1 immunotherapy blocks PD-L1 or PD-1, respectively, on the cells enhancing the killing efficacy and activation efficacy of the adaptive immune system. The killing rate constant (K_{rc}) represents the effectiveness of the tumor cells' killing by the immune cells. As the killing potential of cells of the adaptive immune system is considered more robust compared to that of the innate system, a higher value of K_{rc} is assigned to the cells of the adaptive immune system. The two K_{rc} values are related with a proportionality constant. This is done to account for the more efficient killing of tumor cells by CD8 effector T cells, as shown in Figure 33. The activation rate constant (A_{rc}) represents how easily a naïve cell can be converted into an effector cell. We assumed that the microbiome affects the immune response through these two parameters, K_{rc} and A_{rc}.

The growing tumor was simulated by assuming that all interactions take place inside the tumor region. Furthermore, a uniform spatial distribution was assumed initially for the values of the model variables. The density of the tumor region that includes the immune cells and tumor cells was assumed constant through time and equal to the initial cancer cell density. Based on these assumptions and by calculating the reaction rates of all model components, the rate of change of tumor volume was evaluated. The mass balance for each component of the model was solved and the tumor volume was calculated from the total mass of cells that comprise the tumor.

The values of many model parameters were taken from the literature (

Table 15). To determine the values of the remaining parameters, we employed an optimization procedure to reproduce experimental tumor growth curves from published studies [25,28,31,209] by varying these parameters. The optimization function was the minimization of the sum of the squared difference of the logarithmic values between the measured ($V_{exp.}$) and simulated ($V_{calc.}$) tumor volumes $\left(\min\left(\sum_i\left[\ln\left(V_{exp,i}\right)-\ln\left(V_{calc,i}\right)\right]^2\right)\right)$. Only positive values of model parameters were accepted by the optimization algorithm to have a physical meaning. This was performed by introducing a penalty into the optimization function for negative parameters. The Nelder–Mead simplex algorithm [210,211] was used to find the minimum of the optimization function. The baseline model parameters that depend on tumor cell type and immunotherapy type (anti-PD-L1 and anti-PD-1) are defined with the optimization algorithm by using the average experimental volume from Matson et

al. [28], Gopalakrishnan et al. [25] and Spencer et al. [31] for B16, BP and HCmel1274 melanoma cells. The baseline parameters for each combination of tumor cell/immunotherapy type were kept the same for the reproduction of tumor growth curves for each individual subject with the same tumor cell and immunotherapy type, and only the parameters K_{rc} and A_{rc} were varied to reproduce the other experimental datasets. The aforementioned process assessed the predictive capabilities of the model by varying only two parameters that affect crucial mechanisms of the immune system.

Using the observed tumor volume data, we trained our mathematical model to obtain an optimal estimate of K_{rc} and A_{rc}. We used the forward model parameters estimate to learn the state of the immune system in terms of the concentration of the various types of immune cells and cytokines. Recent advances in immunotherapy have shown that the microbiome mediates through the immune system to affect tumor growth in cancer patients [25,28–33,198]. We have accessed the overall significance of some of the observed confounders, such as experiment type (E1, E2, and E3) and treatment (pre/post-PD-L1), with PERMANOVA. Accordingly, we compute the association between the microbiome and the predicted immune components with Spearman's Rank correlation analysis.

Interactions between the immune system and tumor cells

Figure 34 represents the interactions between the immune components and the tumor cells as well as the interactions of the PD-1 and PD-L1 receptors considered in our mathematical model. Each component of the model corresponds to a variable. These variables are presented in

Table 14 along with their description. These variables are included in ordinary differential equations or algebraic equations. Then, these equations are solved simultaneously by a MATLAB source code.

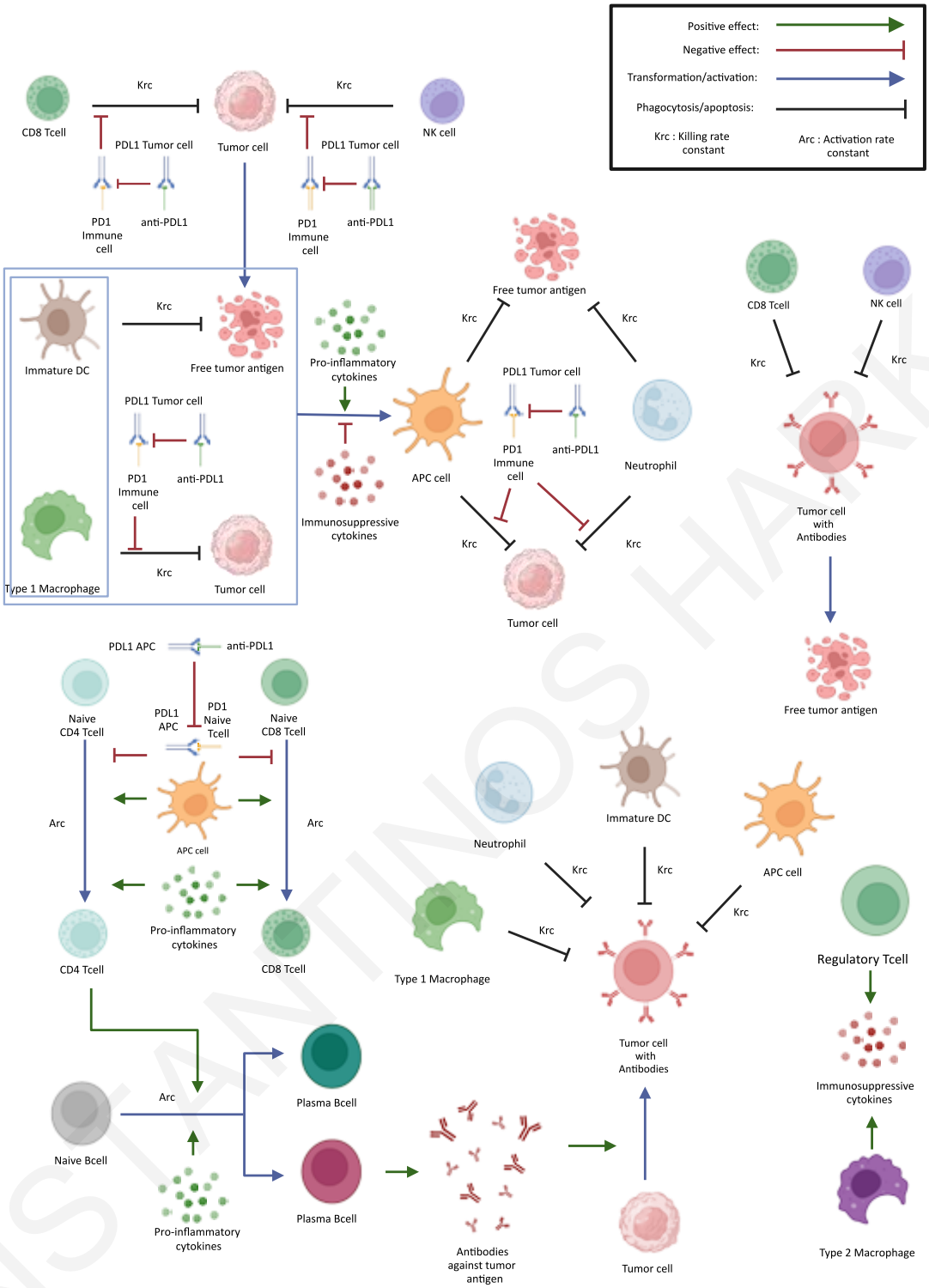

Figure 34: Schematic of mathematical model and its components. The arrows represent the interactions among model components. Some arrows represent the killing rate constant (Krc) and activation rate constant (Arc). The model includes the cytolytic effect of CD8+ T cells and NK cells that induce the tumor cells to make antigen(s). M1 macrophages and dendritic cells interact with tumor cells and become antigen-presenting cells (APCs). APCs and Neutrophils can phagocytose tumor cells and the free tumor

antigen. APCs also activate naïve CD4+ and naïve CD8+ T cells to turn them into effector CD4+ and CD8+ T cells, respectively. CD4+ T cells help the activation of Naïve B cells in becoming Plasma and Memory B cells. Plasma cells produce antibodies, which bind to tumor cells. Phagocytosis/apoptosis arrows represent the killing rate constant (Krc). Also, the killing of cancer cells by immune cells as well as the activation of naive immune are affected negatively by the binding of PD-1 to PD-L1. Anti-PD-L1 and anti-PD-1 reduce the binding of PD-1 to PD-L1, increasing the intensity of these interactions. In addition, the model incorporates the effects of pro-inflammatory and immunosuppressive cytokines and the adverse effects of M2 macrophages and regulatory T cells (Tregs). Created with BioRender.com

Pro-inflammatory cytokines:

Pro-inflammatory cytokines are produced by natural killer cells (NK), effector $CD8^+$ T cells (T^E), antigen-presenting cells (APC), effector $CD4^+$ T cells (Th^E), neutrophils (N), type 1 macrophages (M_1) and plasma cells (P). The rate of change of the concentration of the pro-inflammatory (c) cytokines (e.g., Il2, IFNγ, TNF-α) is described by the following equation:

$$\frac{dc}{dt} = R_c = k_{cNK}NK + k_{cT^E}T^E + k_{cAPC}APC + k_{cTh^E}Th^E + k_{cN}N + k_{cM1}M_1 + k_{cP}P - \delta_c\, c \tag{161}$$

Where the first 7 terms describe the production rates of c by the natural killer (NK), effector $CD8^+$ T (T^E), antigen-presenting cells (APC), effector $CD4^+$ T cells (Th^E), neutrophils (N), macrophages type 1 (M_1) and plasma B cells (P) respectively, and the last term is the degradation rate of c.

Immunosuppressive cytokines

Immunosuppressive cytokines (e.g., IL10, TGF-β) are produced by regulatory T cells (T_{reg}) and type 2 macrophages (M_2). The rate of change of the concentration of the immunosuppressive (α) cytokines (e.g., IL10, TGF-β) is described by the following equation:

$$\frac{d\alpha}{dt} = R_a = k_{ant-T_{reg}}T_{reg} + k_{ant-M2}M_2 - \delta_a a \tag{162}$$

Where the first two terms describe the production of immunosuppressive cytokines by regulatory T cells (T_{reg}), type 2 macrophages (M_2). The last term is the degradation rate of immunosuppressive cytokines.

Interactions between PD-L1, PD-1, anti-PD-1, and anti-PD-L1

PD-1 exists on natural killer cells, effector $CD8^+$ T cells, antigen-presenting cells, effector $CD4^+$ T cells, neutrophils, macrophages type 1 and 2, naïve $CD8^+$ and $CD4^+$ T cells. PD-L1 exists on tumor cells, antigen-presenting cells, macrophages type 1 and 2, dendritic cells, naïve B cells, memory cells and plasma cells. PD-1 on any cell can bind to PD-L1 on other cells or to anti-PD-1 antibody. Similarly, PD-L1 on any cell can bind to PD-1 on other cells or to anti-PD-L1 antibody.

The concentration of the available PD-L1 for binding [212,213] depends on the amount of the available PD-L1 on the cells and is described by the following equation:

$$[\mathrm{PDL1}] = \beta_{\widehat{\mathrm{T}}}\widehat{\mathrm{T}} + \beta_{\mathrm{APC}}\mathrm{APC} + \beta_{\mathrm{DC}}\mathrm{DC} + \beta_{\mathrm{M1}}\mathrm{M}_1 + \beta_{\mathrm{M2}}\mathrm{M}_2 + \beta_{\mathrm{B^N}}\mathrm{B^N} + \beta_{\mathrm{P}}\mathrm{P} - [\mathrm{PD1} - \mathrm{PDL1}] - [\mathrm{PDL1} - \mathrm{antiPDL1}] \quad (163)$$

where the constants β describe the amount of PD-L1 on each type of cell. The first terms describe the amount of PD-L1 on tumor cells, APCs (APC), dendritic cells (DC), macrophages type 1 and 2 (M_1 and M_2), naïve B cells (B^N) and plasma B cells (P). The last two terms describe the amount of PD-L1 which has been already bound to PD-1 and anti-PD-L1 respectively.

The concentration of the available PD-1 for binding [212,213] depends on the amount of the available PD-1 on the cells and is described by the following equation :

$$[\mathrm{PD1}] = \mathrm{a_{T^E}T^E} + \mathrm{a_{Th^E}Th^E} + \mathrm{a_{T_N}T^N} + \mathrm{a_{Th_N}Th^N} + \mathrm{a_N N} + \mathrm{a_{NK}NK} + \mathrm{a_{M_1}M_1} + \mathrm{a_{M_2}M_2} + \mathrm{a_{APC}APC} + \mathrm{a_{DC}DC} + \mathrm{a_{T_{reg}}T_{reg}} - [\mathrm{PD1} - \mathrm{PDL1}] - [\mathrm{PD1} - \mathrm{antiPD1}] \quad (164)$$

where the parameters α represent the amount of PD-1 on each type of cell. The terms except for the last two describe the amount of PD-1 ligand on the following immune cells T^E, Th^E,

T^N, Th^N, N , NK, M_1, M_2, APC, DC and T_{reg}. The last two terms describe the amount of PD-1 which is already bound to PD-L1 and anti-PD-1 respectively.

The rate of change in the concentration of the PD-1 – PD-L1 complex is described by the following equation:

$$\frac{d[PD1 - PDL1]}{dt} = a_{PL}[PD1][PDL1] - d_Q[PD1 - PDL1] \tag{165}$$

where the first term is the binding of PD-1 to the PD-L1 and the last term is their unbinding.

The rate of change in the concentration of the anti-PD-1 - PD-1 complex is:

$$\begin{aligned}\frac{d[PD1 - antiPD1]}{dt} &= \mu_{PD1-aPD1}[PD1][anti - PD1] \\ &\quad - d_{PD1-aPD1}\,[PD1 - antiPD1]\end{aligned} \tag{166}$$

where the first term is the binding of PD-1 to the anti-PD-1 and the last term is their unbinding.

The rate of change in the concentration of the anti-PD-1 is:

$$\begin{aligned}\frac{d[anti - PD1]}{dt} &= \gamma_{anti-PD1} - \mu_{PD1-aPD1}[PD1][anti - PD1] \\ &\quad + d_{PD1-aPD1}\,[PD1 - antiPD1] - d_{anti-PD1}[anti - PD1]\end{aligned} \tag{167}$$

where the first term represents the source term of the anti-PD-1, the second term is the binding of the anti-PD-1 to PD-1, the following term is their unbinding, and the last term is the degradation of anti-PD-1.

The rate of change in the concentration of the anti-PD-L1 - PD-L1 complex is given by the following equation:

$$\frac{d[PDL1 - antiPDL1]}{dt} = \mu_{PDL1-aPDL1}[PDL1][anti - PDL1] - d_{PDL1-aPDL1}\,[PDL1 - antiPDL1] \tag{168}$$

where the first term describes the binding of PD-L1 to the anti-PD-L1 and the last term is their unbinding.

The rate of change in the concentration of the anti-PD-L1 is

$$\frac{d[anti - PDL1]}{dt} = \gamma_{anti-PDL1} - \mu_{PDL1-aPDL1}[PDL1][anti - PDL1] + d_{PDL1-aPDL1}\,[PDL1 - antiPDL1] - d_{anti-PDL1}[anti - PDL1] \tag{169}$$

where the first term represents the source term of the anti-PD-L1, the second term is the binding of the anti-PD-L1 to PD-L1, the following term describes their unbinding, and the last term is the degradation of the anti-PD-L1.

Φ_{x-y} is the fraction of the total PD-1-PD-L1 complex, referring to the binding of PD-1 receptor on x-cell to PD-L1 receptor on y-cell.

$$\Phi_{x-y} = \frac{a_x x}{\sum_x a_x x}\frac{\beta_y y}{\sum_y \beta_y y} \tag{170}$$

Where x can be any of the following cell types:

$$T^E, Th^E, T^N, Th^N, N, NK, M_1, M_2, APC, DC, T_{reg}$$

and y can be any of the following:

$$\hat{T}, APC, DC, M_1, M_2, B^N, P, MB$$

The reduction of PD-1, PD-L1 and PD-1-PD-L1 complex is assumed to be equally distributed among the receptors on the different cell types.

Cancer Cells

The rate of increase in the number of cancer cells ($\hat{T}$) is equal to their rate of proliferation minus their death rate. The death of cancer cells ($\hat{T}$) is induced by $CD8^+$ T cells (T^E) and natural killer cells (Nk). $\hat{T}$ can be phagocytosed by neutrophils (N), type one macrophages (M_1), dendritic cells (DC), and/or antigen presenting cells (APC). The interaction between the tumor cells and either $CD8^+$ T cells (T^E) or natural killer cells (Nk) or type one macrophages (M_1) or neutrophils (N) or dendritic cells (DC), or antigen presenting cells (APC) is inhibited by the binding of PD-1 of the immune cells to PD-L1 of the tumor cells. The antibodies can bind to receptors on the tumor cells and neutralize them.

The rate of change in the concentration of the cancer cells is given by:

$$\begin{aligned}\frac{d\hat{T}}{dt} = R_{\hat{T}} = k_{\hat{T}}\hat{T} - d_A A\hat{T} \\ -\left(Krc_{T^E}\frac{K_T}{K_T + \Phi_{T_T^E-\hat{T}}[PD1-PDL1]}T^E\right. \\ + Krc_{Nk}\frac{K_T}{K_T + \Phi_{Nk-\hat{T}}[PD1-PDL1]}Nk \\ + Krc_{M_1}\frac{K_T}{K_T + \Phi_{M_1-\hat{T}}[PD1-PDL1]}M_1 \\ + Krc_{N}\frac{K_T}{K_T + \Phi_{N-\hat{T}}[PD1-PDL1]}N \\ + Krc_{DC}\frac{K_T}{K_T + \Phi_{DC-\hat{T}}[PD1-PDL1]}DC \\ \left. + Krc_{APC}\frac{K_T}{K_T + \Phi_{DC_T^*-\hat{T}}[PD1-PDL1]}APC\right)\hat{T}\end{aligned} \quad (171)$$

Where the first term is the proliferation rate of the tumor cells. The second term describes the neutralization of tumor cells by the binding of antibodies. The remaining terms are the death rates which depend on the tumor cell density and the immune cells (effector $CD8^+$, natural killer, type 1 macrophage, neutrophils, dendritic cells and antigen presenting cells) [214].

Dead Cancer Cells or free tumor antigen

The dead cancer cells or free tumor antigen ($\hat{T}_D$) are produced when an immune cell induces cytolysis of a tumor cell. $\hat{T}_D$ is phagocytosed by N, M_1, DC or APC. The phagocytosis of dead cancer cells does not depend on PD-1-PD-L1 binding.

The rate of change in the concentration of the dead tumor cells or free tumor antigen is:

$$\begin{aligned}\frac{d\hat{T}_D}{dt} = R_{\hat{T}_D} = {} & d_{Tc}\hat{T} \\ & + \hat{T}\left(Krc_{T^E}\frac{K_T}{K_T + \Phi_{T^E-\hat{T}}\,[PD1-PDL1]}T^E\right. \\ & \left. + Krc_{Nk}\frac{K_T}{K_T + \Phi_{Nk-\hat{T}}\,[PD1-PDL1]}Nk\right) \\ & + (Krc_{T^E}T^E + Krc_{Nk}Nk)\hat{T}_A \\ & - \left(Krc_{M_1}M_1 + Krc_N N + Krc_{DC}DC + Krc_{APC}APC\right)\hat{T}_D\end{aligned} \tag{172}$$

The first term is the rate of apoptosis of tumor cells which increases the number of $\hat{T}_D$. The following six terms describe the increase in $\hat{T}_D$ when $T^E$and Nk induce cytolysis of$\hat{T}$ or tumor cell with antibody ($\hat{T}_A$). The remaining terms represent the phagocytosis of $\hat{T}_D$ by N, M_1, DC or APC

Cancer Cells with Antibody

The cancer cells with antibodies $\hat{T}_A$ bound to their membrane are produced when an antibody binds to a cancer cell. Cancer cells with antibodies are easily recognized and killed by the immune cells. $\hat{T}_A$ can be consumed by the following immune cells T^E, Nk, M_1, N DC or APC.

The rate of change in the concentration of cancer cells with antibodies bound to their membrane is:

$$\begin{aligned}\frac{d\hat{T}_A}{dt} = R_{\hat{T}_A} = {} & d_A A\hat{T} \\ & - \left(Krc_{T^E}T^E + Krc_{Nk}Nk + Krc_{M_1}M_1 + Krc_N N + Krc_{DC}DC\right. \\ & \left. + Krc_{APC}APC\right)\hat{T}_A\end{aligned} \tag{173}$$

where the first term is the production of $\hat{T}_A$ by the binding of antibodies on tumor cells. The remaining terms are the elimination of $\hat{T}_A$ by the following immune cells T^E, Nk, M_1, N DC or APC.

Neutrophils

The recruitment of neutrophils depends on the pro-inflammatory cytokines.

The rate of change in the concentration of the neutrophils is:

$$\frac{dN}{dt} = R_N = \frac{\lambda_N c}{K_N + c} - \delta_N N \qquad (174)$$

where the first term describes the recruitment of the neutrophils and its dependence on pro-inflammatory cytokines and the last term describes their death rate.

Macrophage, dendritic, and antigen presenting cells

Macrophages recruitment depends on concentration of pro- and anti- inflammatory cytokines. The concentration of pro-inflammatory cytokines relative to the total cytokines increases the concentration of type 1 macrophages. The concentration of immunosuppressive cytokines relative to the total cytokines increases the concentration of type 2 macrophages. Type 1 macrophages can also become antigen presenting cells in the same manner as dendritic cells. APCs production depends on the killing of tumor cells, dead tumor cells (or free tumor antigen) and tumor cells with antibody, killed by dendritic cells or type 1 macrophages. Their activation depends on pro-inflammatory and immunosuppressive cytokines.

Macrophages

The rate of change in the concentration of type 1 and type 2 macrophages is given by:

$$\frac{dM1}{dt} = R_{M1} = \lambda_{M1}\frac{c}{\alpha + c} - \frac{\chi_{M1}\, c}{K_{APC} + \alpha}\frac{K_{aAPC}}{K_{aAPC} + \alpha}\; M_1\left[Krc_{M_1}\left(\frac{K_T\hat{T}}{K_T + \Phi_{M_1-\hat{T}}\,[PD1 - PDL1]} + \hat{T}_D + \hat{T}_A\right)\right] - \delta_{M1}M1 \quad (175)$$

$$\frac{dM2}{dt} = R_{M2} = \lambda_{M2}\frac{\alpha}{c + \alpha} - \delta_{M2}M2 \quad (176)$$

where type 1 macrophages production depends on the ratio of pro-inflammatory to total cytokines. The second term describes their transformation to antigen-presenting cells by phagocytosis of $\hat{T}$, $\hat{T}_D$, or $\hat{T}_A$. Type 2 macrophages production depends on the ratio of immunosuppressive to total cytokines. Both equations include a death rate term [212,215].

Dendritic cells (DC)

The rate of change in the concentration of the dendritic cells is:

$$\frac{dDC}{dt} = R_{DC} = S_{DC} - \delta_{DC}DC - \chi_{DC}\frac{c}{K_{cAPC} + c}\frac{K_{aAPC}}{K_{aAPC} + \alpha}\; DC\left[Krc_{DC}\left(\frac{K_T\hat{T}}{K_T + \Phi_{DC-\hat{T}}\,[PD1 - PDL1]} + \hat{T}_D + \hat{T}_A\right)\right] \quad (177)$$

where the first term describes the source term of DCs, and the next term is the death rate of DCs. The next term describes the conversion of dendritic cells to antigen-presenting cells which depends on the tumor cells ($\hat{T}$), dead tumor cells ($\hat{T}_D$) and tumor cells bearing antibodies on their membrane ($\hat{T}_A$).

Antigen-presenting cells APCs (APC)

The rate of change in the concentration of the APCs is:

$$\frac{dAPC}{dt} = R_{DC^*}$$
$$= \frac{c}{K_{cAPC} + c} \frac{K_{aAPC}}{K_{aAPC} + \alpha} \left[\chi_{DC} Krc_{DC} DC \left(\frac{K_T \hat{T}}{K_T + \Phi_{DC-\hat{T}} [PD1 - PDL1]} + \hat{T}_D + \hat{T}_A \right) + \chi_{M1} Krc_{M_1} M_1 \left(\frac{K_T \hat{T}}{K_T + \Phi_{M_1-\hat{T}} [PD1 - PDL1]} + \hat{T}_D + \hat{T}_A \right) \right] \quad (178)$$
$$- \delta_{APC} APC$$

where the first term describes the conversion rates of dendritic cells and type 1 macrophages to APCs (APC) and the next term describes the death rate of APCs.

CD4⁺ T cells

Naïve $CD4^+$ T cells can become effector $CD4^+$ T cells. Activation of effector $CD4^+$ T cells depends on pro-inflammatory cytokines and the PD-1-PD-L1 complex especially on the binding of naïve CD+4 T cell PD-1 to the APC PD-L1.

Naïve CD4⁺ T cells (Th^N)

The rate of change in the concentration of the Naive $CD4^+$ T cells (Th^N) is:

$$\frac{dTh^N}{dt} = R_{Th^N} = S_{Th^N} - Th^N \left(\frac{c}{K_{Th} + c} \right) \left(Arc_{Th} \frac{K_T}{K_T + \Phi_{T^N-DC^*} [PD1 - PDL1]} APC \right) - \delta_{Th^N} Th^N \quad (179)$$

where the first term describes the source term of Naïve $CD4^+$ T cells, and the second term describes the activation rate of naive $CD4^+$ T cells by APCs (APC). The last term describes the death rate of naïve $CD4^+$ T cells.

Effector CD4⁺ T cells (Th^E)

The rate of change in the concentration of the effector $CD4^+$ T cells is:

$$\frac{dTh^E}{dt} = R_{Th^E} = Arc_{Th} Th^N \left(\frac{c}{K_{Th} + c}\right)\left(\frac{K_T}{K_T + \Phi_{Th^N - DC^*}[PD1 - PDL1]} APC\right) - \delta_{Th^E} Th^E \quad (180)$$

where the first term describes the activation of naïve $CD4^+$ T cells by APC and the second term describes their death.

Regulatory T cells (Treg)

Regulatory T cells can be supplied from thymus and regulate the immune system by producing immunosuppressive cytokines.

The rate of change in the concentration of the regulatory T cells is:

$$\frac{dT_{reg}}{dt} = R_{T_{reg}} = S_{Treg} - \delta_{Treg} T_{reg} \quad (181)$$

where the first term describes their production rate from the thymus. The last term describes their death rate [216].

$CD8^+$ T cells

Naïve $CD8^+$ T cells can become effector $CD8^+$ T cells. Activation of effector $CD8^+$ T cells in general depends on cytokines and the PD-1-PD-L1 complex.

Naïve $CD8^+$ T cells (T^N)

The rate of change in the concentration of the naïve $CD8^+$ T cells is:

$$\frac{dT^N}{dt} = R_{T^N} = S_{T^N} - T^N \left(\frac{c}{K_{T^N} + c}\right)\left(Arc_{T^N} \frac{K_T}{K_T + \Phi_{T^N - DC_T^*}[PD1 - PDL1]} APC\right) - \delta_{T^N} T^N \quad (182)$$

where the first term represents the source term of Naïve $CD8^+$ T cells, and the second term describes the activation rate of naïve $CD8^+$ T cells by APC. The last term describes the death rate of naïve $CD8^+$ T cells.

Effector CD8⁺ T cells (T^E)

The rate of change in the concentration of the effector $CD8^+$ T cells (T^E) is:

$$\frac{dT^E}{dt} = R_{T^E} = Arc_{T^N} T^N \left(\frac{c}{K_{T^N} + c}\right)\left(\frac{K_T}{K_T + \Phi_{T^N - DC_T^*}[PD1 - PDL1]} APC\right) - \delta_{T^E} T^E \quad (183)$$

where the first term describes the activation rate of the naïve $CD8^+$ T cells by APC and the second term describes their death.

Natural killer cells

The production of natural killer cells depends on the ratio of pro- to immunosuppressive cytokines.

The rate of change in the concentration of the natural killer cells is:

$$\frac{dNK}{dt} = R_{NK} = \frac{\lambda_{NK}\, c}{K_{NK} + c} - \delta_{NK} NK \quad (184)$$

The first term is the production of natural killer cells depending on the pro-inflammatory cytokines. The second term is their death rate.

B cells

Naïve B cells can become Plasma cells and Memory cells. Pro-inflammatory cytokines and effector $CD4^+$ T cells help the Naïve B cells to become memory B cells and plasma cells.

Naıve B cells (B^N)

$$\frac{dB^N}{dt} = R_{B^N} = S_B - [(Arc_{B^N M} + Arc_{B^N P}) Th^E] B^N \left(\frac{c}{K_B + c}\right) - \delta_B B^N \quad (185)$$

where the first term describes the source of naïve B cells. The second term describes the conversion of naïve B cells to plasma and memory cells and the last term describes the death of naïve B cells.

Memory B cells (B)

$$\frac{dMB}{dt} = R_{MB} = Arc_{B^N M} B^N Th^E \left(\frac{c}{K_B + c}\right) - \delta_{MB} MB \tag{186}$$

where the first term describes the production rate of memory B cells from naïve B cells which depends on effector $CD4^+$ cells and pro-inflammatory cytokines. The second term describes the death of memory B cells.

Plasma cells

$$\frac{dP}{dt} = R_P = Arc_{B^N P} B^N Th^E \left(\frac{c}{K_B + c}\right) - \delta_P P \tag{187}$$

where the first term describes the production of plasma cells from naïve B cells which depends on effector $CD4^+$ and pro-inflammatory cytokines. The second term describes the death of plasma cells.

Antibodies

Antibodies are produced by plasma cells and can bind to tumor cells.

$$\frac{dA}{dt} = R_A = k_A P - d_A A \hat{T} \tag{188}$$

where the first term describes the production of antibodies by plasma cells. The last term describes the binding of antibodies to tumor cells.

Calculation of the tumor volume

To calculate the tumor volume, the initial density (or concentration) of the tumor (including the cancer cells and immune cells) was assumed equal to the initial cancer cell density $\hat{T}_0$, because the initial concentrations of the immune cells was negligible. The density of the tumor (whole system) was assumed to remain constant through time (equal to $\hat{T}_0$). These assumptions allow to calculate the rate of change of the volume with the total rate of change of the mass:

$$\frac{dV}{dt} = \frac{1}{\hat{T}_0} V \sum_i R_i \tag{189}$$

Where R_i is the rate of change in concentration (reaction rates) of i^{th} cell. The reaction rates of the following cells were considered:

$$T^E, Th^E, T^N, Th^N, N, NK, M_1, M_2, APC, DC, T_{reg}, \hat{T}, B^N, P, MB, \hat{T}_A$$

The volume of the tumor is calculated at the same time with the mass balances of all components.

Calculation of the mass balance of each component

The rates of change of concentrations are functions of the concentrations (equations 1,2, 5-9 and 11-28). They have the following form, and they are calculated first.

$$\frac{dq}{dt} = R_q \tag{190}$$

Where $q = (c, \alpha, T^E, Th^E, T^N, Th^N, N, NK, M_1, M_2, APC, DC, T_{reg}, \hat{T}, B^N, P,$

$$MB, \hat{T}_D, \hat{T}_A, A, [PD1 - PDL1], [PD1 - antiPD1],$$

$$[anti - PD1], [PDL1 - antiPDL1], [anti - PDL1])$$

Then they are introduced in the mass balance of each component as follows:

$$\frac{d(m_q)}{dt} = \frac{d(Vq)}{dt} = VR_q \tag{191}$$

Where m_q, q and R_q are the mass, concentration, and rate of change in concentration (reaction rate) of the q component respectively and V is the current volume.

The concentrations are calculated by dividing each mass with the total volume

$$q = \frac{m_q}{V} \tag{192}$$

Description of murine and human studies used for calibration of the model

Murine studies

The experimental design for these studies has been previously described in full detail [31]. The studies were conducted at the MD Anderson Cancer Center under the approval of the Institutional Animal Care and Use Committee (IACUC). B6 germ-free mice were colonized by a complete responder microbiota through FMT. One week was allowed for engraftment, following which, mice received subcutaneous injection of BP melanoma cells. Once tumors reached a size range of 250-500 mm^3, mice were treated with 3 doses of intraperitoneal anti-PD-L1 and tumor size was measured using a caliper.

Human studies

For further calibration of our model, we incorporated data from a phase 1 clinical trial conducted by Baruch et al. [30] that evaluated the safety of FMT in patients with PD-1-refractory melanoma. Ten patients were enrolled in this study and received a broad-spectrum antibiotic treatment to deplete the native microbiota, followed by FMT with stool samples from complete responders (2 donors). FMT was conducted via colonoscopy and continued via oral capsules at day 1 and day 12 post-colonoscopy. Subsequently, patients received anti-PD-1 treatment with additional FMT (oral capsules) administered every 14 days. Response to tumor treatment was measured using the iRECIST criteria.

Statistical analysis

We used statistical methods to study the connection between the microbiome and the immune system in experiments 3 4 and 5 [31]. These experiments involved changing the microbiome only through FMT. We used a beta-diversity analysis to compare diversity between samples and represented each sample using the top three principal components of principal coordinate analysis. We also analyzed the significance of observed confounders and ICB treatment on microbiome using PERMANOVA analyses. This helped us identify confounders that had a significant impact on the diversity of the microbiome. After controlling these confounders, we measured the association using Spearman's Rank correlation. We used the R statistical software and MATLAB for all analyses and visual representations.

Results

Gut microbiome affects the activation and killing potential of immune cells

We set out to define potential mechanisms by which the gut microbiome affects anti-tumor immune responses. To do so, we first established the values of the model parameters that are involved in the growth of the tumor and the efficacy of immunotherapy (Table 16) by fitting the model to experimental data from B16, BP, and HCmel1274 murine melanoma tumors using an optimization procedure [25,28,31]. In the B16 and BP melanoma studies, the gut microbiome was modulated in the case of specific pathogen-free mice or seeded in the case of germ-free mice with a FMT from a responder or a non-responder patient. Subsequently, the mice were treated with anti-PDL1 antibodies (Figure 35a). The experimental data and model predictions are shown in Figure 35b-c and Figure 36. For each experiment, we generated a set of values for the model parameters. Among groups of each experiment only the parameter related to the immune cell activation (A_{rc}) and the parameter related to the efficiency of cancer cell killing (K_{rc}) were varied. Those two parameters describe the hypothesized roles of the microbiome.

(A)

Experiment	Cell line	Treatment	Microbiome modulation
Matson et al. [28]	B16	Anti-PD-L1 (day 4)	FMT
Gopalakrishnan et al. [25]	BP	Anti-PD-L1 (day 14)	FMT

(B)

Matson et al. [28]

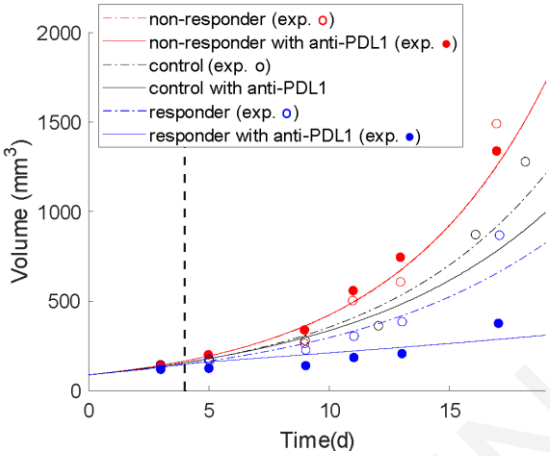

(C)

Gopalakrishnan et al. [25]

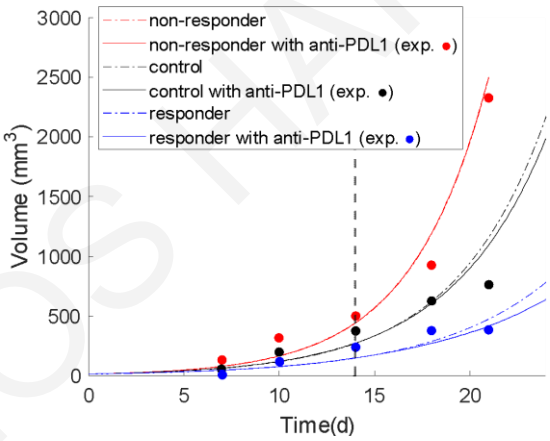

Figure 35: Comparison of experimental tumor growth curves with model prediction to define baseline values of model parameters. (a) Experimental details for each experiment. (b) and (c) Bullet points represent the experimental data and the continuous curves represent the model predictions. Day 0 is the initiation of the simulation, (b) day 3, (c) day 7 of the experiment. The vertical dashed black line represents the initiation of immunotherapy (anti-PD-L1). (b) experimental data from Matson et al. [28] (B16 melanoma cells) and (c) Gopalakrishnan et al. [25] (BP melanoma cells. In (b) and (c), the control groups are germ-free mice and the rest of the groups received FMT from either a responder or a non-responder patient to immunotherapy.

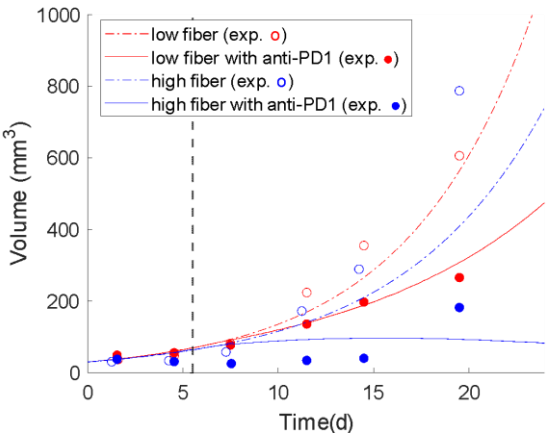

Figure 36: Comparison of experimental tumor growth curves with model prediction to define baseline values of model parameters. The bullet points represent the experimental data, and the continuous curves represent the model predictions. Day 0 is the initiation of the simulation and day 1.5 of the experiment. The vertical dashed black line represents the initiation of immunotherapy (anti-PD1). The experimental data are from Spencer et al. (HCmel1274 melanoma cells) [31]. The mice were kept in specific pathogen-free conditions and fed with low- or high-fiber diet.

Next, we employed data from a clinical study of patients with melanoma who progressed on ICB and were subsequently treated with FMT followed by ICB in an attempt to overcome initial ICB resistance (Baruch et al.[30]). Here, we assigned the same baseline parameter values obtained from the HCmel1274 murine melanoma study (Spencer et al. [31] Figure 36) because these studies used the same anti-PD1 treatment; we then simulated treatment of the human melanoma tumors (Figure 37a-c). To reproduce these data, we only varied the parameters related to the immune cell activation (A_{rc}) and efficiency of cancer cell killing (K_{rc}) which we assumed are affected by microbiome (as shown in Figure 37a). The model was able to reproduce the clinical tumor growth data with good accuracy (Pearson's rho, r=0.7 with a p-value 0.0001) as well as validated with data for CD8+ T cells (Figure 38).

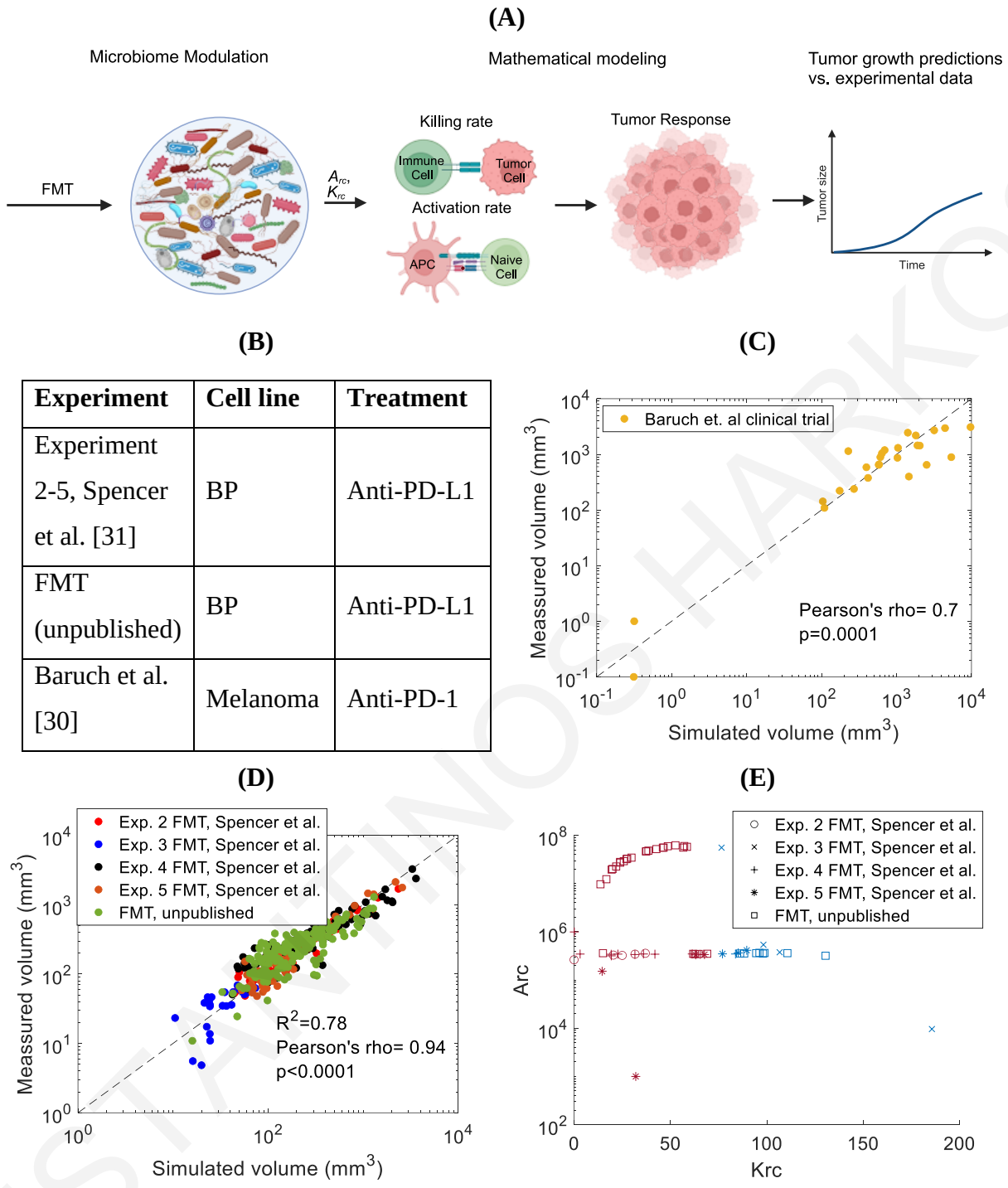

Experiment	Cell line	Treatment
Experiment 2-5, Spencer et al. [31]	BP	Anti-PD-L1
FMT (unpublished)	BP	Anti-PD-L1
Baruch et al. [30]	Melanoma	Anti-PD-1

Figure 37: Model calibration with preclinical and clinical data. Microbiome modulation was assumed to affect only the parameters Krc and Arc. Comparison of model predictions with measured. (a) Schematic of followed procedure (Created with BioRender.com) (b) Experimental details for each experiment (c) clinical data that include 9 patients (Baruch et al. [30]) and (d) preclinical tumor volume data that include 62 mice which received only FMT modulation of microbiome (Spencer et al. [31] and an unpublished FMT data set). (e) Range of Krc and Arc parameters employed for the results in figure 3D, blue and red points correspond to responders and non-responders, respectively.

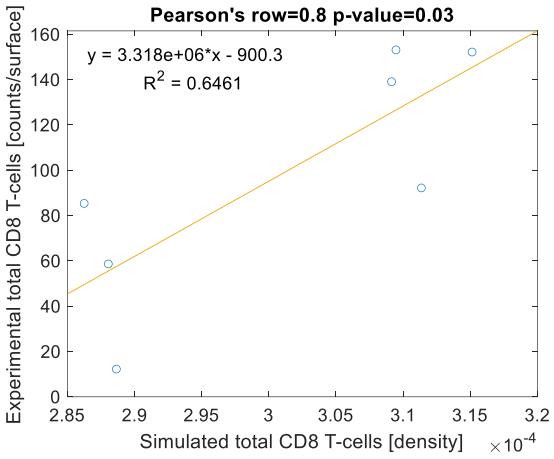

Figure 38: Comparison of simulated CD8 T with available experimental data from the human clinical trial after treatment[34]

After defining baseline values of the model parameters, we then used the model to probe new sets of pertinent experimental data for which complete sets of microbiome profiles were available. To reproduce these data, we only varied the parameters A_{rc} and K_{rc}. Specifically, we used data from 62 mice (Figure 37d) where: i) 35 received FMT from a responder, a non-responder melanoma patient, or a healthy person (FMT, unpublished data) and ii) 27 received FMT from a responder patient (experiments 2-5 from Spencer et al. [31]). For experiments 2-5 and FMT, the baseline parameters were kept the same as for Gopalakrishnan et al. [25] (Figure 35c and Table 16) because both of these experiments involved the same cell line (BP melanoma) and the same treatment (anti-PD-L1).

This process resulted in fits for the killing rate constant (parameter K_{rc}) and the activation of the adaptive immune system (parameter A_{rc}) for each mouse. Figure 37d presents the comparison of the experimental and the predicted tumor volume by the model at all available time points. The diagonal dashed line depicts the best-fitting case scenario. Points close to the diagonal line have the best agreement between the simulated and experimental values. By only varying K_{rc} and A_{rc} and keeping the rest of the parameters at their baseline values, the model was able to reproduce the measured tumor volume for all 62 mice with good accuracy (R^2=0.78; Pearson's rho, r=0.94 with a p-value less than 0.0001). This supports our hypothesis that the primary effects of the microbiome are through modulation of the killing

of tumor cells by immune cells and the activation of the adaptive immune system. Figure 37e shows the range of values of K_{rc} and A_{rc} that correspond to responders and non-responders (blue and red points respectively). A tumor was assumed to be a responder if its simulated volume decreased below a threshold value (10 mm^3) and never surpassed a size of 1500 mm^3 until day 100.

Modeling framework suggests antitumor immune responses

The advantage of mathematical modeling is the ability to estimate mechanistic parameters that are difficult to determine experimentally. From the analysis in Figure 37d, our model predicted the immune profile of the 62 cases for which the microbiome profile was available. Predictions of model variables for the antitumor immune response are shown in Figure 39. The figure presents the time evolution of model variables, and the plots are divided into two categories representing the tumor response – responders and non-responders. A tumor was assumed to be a responder if its simulated volume decreased below a threshold value (10 mm^3) and never surpassed a size of 1500 mm^3 until day 100. The non-responder concentrations (red curves) of pro-inflammatory cytokines, natural killer cells, and antigen-presenting cells have lower values than the corresponding concentrations for the responders (blue curves), and they reach a plateau. The activation of the adaptive immune system is also insignificant in the non-responders and thus, the non-responder concentrations of the effector CD8+ and CD4+ T cells, memory, and plasma B cells are near zero, which results in a low amount of tumor antigen and tumor cells with antibodies. On the other hand, the responders' concentrations of the pro-inflammatory cytokines, natural killer cells, and antigen-presenting cells are continuously increasing. There is also a significant activation of the adaptive immune system in responders, which results in high concentrations of effector CD8+ and CD4+ T cells, memory, and plasma B cells. Overall, the simulations predict that the responder mice have strong innate and adaptive immune responses, which results in decreased tumor cell density and tumor eradication.

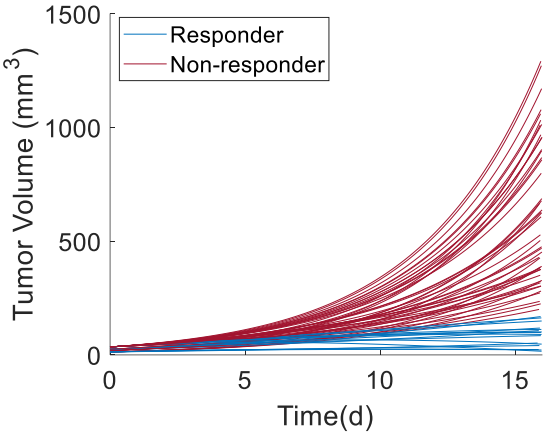

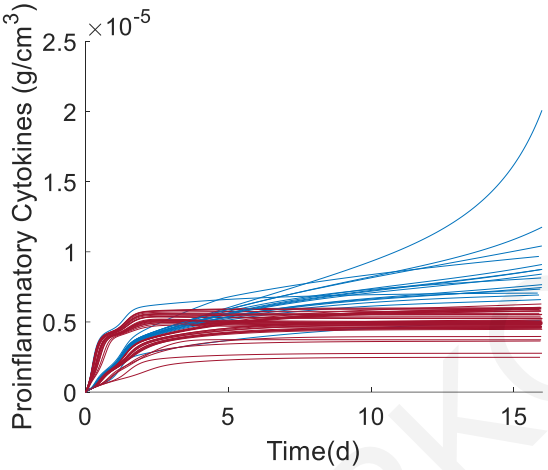

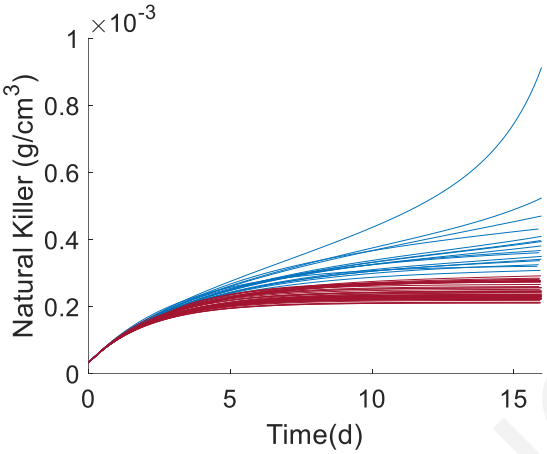

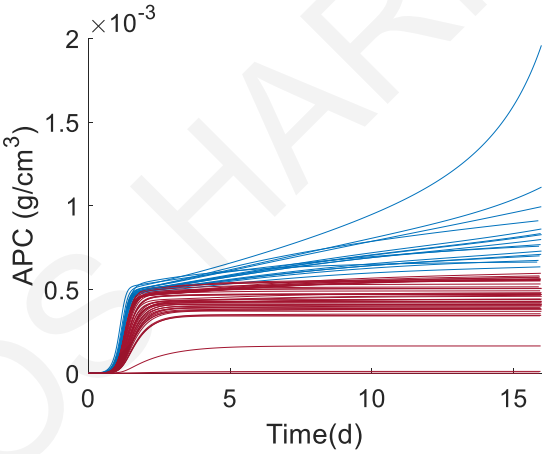

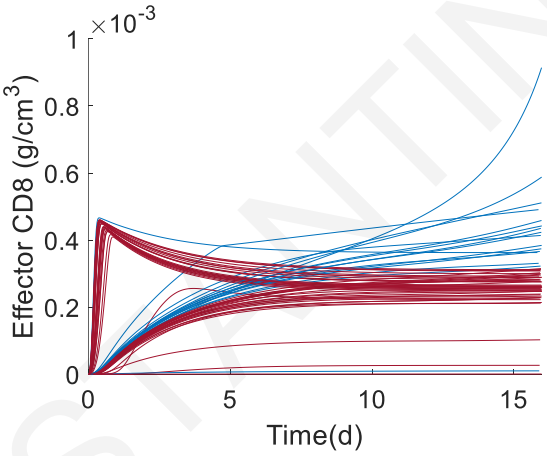

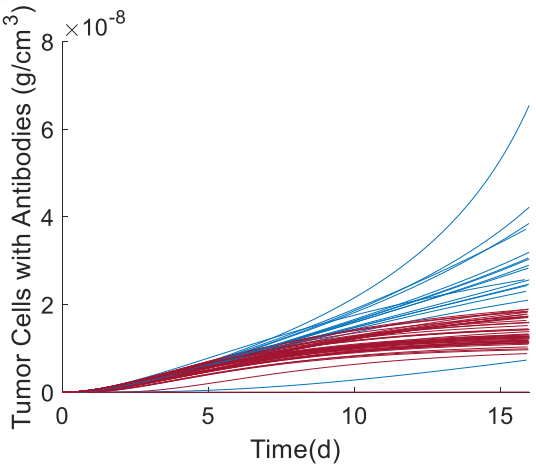

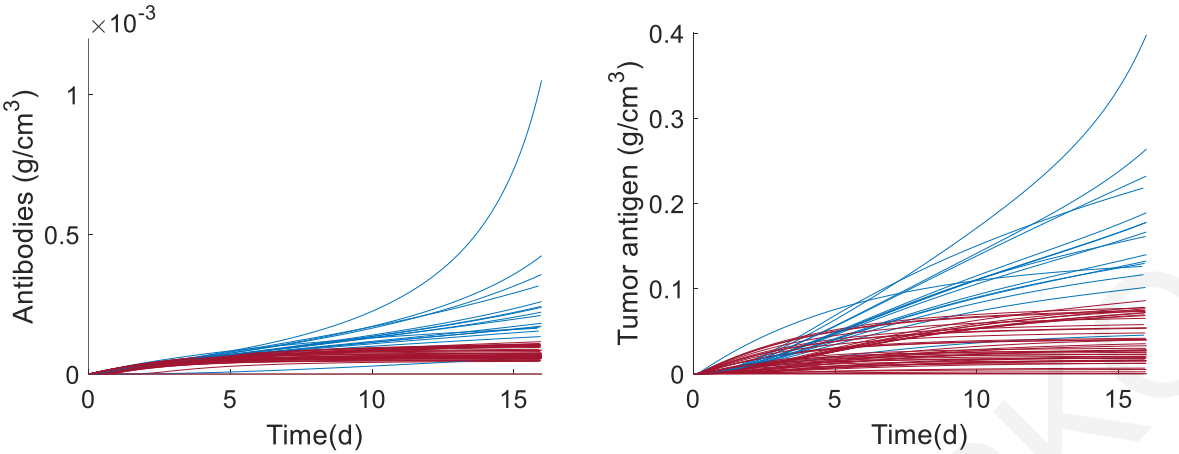

Figure 39: The time evolution of indicative model variables. The blue curves represent the variables for the responder group and the red curves for the non-responders respectively.

Association analysis suggests correlations of specific gut bacteria with immune cell responses

Next, we examined the relationships between specific microbes and components of the immune system. To this end, we performed a robust association analysis between the model predictions of the immune system with the microbiome profiling (Figure 40a and Figure 40b) from the murine studies (experiment 3 4 and 5 in Figure 37) [31] of mice that received microbiome modulation only with FMT. To identify associations of the microbiome families with components of the immune system, we evaluated the association of microbiome profiles reported in the experimental studies with the immune profiles generated by our model. For the association analysis (Figure 40c), the microbiome profiling data (Figure 40a) were not separated to pre- and post-ICB treatment because the underlying microbiome profiles are not significantly different as seen in Figure 40b for the p-value of pre-/post-treatment. The three different experiments involve studies with three different FMT responder donors. The different FMT donors induce different microbiomes, as evidenced by the microbiome profiles in Figure 40a and Figure 40b (p-value of the experiment 3,4, and 5 is 0). The association analysis is presented in Figure 40c and summarized in Table 8. We have suitably adjusted for the three experiments by only considering the microbiome families that have non-zero relative abundance for their associations. In this way, we have the largest possible data set that allowed us to extract the strongest signal from all experiments.

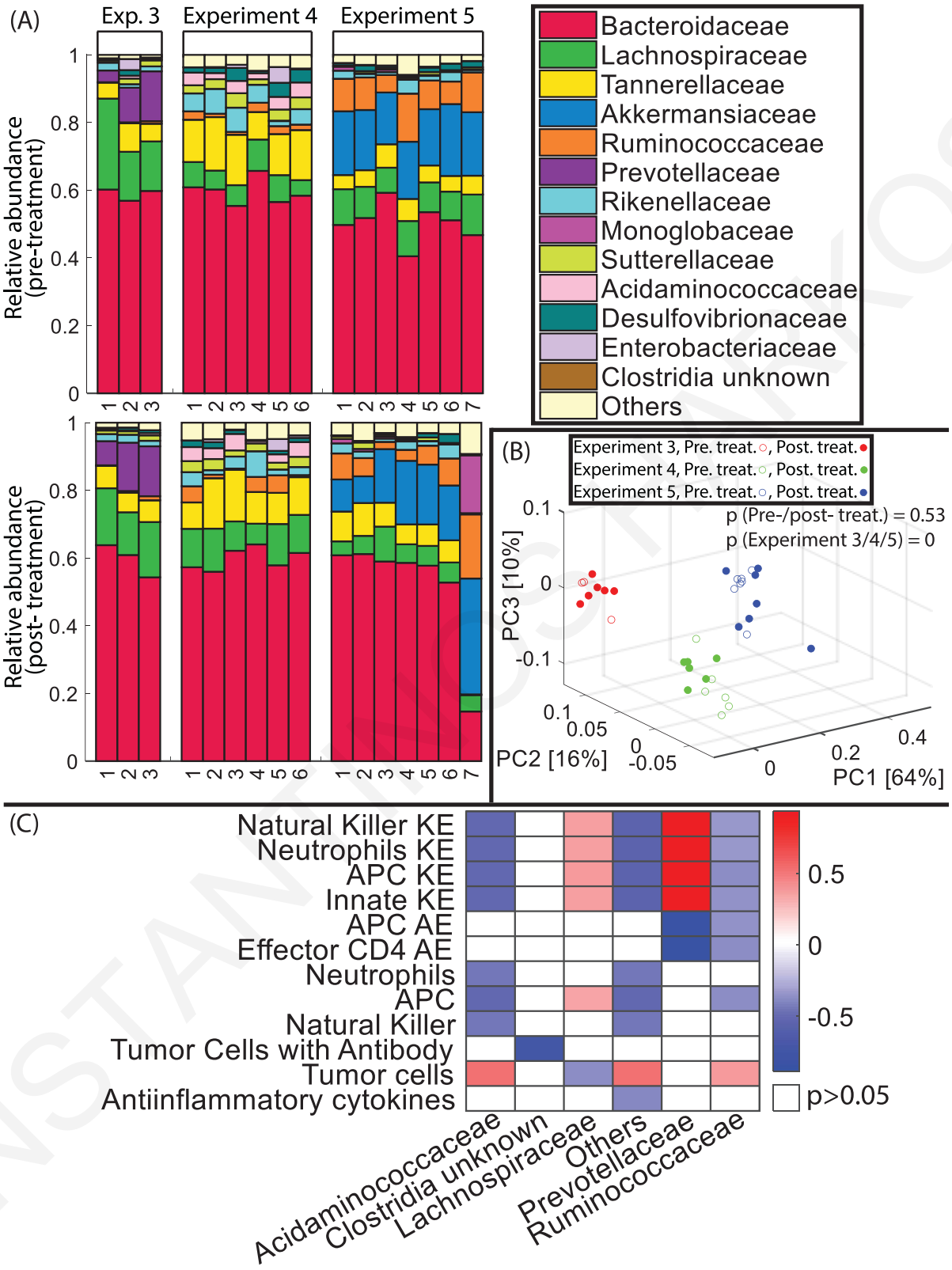

Figure 40: Microbial abundance profiles obtained by 16Sv4 RNA gene profiling of murine fecal samples. (a) Fecal microbiome profiles are represented by compositional plots showing the relative abundance of

the bacteria at the family level. the three experimental groups (E1, E2, and E3) received only FMT microbiome modulation and treated with a-PD-L1 (b) Principal components analysis of the microbiome data and the p-value of PERMANOVA for pre or post treatment groups and the experimental groups. (c) The association between microbiome at the family level and immune profile by adjusting for the three experiments (only values with p<0.05 are presented)

Table 8: Summary of the association of microbiome at the family level with immune profile for Figure 40c. Table shows the association between microbiome and adaptive-innate immunity before and after treatment.

	Post-treatment	
	Adaptive	**Innate**
Acidaminococcaceae	↓	-
Clostridia unknown	↓	-
Lachnospiraceae	-	↑
Others	-	↓
Prevotellaceae	↓	↑
Ruminococcaceae	↓	↓

Positive association	↑	**Negative association**	↓	**No indication**	–

Our model identified certain bacterial taxa that have been the subject of previous studies, such as Lachnospiraceae, Prevotellaceae and Ruminococcaceae [217–220]. The analysis Figure 40c suggests that there are direct associations between the immune cell killing and activation efficiencies (K_{rc} and A_{rc} respectively in Figure 40c) and the bacterial taxa. These associations are consistent with our initial hypothesis that the microbiome affects the immune system primarily by enhancing immune cell activation and killing efficiency. The results also show that Lachnospiraceae is correlated positively with the killing effectiveness of the innate immune cells (natural killer, neutrophils and APCs) and negatively with the number of tumor cells. On the other hand, the Acidaminococcaceae and "Other" families (families that had a very small relative abundance) are correlated negatively with the killing

effectiveness of the innate immune cells and positively with tumor cells. The Ruminococcaceae family is correlated negatively with the killing effectiveness of the innate immune cells and activation effectiveness of the adaptive immune cells, which results in a positive correlation with tumor cells. Interestingly, the Prevotellaceae family seems to have a dual role: it is correlated positively with the killing effectiveness of the innate immune cells and negatively with the activation effectiveness of the adaptive immune cells.

Discussion

In this chapter, we developed a systems approach to elucidate the role of the microbiome in controlling immune responses and determining the efficacy of immunotherapy. Our approach is based on (a) microbiome profiles obtained from preclinical and clinical studies, (b) a mechanistic mathematical model specifically developed for the simulation of the immune profile during anti-tumor response and (c) an advanced statistical analysis to correlate the experimental data with the model predictions. Through comparison of model predictions with experimental observation of tumor response, we identified the immune activation rate, A_{rc}, and the killing rate, K_{rc}, as key determinants of microbiome-mediated anti-tumor immunity. Provocatively, using our mathematical model, we were able to distill the complexity of each experiment and microbiome modulation with just two model parameters: the killing rate constant (K_{rc}) and the activation rate constant (A_{rc}) (Figure 37). Furthermore, by evaluating the association of different bacterial taxa with the immune profiles predicted by our model, we identified patterns of association that provide additional information about the involvement of the microbiome in the response and resistance to ICB. These results can inform future pre-clinical and clinical studies. Interestingly, the microbiome association analysis indicates direct connections between the microbiome and killing and activation efficiency of the adaptive immune cells. Our results can also help guide experimental investigations of these two crucial mechanisms and how they are affected by specific microbiome families. Of note, our model and methodology can be used as a tool to test and refine new mechanisms as soon as new experiments become available.

Regarding the association analysis of the microbiome families and the immune components, the Lachnospiraceae family is correlated positively with increased immune responses, which is in agreement with the literature [217,218]. The Ruminococcaceae family seems to induce immunosuppression according to our results which is consistent with literature reports that

this family has anti-inflammation effects on the colon and causes less adverse effects during immunotherapy [219–221]. In patients with melanoma, the Ruminococcaceae family was mostly found in responders to immunotherapy [25]. This discrepancy indicates that the microbiome has a collective effect on the response to immunotherapy and a balance between immunostimulation to cause anti-tumor effects and immunosuppression to limit adverse effects is needed to induce response to immunotherapy.

It should be noted that the analyses based on our model do not imply causal relationships between bacteria and the tumor immune profile. Nevertheless, the identified associations with immune components could help determine the focus and design of future mechanistic biological studies. In addition, as with any mathematical model, our modeling framework is subject to certain assumptions and limitations. The most obvious limitations are that we focused on the gut microbiome and did not consider the local tumor microenvironment. Also, we assumed that the contribution of the microbiome to the activation and killing rates are the same for all cells of the innate and adaptive immune systems. Furthermore we did not consider in the deterministic model the role of PD-L2 ligand [222]. Due to the complexity of the immune system, it would be intractable for all individual components to be incorporated into a model with parameters that can be estimated independently. These limitations not withstanding, our systems approach combining state-of-the-art murine and human studies with advanced mathematical modeling and statistical analysis paves the way for the elucidation of the role of microbiome modulation in improving cancer immunotherapy.

Chapter 6: Conclusions

Mathematical modelling in cancer can be proven a valuable tool for the investigation of various events during tumor progression and treatment. It can shed light on various mechanisms taking place as well as improving the design of therapeutic agents for various treatments. The thesis uses a mathematical framework of tumor growth as a basis. Incorporating variations of this model allows the examination of different applications and treatment strategies.

The analysis showed that non-invasive imaging techniques like MRI, DTI MRI and MRE can be valuable in capturing various properties of the patient's tumor state and integrate them in an in silico model. More specifically integration of biomechanical properties from MRE allows predictions for anisotropic tumor growth, anisotropic compression of vascular density that results in vessel's heterogenic distribution which affects the delivery of therapeutics.

Integration of various cells of the immune system allows the examination of the effect of immunotherapies. When modelling immunotherapy, the consideration of properties of the tumor microenvironment as the analysis showed is crucial. The efficacy of intratumoral injection of cytokines which is one type of immunotherapy is affected by properties of the tumor microenvironment as well as those of the design of the cytokines. Furthermore, the efficacy of the ICB immunotherapy is also affected by properties of the tumor microenvironment as well as of properties of the drug. For those two properties stand out, the effect of the administered dose of the drug as well as the number of functional vessels. Thus, normalization treatment improves perfusion and increases the concentration of immune cells at the tumor center.

Although the tumor microenvironment plays a crucial role in the outcome of treatment there are various other factors affecting the efficacy of immunotherapy. One of those factors that emerged the last few years is the gut microbiome. Both the microbiome and the immune system are complex systems that consist of various cells with multiple functions and effects. Although modelling the whole immune system would be impossible, the feasible approach is the creation of a mechanistic model of the immune system response that focuses on key immune cells and functions. On the other hand, little is known about the individual microbes that stand out on assisting immunotherapy making it hard to develop a mechanistic model

for all those microbes. Thus, the developed mechanistic model of tumor growth and immune response can be combined with other approaches like an association analysis to shed light on mechanisms hiding behind larger datasets.

Future work aims to combine the different variations-applications of the model in a unified mathematical modelling framework as presented in Figure 1. The unified mathematical framework can enable predictions on the outcome of various therapies for an individual patient. This can be used as a tool for the planning of the optimal treatment strategy for each individual. An optimal personalised treatment strategy includes administration of the drug or combination of drugs at the optimal dosage. This can be done by simulating various drug designs and treatment protocols. The optimal treatment strategy can also include adjustment of other factors affecting the treatment outcome like altering the gut microbiome of the patient prior to treatment. With this approach the patients will avoid undergoing non-beneficial treatment procedures and also maximize the benefit of less beneficial strategies.

References

1. Stylianopoulos T, Munn LL, Jain RK. Reengineering the Physical Microenvironment of Tumors to Improve Drug Delivery and Efficacy: From Mathematical Modeling to Bench to Bedside. Trends in Cancer. 2018;4: 292–319. doi:10.1016/j.trecan.2018.02.005

2. Jain RK, Martin JD, Stylianopoulos T. The Role of Mechanical Forces in Tumor Growth and Therapy. Annual Review of Biomedical Engineering. 2014;16: 321–346. doi:10.1146/annurev-bioeng-071813-105259

3. Stylianopoulos T. The Solid Mechanics of Cancer and Strategies for Improved Therapy. Journal of Biomechanical Engineering. 2017;139: 021004. doi:10.1115/1.4034991

4. Voutouri C, Stylianopoulos T. Accumulation of mechanical forces in tumors is related to hyaluronan content and tissue stiffness. PLoS ONE. 2018;13: e0193801. doi:10.1371/journal.pone.0193801

5. Stylianopoulos T, Martin JD, Chauhan VP, Jain SR, Diop-Frimpong B, Bardeesy N, et al. Causes, consequences, and remedies for growth-induced solid stress in murine and human tumors. Proceedings of the National Academy of Sciences of the United States of America. 2012;109: 15101–15108. doi:10.1073/pnas.1213353109

6. Voutouri C, Mpekris F, Papageorgis P, Odysseos AD, Stylianopoulos T. Role of constitutive behavior and tumor-host mechanical interactions in the state of stress and growth of solid tumors. PLoS ONE. 2014;9: e104717. doi:10.1371/journal.pone.0104717

7. Voutouri C, Polydorou C, Papageorgis P, Gkretsi V, Stylianopoulos T. Hyaluronan-Derived Swelling of Solid Tumors, the Contribution of Collagen and Cancer Cells, and Implications for Cancer Therapy. Neoplasia (United States). 2016;18: 732–741. doi:10.1016/j.neo.2016.10.001

8. Stylianopoulos T. The Solid Mechanics of Cancer and Strategies for Improved Therapy. Journal of Biomechanical Engineering. 2017;139. doi:10.1115/1.4034991

9. Boucher Y, Jain RK. Microvascular Pressure Is the Principal Driving Force for Interstitial Hypertension in Solid Tumors: Implications for Vascular Collapse. Cancer Research. 1992;52: 5110–5114.

10. Boucher Y, Baxter LT, Jain RK. Interstitial Pressure Gradients in Tissue-isolated and Subcutaneous Tumors: Implications for Therapy. Cancer Research. 1990;50: 4478–4484.

11. Baxter LT, Jain RK. Transport of fluid and macromolecules in tumors. I. Role of interstitial pressure and convection. Microvascular Research. 1989;37: 77–104. doi:10.1016/0026-2862(89)90074-5

12. Baxter LT, Jain RK. Transport of fluid and macromolecules in tumors. II. Role of heterogeneous perfusion and lymphatics. Microvascular Research. 1990;40: 246–263. doi:10.1016/0026-2862(90)90023-K

13. Baxter LT, Jain RK. Transport of fluid and macromolecules in tumors: III. Role of binding and metabolism. Microvascular Research. 1991;41: 5–23. doi:10.1016/0026-2862(91)90003-T

14. Baxter LT, Jain RK. Transport of fluid and macromolecules in tumors. IV. A microscopic model of the perivascular distribution. Microvascular Research. 1991;41: 252–272. doi:10.1016/0026-2862(91)90026-8

15. Hatzikirou H, Basanta D, Simon M, Schaller K, Deutsch A. “Go or grow”: the key to the emergence of invasion in tumour progression? Mathematical medicine and biology : a journal of the IMA. 2012;29: 49–65. doi:10.1093/IMAMMB/DQQ011

16. Huang Y, Goel S, Duda DG, Fukumura D, Jain RK. Vascular Normalization as an Emerging Strategy to Enhance Cancer Immunotherapy. Cancer Research. 2013;73: 2943–2948. doi:10.1158/0008-5472.CAN-12-4354

17. Noman MZ, Hasmim M, Messai Y, Terry S, Kieda C, Janji B, et al. Hypoxia: a key player in antitumor immune response. A Review in the Theme: Cellular Responses to Hypoxia. American Journal of Physiology-Cell Physiology. 2015;309: C569–C579. doi:10.1152/ajpcell.00207.2015

18. Stylianopoulos T, Munn LL, Jain RK. Reengineering the Physical Microenvironment of Tumors to Improve Drug Delivery and Efficacy: From Mathematical Modeling to Bench to Bedside. Trends in cancer. 2018/03/13 ed. 2018;4: 292–319. doi:10.1016/j.trecan.2018.02.005

19. Lee JB, Kim HR, Ha S-J. Immune Checkpoint Inhibitors in 10 Years: Contribution of Basic Research and Clinical Application in Cancer Immunotherapy. Immune Network. 2022;22: e2. doi:10.4110/in.2022.22.e2

20. Agarwal Y, Milling LE, Chang JYH, Santollani L, Sheen A, Lutz EA, et al. Intratumourally injected alum-tethered cytokines elicit potent and safer local and systemic anticancer immunity. Nature Biomedical Engineering. 2022;6: 129–143. doi:10.1038/s41551-021-00831-9

21. Momin N, Mehta NK, Bennett NR, Ma L, Palmeri JR, Chinn MM, et al. Anchoring of intratumorally administered cytokines to collagen safely potentiates systemic cancer immunotherapy. Science Translational Medicine. 2019;11: eaaw2614. doi:10.1126/scitranslmed.aaw2614

22. Momin N, Palmeri JR, Lutz EA, Jailkhani N, Mak H, Tabet A, et al. Maximizing response to intratumoral immunotherapy in mice by tuning local retention. Nature Communications. 2022;13: 109. doi:10.1038/s41467-021-27390-6

23. Haslam A, Prasad V. Estimation of the Percentage of US Patients With Cancer Who Are Eligible for and Respond to Checkpoint Inhibitor Immunotherapy Drugs. JAMA Network Open. 2019;2: e192535. doi:10.1001/jamanetworkopen.2019.2535

24. Ramos-Casals M, Brahmer JR, Callahan MK, Flores-Chávez A, Keegan N, Khamashta MA, et al. Immune-related adverse events of checkpoint inhibitors. Nature Reviews Disease Primers. 2020;6: 38. doi:10.1038/s41572-020-0160-6

25. Gopalakrishnan V, Spencer CN, Nezi L, Reuben A, Andrews MC, Karpinets TV, et al. Gut microbiome modulates response to anti–PD-1 immunotherapy in melanoma patients. Science. 2018;359: 97–103. doi:10.1126/science.aan4236

26. Gong J, Chehrazi-Raffle A, Placencio-Hickok V, Guan M, Hendifar A, Salgia R. The gut microbiome and response to immune checkpoint inhibitors: preclinical and clinical strategies. Clinical and Translational Medicine. 2019;8. doi:10.1186/s40169-019-0225-x

27. Rezasoltani S, Yadegar A, Asadzadeh Aghdaei H, Reza Zali M. Modulatory effects of gut microbiome in cancer immunotherapy: A novel paradigm for blockade of immune checkpoint inhibitors. Cancer Medicine. 2021;10: 1141–1154. doi:10.1002/cam4.3694

28. Matson V, Fessler J, Bao R, Chongsuwat T, Zha Y, Alegre M-L, et al. The commensal microbiome is associated with anti–PD-1 efficacy in metastatic melanoma patients. Science. 2018;359: 104–108. doi:10.1126/science.aao3290

29. Davar D, Dzutsev AK, McCulloch JA, Rodrigues RR, Chauvin J-M, Morrison RM, et al. Fecal microbiota transplant overcomes resistance to anti–PD-1 therapy in melanoma patients. Science. 2021;371: 595–602. doi:10.1126/science.abf3363

30. Baruch EN, Youngster I, Ben-Betzalel G, Ortenberg R, Lahat A, Katz L, et al. Fecal microbiota transplant promotes response in immunotherapy-refractory melanoma patients. Science. 2021;371: 602–609. doi:10.1126/science.abb5920

31. Spencer CN, McQuade JL, Gopalakrishnan V, McCulloch JA, Vetizou M, Cogdill AP, et al. Dietary fiber and probiotics influence the gut microbiome and melanoma immunotherapy response. Science. 2021;374: 1632–1640. doi:10.1126/science.aaz7015

32. Gao G, Shen S, Zhang T, Zhang J, Huang S, Sun Z, et al. Lacticaseibacillus rhamnosus Probio-M9 enhanced the antitumor response to anti-PD-1 therapy by modulating intestinal metabolites. eBioMedicine. 2023;91: 104533. doi:10.1016/j.ebiom.2023.104533

33. Sivan A, Corrales L, Hubert N, Williams JB, Aquino-Michaels K, Earley ZM, et al. Commensal *Bifidobacterium* promotes antitumor immunity and facilitates anti–PD-L1 efficacy. Science. 2015;350: 1084–1089. doi:10.1126/science.aac4255

34. Baruch EN, Youngster I, Ben-Betzalel G, Ortenberg R, Lahat A, Katz L, et al. Fecal microbiota transplant promotes response in immunotherapy-refractory melanoma patients. Science. 2021;371: 602–609. doi:10.1126/science.abb5920

35. Wasserman R, Acharya R, Sibata C, Shin KH. A patient-specific in vivo tumor model. Mathematical Biosciences. 1996;136: 111–140. doi:10.1016/0025-5564(96)00045-4

36. Siddiqui M, Rajkumar SV. The High Cost of Cancer Drugs and What We Can Do About It. Mayo Clinic Proceedings. 2012;87: 935–943. doi:10.1016/j.mayocp.2012.07.007

37. Malinzi J, Basita KB, Padidar S, Adeola HA. Prospect for application of mathematical models in combination cancer treatments. Informatics in Medicine Unlocked. 2021;23: 100534. doi:10.1016/j.imu.2021.100534

38. Wang Z, Butner JD, Cristini V, Deisboeck TS. Integrated PK-PD and agent-based modeling in oncology. Journal of Pharmacokinetics and Pharmacodynamics. 2015;42: 179–189. doi:10.1007/s10928-015-9403-7

39. Wang S, Guo P, Wang X, Zhou Q, Gallo JM. Preclinical pharmacokinetic/pharmacodynamic models of gefitinib and the design of equivalent dosing regimens in EGFR wild-type and mutant tumor models. Molecular Cancer Therapeutics. 2008;7: 407–417. doi:10.1158/1535-7163.MCT-07-2070

40. Jain RK, Wei J. Dynamics of drug transport in solid tumors: distributed parameter model. J Bioengineering. 1977;1: 313–329.

41. Mpekris F, Angeli S, Pirentis AP, Stylianopoulos T. Stress-mediated progression of solid tumors: effect of mechanical stress on tissue oxygenation, cancer cell proliferation, and drug delivery. Biomechanics and Modeling in Mechanobiology. 2015;14: 1391–1402. doi:10.1007/s10237-015-0682-0

42. Mpekris F, Voutouri C, Baish JW, Duda DG, Munn LL, Stylianopoulos T, et al. Combining microenvironment normalization strategies to improve cancer immunotherapy. Proceedings of the National Academy of Sciences. 2020;117: 3728–3737. doi:10.1073/pnas.1919764117

43. Anderson ARA, Chaplain MAJ, McDougall S. A hybrid discrete-continuum model of tumour induced angiogenesis. In: Jackson TLL, editor. Modeling tumor vasculature: Molecular, cellular, and tissue level aspects and implications. New York, NY: Springer New York; 2012. pp. 105–133. doi:10.1007/978-1-4614-0052-3_5

44. Angeli S, Emblem KE, Due-Tonnessen P, Stylianopoulos T. Towards patient-specific modeling of brain tumor growth and formation of secondary nodes guided by DTI-MRI. NeuroImage: Clinical. 2018;20: 664–673. doi:10.1016/j.nicl.2018.08.032

45. Harkos C, Svensson SF, Emblem KE, Stylianopoulos T. Inducing Biomechanical Heterogeneity in Brain Tumor Modeling by MR Elastography: Effects on Tumor Growth, Vascular Density and Delivery of Therapeutics. Cancers. 2022;14: 884. doi:10.3390/cancers14040884

46. Hamamoto R, Takasawa K, Machino H, Kobayashi K, Takahashi S, Bolatkan A, et al. Application of non-negative matrix factorization in oncology: one approach for

establishing precision medicine. Briefings in Bioinformatics. 2022;23: bbac246. doi:10.1093/bib/bbac246

47. Zeng Z, Vo AH, Mao C, Clare SE, Khan SA, Luo Y. Cancer classification and pathway discovery using non-negative matrix factorization. Journal of Biomedical Informatics. 2019;96: 103247. doi:10.1016/j.jbi.2019.103247

48. Deng X, Ali-Adeeb R, Andrews JL, Shreeves P, Lum JJ, Brolo A, et al. Monitor Ionizing Radiation-Induced Cellular Responses with Raman Spectroscopy, Non-Negative Matrix Factorization, and Non-Negative Least Squares. Applied Spectroscopy. 2020;74: 701–711. doi:10.1177/0003702820906221

49. Naik GR, editor. Non-negative Matrix Factorization Techniques: Advances in Theory and Applications. Berlin, Heidelberg: Springer Berlin Heidelberg; 2016. doi:10.1007/978-3-662-48331-2

50. Ostrom QT, Gittleman H, Fulop J, Liu M, Blanda R, Kromer C, et al. CBTRUS statistical Report: primary brain and central nervous system tumors diagnosed in the United States in 2008-2012. Neuro-Oncology. 2015;17: iv1–iv62. doi:10.1093/neuonc/nov189

51. Lym RL, Ostrom QT, Kruchko C, Couce M, Brat DJ, Louis DN, et al. Completeness and concordancy of WHO grade assignment for brain and central nervous system tumors in the United States, 2004–2011. Journal of Neuro-Oncology. 2015;123: 43–51. doi:10.1007/s11060-015-1775-4

52. Johnson DR, O'Neill BP. Glioblastoma survival in the United States before and during the temozolomide era. Journal of Neuro-Oncology. 2012;107: 359–364. doi:10.1007/s11060-011-0749-4

53. Stupp R, Hegi ME, Mason WP, van den Bent MJ, Taphoorn MJ, Janzer RC, et al. Effects of radiotherapy with concomitant and adjuvant temozolomide versus radiotherapy alone on survival in glioblastoma in a randomised phase III study: 5-year analysis of the EORTC-NCIC trial. The Lancet Oncology. 2009;10: 459–466. doi:10.1016/S1470-2045(09)70025-7

54. Alfonso JCL, Talkenberger K, Seifert M, Klink B, Hawkins-Daarud A, Swanson KR, et al. The biology and mathematical modelling of glioma invasion: a review. Journal of The Royal Society Interface. 2017;14. doi:10.1098/RSIF.2017.0490

55. Falco J, Agosti A, Vetrano IG, Bizzi A, Restelli F, Broggi M, et al. In Silico Mathematical Modelling for Glioblastoma: A Critical Review and a Patient-Specific Case. Journal of Clinical Medicine 2021, Vol 10, Page 2169. 2021;10: 2169. doi:10.3390/JCM10102169

56. Protopapa M, Zygogianni A, Stamatakos GS, Antypas C, Armpilia C, Uzunoglu NK, et al. Clinical implications of in silico mathematical modeling for glioblastoma: a critical review. Journal of Neuro-Oncology 2017 136:1. 2017;136: 1–11. doi:10.1007/S11060-017-2650-2

57. Juffer AH, Marin U, Niemitalo O, Koivukangas J. Computer modeling of brain tumor growth. Mini Reviews In Medicinal Chemistry. 2008;8: 1494–1506. doi:10.2174/138955708786786471

58. Swanson KR, Alvord EC, Murray JD. Virtual brain tumours (gliomas) enhance the reality of medical imaging and highlight inadequacies of current therapy. British Journal of Cancer. 2002;86: 14–18. doi:10.1038/sj.bjc.6600021

59. Swanson KR, Alvord J, Murray JD. A quantitative model for differential motility of gliomas in grey and white matter. Cell Proliferation. 2000;33: 317–329. doi:10.1046/j.1365-2184.2000.00177.x

60. Harpold HLP, Alvord EC, Swanson KR. The Evolution of Mathematical Modeling of Glioma Proliferation and Invasion. Journal of Neuropathology and Experimental Neurology. 2007;66: 1–9. doi:10.1097/nen.0b013e31802d9000

61. Jbabdi S, Mandonnet E, Duffau H, Capelle L, Swanson KR, Pélégrini-Issac M, et al. Simulation of anisotropic growth of low-grade gliomas using diffusion tensor imaging. Magnetic Resonance in Medicine. 2005;54: 616–624. doi:10.1002/mrm.20625

62. Colombo MC, Giverso C, Faggiano E, Boffano C, Acerbi F, Ciarletta P. Towards the personalized treatment of glioblastoma: Integrating patient-specific clinical data in a continuous mechanical model. PLoS ONE. 2015;10: e0132887. doi:10.1371/journal.pone.0132887

63. Sakkalis V, Roniotis A, Farmaki C, Karatzanis I, Marias K. Evaluation framework for the multilevel macroscopic models of solid tumor growth in the glioma case. Annual International Conference of the IEEE Engineering in Medicine and Biology Society IEEE

Engineering in Medicine and Biology Society Annual International Conference. 2010;2010: 6809–6812. doi:10.1109/IEMBS.2010.5625961

64. Roniotis A, Manikis GC, Sakkalis V, Zervakis ME, Karatzanis I, Marias K. High-grade glioma diffusive modeling using statistical tissue information and diffusion tensors extracted from atlases. IEEE transactions on information technology in biomedicine : a publication of the IEEE Engineering in Medicine and Biology Society. 2012;16: 255–263. doi:10.1109/TITB.2011.2171190

65. Rockne R, Rockhill JK, Mrugala M, Spence AM, Kalet I, Hendrickson K, et al. Predicting the efficacy of radiotherapy in individual glioblastoma patients in vivo: A mathematical modeling approach. Physics in Medicine and Biology. 2010;55: 3271–3285. doi:10.1088/0031-9155/55/12/001

66. Unkelbach J, Menze BH, Konukoglu E, Dittmann F, Ayache N, Shih HA. Radiotherapy planning for glioblastoma based on a tumor growth model: Implications for spatial dose redistribution. Physics in Medicine and Biology. 2014;59: 771–789. doi:10.1088/0031-9155/59/3/771

67. Lipkova J, Angelikopoulos P, Wu S, Alberts E, Wiestler B, Diehl C, et al. Personalized Radiotherapy Design for Glioblastoma: Integrating Mathematical Tumor Models, Multimodal Scans, and Bayesian Inference. IEEE Transactions on Medical Imaging. 2019;38: 1875–1884. doi:10.1109/TMI.2019.2902044

68. Roniotis A, Marias K, Sakkalis V, Manikis GC, Zervakis M. Simulating radiotherapy effect in high-grade glioma by using diffusive modeling and brain atlases. Journal of Biomedicine and Biotechnology. 2012;2012. doi:10.1155/2012/715812

69. Stamatakos GS, Antipas VP, Uzunoglu NK. A spatiotemporal, patient individualized simulation model of solid tumor response to chemotherapy in vivo: The paradigm of glioblastoma multiforme treated by temozolomide. IEEE Transactions on Biomedical Engineering. 2006;53: 1467–1477. doi:10.1109/TBME.2006.873761

70. Tracqui P, Cruywagen GC, Woodward DE, Bartoo GT, Murray JD, Alvord EC. A mathematical model of glioma growth: the effect of chemotherapy on spatio-temporal growth. Cell Proliferation. 1995;28: 17–31. doi:10.1111/j.1365-2184.1995.tb00036.x

71. Subramanian S, Gholami A, Biros G. Simulation of glioblastoma growth using a 3D multispecies tumor model with mass effect. Journal of Mathematical Biology. 2019;79: 941–967. doi:10.1007/S00285-019-01383-Y/TABLES/6

72. Angeli S, Stylianopoulos T. Biphasic modeling of brain tumor biomechanics and response to radiation treatment. Journal of Biomechanics. 2016;49: 1524–1531. doi:10.1016/j.jbiomech.2016.03.029

73. Seano G, Nia H, Emblem K, Datta M, Ren J, Krishnan S, et al. Solid stress in brain tumours causes neuronal loss and neurological dysfunction and can be reversed by lithium. Nature biomedical engineering. 2019;3: 230–245. doi:10.1038/S41551-018-0334-7

74. Jain RK, Martin JD, Stylianopoulos T. The Role of Mechanical Forces in Tumor Growth and Therapy. Annual Review of Biomedical Engineering. 2014;16: 321–346. doi:10.1146/annurev-bioeng-071813-105259

75. Voutouri C, Stylianopoulos T. Accumulation of mechanical forces in tumors is related to hyaluronan content and tissue stiffness. PLoS ONE. 2018;13: e0193801. doi:10.1371/journal.pone.0193801

76. Macklin P, Lowengrub J. Nonlinear simulation of the effect of microenvironment on tumor growth. Journal of Theoretical Biology. 2007;245: 677–704. doi:10.1016/j.jtbi.2006.12.004

77. Frieboes HB, Lowengrub JS, Wise S, Zheng X, Macklin P, Bearer EL, et al. Computer simulation of glioma growth and morphology. NeuroImage. 2007;37: S59. doi:10.1016/j.neuroimage.2007.03.008

78. Kim Y, Roh S. A hybrid model for cell proliferation and migration in glioblastoma. Discrete & Continuous Dynamical Systems - B 2013, Volume 18, Pages 969-1015. 2013;18: 969. doi:10.3934/DCDSB.2013.18.969

79. Tunc B, Hormuth D, Biros G, Yankeelov TE. Modeling of Glioma Growth with Mass Effect by Longitudinal Magnetic Resonance Imaging. IEEE Transactions on Biomedical Engineering. 2021. doi:10.1109/TBME.2021.3085523

80. Kalli M, Voutouri C, Minia A, Pliaka V, Fotis C, Alexopoulos LG, et al. Mechanical Compression Regulates Brain Cancer Cell Migration Through MEK1/Erk1 Pathway

Activation and GDF15 Expression. Frontiers In Oncology. 2019;9. doi:10.3389/FONC.2019.00992

81. Mascheroni P, Alfonso JCL, Kalli M, Stylianopoulos T, Meyer-Hermann M, Hatzikirou H. On the Impact of Chemo-Mechanically Induced Phenotypic Transitions in Gliomas. Cancers. 2019;11. doi:10.3390/cancers11050716

82. Mpekris F, Angeli S, Pirentis AP, Stylianopoulos T. Stress-mediated progression of solid tumors: effect of mechanical stress on tissue oxygenation, cancer cell proliferation, and drug delivery. Biomechanics and Modeling in Mechanobiology. 2015;14: 1391–1402. doi:10.1007/s10237-015-0682-0

83. Saut O, Lagaert JB, Colin T, Fathallah-Shaykh HM. A Multilayer Grow-or-Go Model for GBM: Effects of Invasive Cells and Anti-Angiogenesis on Growth. Bulletin of Mathematical Biology. 2014;76: 2306–2333. doi:10.1007/s11538-014-0007-y

84. Alfonso JCL, Köhn-Luque A, Stylianopoulos T, Feuerhake F, Deutsch A, Hatzikirou H. Why one-size-fits-all vaso-modulatory interventions fail to control glioma invasion: In silico insights. Scientific Reports. 2016;6. doi:10.1038/srep37283

85. Swanson KR, Rostomily RC, Alvord EC. A mathematical modelling tool for predicting survival of individual patients following resection of glioblastoma: A proof of principle. British Journal of Cancer. 2008;98: 113–119. doi:10.1038/sj.bjc.6604125

86. Papadogiorgaki M, Koliou P, Kotsiakis X, Zervakis ME. Mathematical modelling of spatio-temporal glioma evolution. Theoretical Biology and Medical Modelling. 2013;10: 47. doi:10.1186/1742-4682-10-47

87. Batchelor TT, Gerstner ER, Emblem KE, Duda DG, Kalpathy-Cramer J, Snuderl M, et al. Improved tumor oxygenation and survival in glioblastoma patients who show increased blood perfusion after cediranib and chemoradiation. Proceedings of the National Academy of Sciences of the United States of America. 2013;110: 19059–19064. doi:10.1073/pnas.1318022110

88. Sorensen AG, Emblem KE, Polaskova P, Jennings D, Kim H, Ancukiewicz M, et al. Increased survival of glioblastoma patients who respond to antiangiogenic therapy with elevated blood perfusion. Cancer Research. 2012;72: 402–407. doi:10.1158/0008-5472.CAN-11-2464

89. Hormuth DA, Weis JA, Barnes SL, Miga MI, Rericha EC, Quaranta V, et al. A mechanically coupled reaction–diffusion model that incorporates intra-tumoural heterogeneity to predict in vivo glioma growth. Journal of The Royal Society Interface. 2017;14. doi:10.1098/RSIF.2016.1010

90. Dohm AE, Nickles TM, Miller CE, Bowers HJ, Miga MI, Attia A, et al. Clinical assessment of a biophysical model for distinguishing tumor progression from radiation necrosis. Medical Physics. 2021;48: 3852–3859. doi:10.1002/MP.14999

91. Jamin Y, Boult JKR, Li J, Popov S, Garteiser P, Ulloa JL, et al. Exploring the biomechanical properties of brain malignancies and their pathologic determinants in vivo with magnetic resonance elastography. Cancer Research. 2015;75: 1216–1224. doi:10.1158/0008-5472.CAN-14-1997

92. Hiscox L V., Johnson CL, Barnhill E, McGarry MDJ, Huston J, Van Beek EJR, et al. Magnetic resonance elastography (MRE) of the human brain: Technique, findings and clinical applications. Physics in Medicine and Biology. 2016;61: R401–R437. doi:10.1088/0031-9155/61/24/R401

93. Schregel K, Nazari N, Nowicki MO, Palotai M, Lawler SE, Sinkus R, et al. Characterization of glioblastoma in an orthotopic mouse model with magnetic resonance elastography. NMR in Biomedicine. 2018;31: e3840. doi:10.1002/nbm.3840

94. Katsamba I, Evangelidis P, Voutouri C, Tsamis A, Vavourakis V, Stylianopoulos T. Biomechanical modelling of spinal tumour anisotropic growth. Proceedings of the Royal Society A: Mathematical, Physical and Engineering Sciences. 2020;476: 20190364. doi:10.1098/rspa.2019.0364

95. Helmlinger G, Netti PA, Lichtenbeld HC, Melder RJ, Jain RK. Solid stress inhibits the growth of multicellular tumor spheroids. Nature Biotechnology. 1997;15: 778–783. doi:10.1038/nbt0897-778

96. Cheng G, Tse J, Jain RK, Munn LL. Micro-environmental mechanical stress controls tumor spheroid size and morphology by suppressing proliferation and inducing apoptosis in cancer cells. PLoS ONE. 2009;4: e4632. doi:10.1371/journal.pone.0004632

97. Kaufman LJ, Brangwynne CP, Kasza KE, Filippidi E, Gordon VD, Deisboeck TS, et al. Glioma expansion in collagen I matrices: Analyzing collagen concentration-dependent

growth and motility patterns. Biophysical Journal. 2005;89: 635–650. doi:10.1529/biophysj.105.061994

98. Delarue M, Montel F, Vignjevic D, Prost J, Joanny JF, Cappello G. Compressive stress inhibits proliferation in tumor spheroids through a volume limitation. Biophysical Journal. 2014;107: 1821–1828. doi:10.1016/j.bpj.2014.08.031

99. Fløgstad Svensson S, Fuster-Garcia E, Latysheva A, Fraser-Green J, Nordhøy W, Isam Darwish O, et al. Decreased tissue stiffness in glioblastoma by MR elastography is associated with increased cerebral blood flow. European Journal of Radiology. 2022;147: 110136. doi:10.1016/J.EJRAD.2021.110136

100. Runge JH, Hoelzl SH, Sudakova J, Dokumaci AS, Nelissen JL, Guenthner C, et al. A novel magnetic resonance elastography transducer concept based on a rotational eccentric mass: preliminary experiences with the gravitational transducer. Physics in Medicine & Biology. 2019;64: 045007. doi:10.1088/1361-6560/AAF9F8

101. Svensson SF, Arcos J De, Darwish OI, Fraser-Green J, Storås TH, Holm S, et al. Robustness of MR Elastography in the Healthy Brain: Repeatability, Reliability, and Effect of Different Reconstruction Methods. Journal of Magnetic Resonance Imaging. 2021;53: 1510–1521. doi:10.1002/JMRI.27475

102. Fovargue D, Kozerke S, Sinkus R, Nordsletten D. Robust MR elastography stiffness quantification using a localized divergence free finite element reconstruction. Medical Image Analysis. 2018;44: 126–142. doi:10.1016/J.MEDIA.2017.12.005

103. Li S, Zhao G, Chen H. The Relationship between Steady Shear Viscosity and Complex Viscosity. Journal of Dispersion Science and Technology. 2005;26: 415–419. doi:10.1081/DIS-200054555

104. Rodriguez EK, Hoger A, McCulloch AD. Stress-dependent finite growth in soft elastic tissues. Journal of Biomechanics. 1994;27: 455–467. doi:10.1016/0021-9290(94)90021-3

105. Skalak R, Zargaryan S, Jain RK, Netti PA, Hoger A. Compatibility and the genesis of residual stress by volumetric growth. Journal of Mathematical Biology. 1996;34: 889–914. doi:10.1007/BF01834825

106. MacLaurin J, Chapman J, Jones GW, Roose T. The buckling of capillaries in solid tumours. Proceedings of the Royal Society A: Mathematical, Physical and Engineering Sciences. 2012;468: 4123–4145. doi:10.1098/rspa.2012.0418

107. Ambrosi D, Mollica F. On the mechanics of a growing tumor. International Journal of Engineering Science. 2002;40: 1297–1316. doi:10.1016/S0020-7225(02)00014-9

108. Mow VC, Kuei SC, Lai WM, Armstrong CG. Biphasic creep and stress relaxation of articular cartilage in compression: Theory and experiments. Journal of Biomechanical Engineering. 1980;102: 73–84. doi:10.1115/1.3138202

109. Taber LA. Theoretical study of Beloussov's hyper-restoration hypothesis for mechanical regulation of morphogenesis. Biomechanics and Modeling in Mechanobiology. 2008;7: 427–441. doi:10.1007/s10237-007-0106-x

110. Ciarletta P. Buckling instability in growing tumor spheroids. Physical Review Letters. 2013;110. doi:10.1103/PhysRevLett.110.158102

111. Stein AM, Demuth T, Mobley D, Berens M, Sander LM. A mathematical model of glioblastoma tumor spheroid invasion in a three-dimensional in vitro experiment. Biophysical Journal. 2007;92: 356–365. doi:10.1529/biophysj.106.093468

112. Engwer C, Knappitsch M, Surulescu C. A multiscale model for glioma spread including cell-tissue interactions and proliferation. Mathematical Biosciences and Engineering. 2016;13: 443–460. doi:10.3934/mbe.2015011

113. Stylianopoulos T, Yeckel A, Derby JJ, Luo XJ, Shephard MS, Sander EA, et al. Permeability calculations in three-dimensional isotropic and oriented fiber networks. Physics of Fluids. 2008;20: 123601. doi:10.1063/1.3021477

114. Zakariapour M, Hamedi MH, Fatouraee N. Características do fluxo de fluido intersticial junto com o fluxo sanguíneo no interior de um tumor cilíndrico: Uma simulação numérica. Acta Scientiarum - Technology. 2018;40. doi:10.4025/ACTASCITECHNOL.V40I1.30792

115. Baxter LT, Jain RK. Transport of fluid and macromolecules in tumors. I. Role of interstitial pressure and convection. Microvascular Research. 1989;37: 77–104. doi:10.1016/0026-2862(89)90074-5

116. Stylianopoulos T, Martin JD, Snuderl M, Mpekris F, Jain SR, Jain RK. Coevolution of solid stress and interstitial fluid pressure in tumors during progression: Implications for vascular collapse. Cancer Research. 2013;73: 3833–3841. doi:10.1158/0008-5472.CAN-12-4521

117. Roose T, Netti PA, Munn LL, Boucher Y, Jain RK. Solid stress generated by spheroid growth estimated using a linear poroelasticity model. Microvascular Research. 2003;66: 204–212. doi:10.1016/S0026-2862(03)00057-8

118. Kim Y, Stolarska MA, Othmer HG. The role of the microenvironment in tumor growth and invasion. Progress in biophysics and molecular biology. 2011/06/28 ed. 2011;106: 353–379. doi:10.1016/j.pbiomolbio.2011.06.006

119. Stylianopoulos T, Economides E-A, Baish JW, Fukumura D, Jain RK. Towards Optimal Design of Cancer Nanomedicines: Multi-stage Nanoparticles for the Treatment of Solid Tumors. Annals of biomedical engineering. 2015;43: 2291–2300. doi:10.1007/S10439-015-1276-9

120. Deen WM. Hindered transport of large molecules in liquid-filled pores. AIChE Journal. 1987;33: 1409–1425. doi:10.1002/aic.690330902

121. Hobbs SK, Monsky WL, Yuan F, Roberts WG, Griffith L, Torchilin VP, et al. Regulation of transport pathways in tumor vessels: Role of tumor type and microenvironment. Proceedings of the National Academy of Sciences of the United States of America. 1998;95: 4607–4612. doi:10.1073/pnas.95.8.4607

122. Bunevicius A, Schregel K, Sinkus R, Golby A, Patz S. REVIEW: MR elastography of brain tumors. NeuroImage: Clinical. 2020;25: 102109. doi:10.1016/J.NICL.2019.102109

123. Clarke EC, Cheng S, Green M, Sinkus R, Bilston LE. Using static preload with magnetic resonance elastography to estimate large strain viscoelastic properties of bovine liver. Journal of Biomechanics. 2011;44: 2461–2465. doi:10.1016/j.jbiomech.2011.06.023

124. Pagé G, Tardieu M, Besret L, Blot L, Lopes J, Sinkus R, et al. Assessing Tumor Mechanics by MR Elastography at Different Strain Levels. Journal of Magnetic Resonance Imaging. 2019;50: 1982–1989. doi:10.1002/jmri.26787

125. Rakesh K. Jain. Antiangiogenesis Strategies Revisited: From Starving Tumors to Alleviating Hypoxia. Cancer Cell. 2014;26: 605–622. doi:10.1016/j.ccell.2014.10.006

126. Fukumura D, Kloepper J, Amoozgar Z, Duda DG, Jain RK. Enhancing cancer immunotherapy using antiangiogenics: opportunities and challenges. Nature Reviews Clinical Oncology. 2018;15: 325–340. doi:10.1038/nrclinonc.2018.29

127. Patel SA, Nilsson MB, Le X, Cascone T, Jain RK, Heymach JV. Molecular Mechanisms and Future Implications of VEGF/VEGFR in Cancer Therapy. Clinical Cancer Research. 2023;29: 30–39. doi:10.1158/1078-0432.CCR-22-1366

128. Leslie M. New partners reinvigorate a once-touted cancer treatment. Science. 2023;380: 679–680. doi:10.1126/science.adi7657

129. Hong WX, Haebe S, Lee AS, Westphalen CB, Norton JA, Jiang W, et al. Intratumoral Immunotherapy for Early-stage Solid Tumors. Clinical Cancer Research. 2020;26: 3091–3099. doi:10.1158/1078-0432.CCR-19-3642

130. Champiat S, Tselikas L, Farhane S, Raoult T, Texier M, Lanoy E, et al. Intratumoral Immunotherapy: From Trial Design to Clinical Practice. Clinical Cancer Research. 2021;27: 665–679. doi:10.1158/1078-0432.CCR-20-0473

131. Yuan J, Khilnani A, Brody J, Andtbacka RHI, Hu-Lieskovan S, Luke JJ, et al. Current strategies for intratumoural immunotherapy – Beyond immune checkpoint inhibition. European Journal of Cancer. 2021;157: 493–510. doi:10.1016/j.ejca.2021.08.004

132. Milling L, Zhang Y, Irvine DJ. Delivering safer immunotherapies for cancer. Advanced Drug Delivery Reviews. 2017;114: 79–101. doi:10.1016/j.addr.2017.05.011

133. Lasek W, Zagożdżon R, Jakobisiak M. Interleukin 12: still a promising candidate for tumor immunotherapy? Cancer Immunology, Immunotherapy. 2014;63: 419–435. doi:10.1007/s00262-014-1523-1

134. June CH, Warshauer JT, Bluestone JA. Is autoimmunity the Achilles' heel of cancer immunotherapy? Nature Medicine. 2017;23: 540–547. doi:10.1038/nm.4321

135. Nguyen KG, Vrabel MR, Mantooth SM, Hopkins JJ, Wagner ES, Gabaldon TA, et al. Localized Interleukin-12 for Cancer Immunotherapy. Frontiers in Immunology. 2020;11: 575597. doi:10.3389/fimmu.2020.575597

136. Van Herpen CML, Van Der Voort R, Van Der Laak JAWM, Klasen IS, De Graaf AO, Van Kempen LCL, et al. Intratumoral rhIL-12 administration in head and neck squamous cell carcinoma patients induces B cell activation. International Journal of Cancer. 2008;123: 2354–2361. doi:10.1002/ijc.23756

137. Pfreundschuh MG, Tilman Steinmetz H, Tüschen R, Schenk V, Diehl V, Schaadt M. Phase I study of intratumoral application of recombinant human tumor necrosis factor. European Journal of Cancer and Clinical Oncology. 1989;25: 379–388. doi:10.1016/0277-5379(89)90034-5

138. Yousefpour P, Ni K, Irvine DJ. Targeted modulation of immune cells and tissues using engineered biomaterials. Nature Reviews Bioengineering. 2023;1: 107–124. doi:10.1038/s44222-022-00016-2

139. Boucher Y, Baxter LT, Jain RK. Interstitial pressure gradients in tissue-isolated and subcutaneous tumors: implications for therapy. Cancer research. 1990;50: 4478–4484.

140. Boucher Y, Jain RK. Microvascular pressure is the principal driving force for interstitial hypertension in solid tumors: implications for vascular collapse. Cancer Res. 1992;52: 5110–5114.

141. Nia HT, Munn LL, Jain RK. Physical traits of cancer. Science. 2020;370: eaaz0868. doi:10.1126/science.aaz0868

142. Campbell RB, Fukumura D, Brown EB, Mazzola LM, Izumi Y, Jain RK, et al. Cationic charge determines the distribution of liposomes between the vascular and extravascular compartments of tumors. Cancer Research. 2002;62: 6831–6836.

143. Stylianopoulos T, Soteriou K, Fukumura D, Jain RK. Cationic Nanoparticles Have Superior Transvascular Flux into Solid Tumors: Insights from a Mathematical Model. Annals of Biomedical Engineering. 2013;41: 68–77. doi:10.1007/s10439-012-0630-4

144. Chauhan VP, Stylianopoulos T, Martin JD, Popović Z, Chen O, Kamoun WS, et al. Normalization of tumour blood vessels improves the delivery of nanomedicines in a size-dependent manner. Nature Nanotechnology. 2012;7: 383–388. doi:10.1038/nnano.2012.45

145. Lai X, Friedman A. Combination therapy of cancer with cancer vaccine and immune checkpoint inhibitors: A mathematical model. PLoS ONE. 2017;12: e0178479. doi:10.1371/journal.pone.0178479

146. Friedman A, Hao W. The Role of Exosomes in Pancreatic Cancer Microenvironment. Bulletin of Mathematical Biology. 2018;80: 1111–1133. doi:10.1007/s11538-017-0254-9

147. Pluen A, Boucher Y, Ramanujan S, McKee TD, Gohongi T, Di Tomaso E, et al. Role of tumor–host interactions in interstitial diffusion of macromolecules: Cranial vs. subcutaneous tumors. Proceedings of the National Academy of Sciences. 2001;98: 4628–4633. doi:10.1073/pnas.081626898

148. Voutouri C, Stylianopoulos T. Evolution of osmotic pressure in solid tumors. Journal of Biomechanics. 2014;47: 3441–3447. doi:10.1016/j.jbiomech.2014.09.019

149. Schmidt MM, Wittrup KD. A modeling analysis of the effects of molecular size and binding affinity on tumor targeting. Molecular Cancer Therapeutics. 2009;8: 2861–2871. doi:10.1158/1535-7163.MCT-09-0195

150. Mpekris F, Baish JW, Stylianopoulos T, Jain RK. Role of vascular normalization in benefit from metronomic chemotherapy. Proceedings of the National Academy of Sciences. 2017;114: 1994–1999. doi:10.1073/pnas.1700340114

151. Roose T, Netti PA, Munn LL, Boucher Y, Jain RK. Solid stress generated by spheroid growth estimated using a linear poroelasticity model. Microvascular Research. 2003;66: 204–212. doi:10.1016/S0026-2862(03)00057-8

152. Kim Y, Stolarska MA, Othmer HG. The role of the microenvironment in tumor growth and invasion. Progress in Biophysics and Molecular Biology. 2011;106: 353–379. doi:10.1016/j.pbiomolbio.2011.06.006

153. Mok W, Stylianopoulos T, Boucher Y, Jain RK. Mathematical modeling of herpes simplex virus distribution in solid tumors: Implications for cancer gene therapy. Clinical Cancer Research. 2009;15: 2352–2360. doi:10.1158/1078-0432.CCR-08-2082

154. Smilgies D-M, Folta-Stogniew E. Molecular weight–gyration radius relation of globular proteins: a comparison of light scattering, small-angle X-ray scattering and

structure-based data. Journal of Applied Crystallography. 2015;48: 1604–1606. doi:10.1107/S1600576715015551

155. Zakariapour M, Hamedi MH, Fatouraee N. Characteristics of interstitial fluid flow along with blood flow inside a cylindrical tumor: a numerical simulation. Acta Scientiarum Technology. 2018;40: 30792. doi:10.4025/actascitechnol.v40i1.30792

156. Panagi M, Mpekris F, Voutouri C, Michael C, Constantinidou A, Martin JD, et al. Abstract 6382: Targeting mast cells restores T cell infiltration and sensitizes sarcomas to PD-L1 inhibition. Cancer Research. 2022;82: 6382–6382. doi:10.1158/1538-7445.AM2022-6382

157. Barsoum IB, Smallwood CA, Siemens DR, Graham CH. A Mechanism of Hypoxia-Mediated Escape from Adaptive Immunity in Cancer Cells. Cancer Research. 2014;74: 665–674. doi:10.1158/0008-5472.CAN-13-0992

158. Jain RK, Tong RT, Munn LL. Effect of Vascular Normalization by Antiangiogenic Therapy on Interstitial Hypertension, Peritumor Edema, and Lymphatic Metastasis: Insights from a Mathematical Model. Cancer Research. 2007;67: 2729–2735. doi:10.1158/0008-5472.CAN-06-4102

159. Hobbs SK, Monsky WL, Yuan F, Roberts WG, Griffith L, Torchilin VP, et al. Regulation of transport pathways in tumor vessels: Role of tumor type and microenvironment. Proceedings of the National Academy of Sciences. 1998;95: 4607–4612. doi:10.1073/pnas.95.8.4607

160. Netti PA, Berk DA, Swartz MA, Grodzinsky AJ, Jain RK. Role of Extracellular Matrix Assembly in Interstitial Transport in Solid Tumors. Cancer Research. 2000;60: 2497–2503.

161. Stylianopoulos T, Jain RK. Combining two strategies to improve perfusion and drug delivery in solid tumors. Proceedings of the National Academy of Sciences. 2013;110: 18632–18637. doi:10.1073/pnas.1318415110

162. Jain RK. Normalization of Tumor Vasculature: An Emerging Concept in Antiangiogenic Therapy. Science. 2005;307: 58–62. doi:10.1126/science.1104819

163. Martin JD, Cabral H, Stylianopoulos T, Jain RK. Improving cancer immunotherapy using nanomedicines: progress, opportunities and challenges. Nature Reviews Clinical Oncology. 2020;17: 251–266. doi:10.1038/s41571-019-0308-z

164. Wittrup KD, Kaufman HL, Schmidt MM, Irvine DJ. Intratumorally anchored cytokine therapy. Expert Opinion on Drug Delivery. 2022;19: 725–732. doi:10.1080/17425247.2022.2084070

165. Böttger K, Hatzikirou H, Voss-Böhme A, Cavalcanti-Adam EA, Herrero MA, Deutsch A. An Emerging Allee Effect Is Critical for Tumor Initiation and Persistence. PLoS Computational Biology. 2015;11: e1004366. doi:10.1371/journal.pcbi.1004366

166. Korolev KS, Xavier JB, Gore J. Turning ecology and evolution against cancer. Nature Reviews Cancer. 2014;14: 371–380. doi:10.1038/nrc3712

167. Sewalt L, Harley K, Van Heijster P, Balasuriya S. Influences of Allee effects in the spreading of malignant tumours. Journal of Theoretical Biology. 2016;394: 77–92. doi:10.1016/j.jtbi.2015.12.024

168. Jain RK, Stylianopoulos T. Delivering nanomedicine to solid tumors. Nature Reviews Clinical Oncology. 2010;7: 653–664. doi:10.1038/nrclinonc.2010.139

169. Stylianopoulos T, Jain RK. Design considerations for nanotherapeutics in oncology. Nanomedicine: Nanotechnology, Biology and Medicine. 2015;11: 1893–1907. doi:10.1016/j.nano.2015.07.015

170. Angeli S, Stylianopoulos T. Biphasic modeling of brain tumor biomechanics and response to radiation treatment. Journal of Biomechanics. 2016;49: 1524–1531. doi:10.1016/j.jbiomech.2016.03.029

171. Vavourakis V, Wijeratne PA, Shipley R, Loizidou M, Stylianopoulos T, Hawkes DJ. A Validated Multiscale In-Silico Model for Mechano-sensitive Tumour Angiogenesis and Growth. PLoS Computational Biology. 2017;13: e1005259. doi:10.1371/journal.pcbi.1005259

172. Koumoutsakos P, Pivkin I, Milde F. The Fluid Mechanics of Cancer and Its Therapy. Annual Review of Fluid Mechanics. 2013;45: 325–355. doi:10.1146/annurev-fluid-120710-101102

173. Sun Q, Hong Z, Zhang C, Wang L, Han Z, Ma D. Immune checkpoint therapy for solid tumours: clinical dilemmas and future trends. Signal Transduction and Targeted Therapy. 2023;8: 320. doi:10.1038/s41392-023-01522-4

174. Mpekris F, Panagi M, Michael C, Voutouri C, Tsuchiya M, Wagatsuma C, et al. Translational nanomedicine potentiates immunotherapy in sarcoma by normalizing the microenvironment. Journal of Controlled Release. 2023;353: 956–964. doi:10.1016/j.jconrel.2022.12.016

175. Mpekris F, Panagi M, Voutouri C, Martin JD, Samuel R, Takahashi S, et al. Normalizing the Microenvironment Overcomes Vessel Compression and Resistance to Nano-immunotherapy in Breast Cancer Lung Metastasis. Advanced Science. 2021;8: 2001917. doi:10.1002/advs.202001917

176. Panagi M, Mpekris F, Chen P, Voutouri C, Nakagawa Y, Martin JD, et al. Polymeric micelles effectively reprogram the tumor microenvironment to potentiate nano-immunotherapy in mouse breast cancer models. Nature Communications. 2022;13: 7165. doi:10.1038/s41467-022-34744-1

177. Voutouri C, Panagi M, Mpekris F, Stylianou A, Michael C, Averkiou MA, et al. Endothelin Inhibition Potentiates Cancer Immunotherapy Revealing Mechanical Biomarkers Predictive of Response. Advanced Therapeutics. 2021;4: 2000289. doi:10.1002/adtp.202000289

178. Chauhan VP, Chen IX, Tong R, Ng MR, Martin JD, Naxerova K, et al. Reprogramming the microenvironment with tumor-selective angiotensin blockers enhances cancer immunotherapy. Proceedings of the National Academy of Sciences. 2019;116: 10674–10680. doi:10.1073/pnas.1819889116

179. Chen IX, Chauhan VP, Posada J, Ng MR, Wu MW, Adstamongkonkul P, et al. Blocking CXCR4 alleviates desmoplasia, increases T-lymphocyte infiltration, and improves immunotherapy in metastatic breast cancer. Proceedings of the National Academy of Sciences. 2019;116: 4558–4566. doi:10.1073/pnas.1815515116

180. Chauhan VP, Martin JD, Liu H, Lacorre DA, Jain SR, Kozin SV, et al. Angiotensin inhibition enhances drug delivery and potentiates chemotherapy by decompressing tumour blood vessels. Nature Communications. 2013;4: 2516. doi:10.1038/ncomms3516

181. Datta M, Chatterjee S, Perez EM, Gritsch S, Roberge S, Duquette M, et al. Losartan controls immune checkpoint blocker-induced edema and improves survival in glioblastoma mouse models. Proceedings of the National Academy of Sciences. 2023;120: e2219199120. doi:10.1073/pnas.2219199120

182. Mpekris F, Voutouri C, Panagi M, Baish JW, Jain RK, Stylianopoulos T. Normalizing tumor microenvironment with nanomedicine and metronomic therapy to improve immunotherapy. Journal of Controlled Release. 2022;345: 190–199. doi:10.1016/j.jconrel.2022.03.008

183. Panagi M, Voutouri C, Mpekris F, Papageorgis P, Martin MR, Martin JD, et al. TGF-β inhibition combined with cytotoxic nanomedicine normalizes triple negative breast cancer microenvironment towards anti-tumor immunity. Theranostics. 2020;10: 1910–1922. doi:10.7150/thno.36936

184. Voutouri C, Mpekris F, Panagi M, Krolak C, Michael C, Martin JD, et al. Ultrasound stiffness and perfusion markers correlate with tumor volume responses to immunotherapy. Acta Biomaterialia. 2023;167: 121–134. doi:10.1016/j.actbio.2023.06.007

185. Yu J-L, Jang SR-J. A mathematical model of tumor-immune interactions with an immune checkpoint inhibitor. Applied Mathematics and Computation. 2019;362: 124523. doi:10.1016/j.amc.2019.06.037

186. Koukourakis MI, Giatromanolaki A. Tumor draining lymph nodes, immune response, and radiotherapy: Towards a revisal of therapeutic principles. Biochimica et Biophysica Acta (BBA) - Reviews on Cancer. 2022;1877: 188704. doi:10.1016/j.bbcan.2022.188704

187. Salgado E, Cao Y. Pharmacokinetics and pharmacodynamics of therapeutic antibodies in tumors and tumor-draining lymph nodes. Mathematical Biosciences and Engineering. 2021;18: 112–131. doi:10.3934/mbe.2021006

188. Salgado E, Cao Y. A Physiologically Based Pharmacokinetic Framework for Quantifying Antibody Distribution Gradients from Tumors to Tumor-Draining Lymph Nodes. Antibodies. 2022;11: 28. doi:10.3390/antib11020028

189. Harkos C, Stylianopoulos T, Jain RK. Mathematical modeling of intratumoral immunotherapy yields strategies to improve the treatment outcomes. PLoS Computational Biology. 2023;19: e1011740. doi:10.1371/journal.pcbi.1011740

190. Deen WM. Hindered transport of large molecules in liquid-filled pores. AIChE Journal. 1987;33: 1409–1425. doi:10.1002/aic.690330902

191. Angeli S, Emblem KE, Due-Tonnessen P, Stylianopoulos T. Towards patient-specific modeling of brain tumor growth and formation of secondary nodes guided by DTI-MRI. NeuroImage: Clinical. 2018;20: 664–673. doi:10.1016/j.nicl.2018.08.032

192. Stylianopoulos T, Yeckel A, Derby JJ, Luo X-J, Shephard MS, Sander EA, et al. Permeability calculations in three-dimensional isotropic and oriented fiber networks. Physics of Fluids. 2008;20: 123601. doi:10.1063/1.3021477

193. Simpson RC, Shanahan ER, Batten M, Reijers ILM, Read M, Silva IP, et al. Diet-driven microbial ecology underpins associations between cancer immunotherapy outcomes and the gut microbiome. Nature Medicine. 2022;28: 2344–2352. doi:10.1038/s41591-022-01965-2

194. Villemin C, Six A, Neville BA, Lawley TD, Robinson MJ, Bakdash G. The heightened importance of the microbiome in cancer immunotherapy. Trends in Immunology. 2023;44: 44–59. doi:10.1016/j.it.2022.11.002

195. Yi M, Jiao D, Qin S, Chu Q, Li A, Wu K. Manipulating Gut Microbiota Composition to Enhance the Therapeutic Effect of Cancer Immunotherapy. Integrative Cancer Therapies. 2019;18: 153473541987635. doi:10.1177/1534735419876351

196. Dai Z, Zhang J, Wu Q, Fang H, Shi C, Li Z, et al. Intestinal microbiota: a new force in cancer immunotherapy. Cell Communication and Signaling. 2020;18: 90. doi:10.1186/s12964-020-00599-6

197. Fessler J, Matson V, Gajewski TF. Exploring the emerging role of the microbiome in cancer immunotherapy. Journal for ImmunoTherapy of Cancer. 2019;7: 108. doi:10.1186/s40425-019-0574-4

198. Stein-Thoeringer CK, Saini NY, Zamir E, Blumenberg V, Schubert M-L, Mor U, et al. A non-antibiotic-disrupted gut microbiome is associated with clinical responses to CD19-

CAR-T cell cancer immunotherapy. Nature Medicine. 2023;29: 906–916. doi:10.1038/s41591-023-02234-6

199. Voutouri C, Nikmaneshi MR, Hardin CC, Patel AB, Verma A, Khandekar MJ, et al. In silico dynamics of COVID-19 phenotypes for optimizing clinical management. Proceedings of the National Academy of Sciences. 2021;118: e2021642118. doi:10.1073/pnas.2021642118

200. Subudhi S, Voutouri C, Hardin CC, Nikmaneshi MR, Patel AB, Verma A, et al. Strategies to minimize heterogeneity and optimize clinical trials in Acute Respiratory Distress Syndrome (ARDS): Insights from mathematical modelling. eBioMedicine. 2022;75: 103809. doi:10.1016/j.ebiom.2021.103809

201. Bucci V, Tzen B, Li N, Simmons M, Tanoue T, Bogart E, et al. MDSINE: Microbial Dynamical Systems INference Engine for microbiome time-series analyses. Genome Biology. 2016;17: 121. doi:10.1186/s13059-016-0980-6

202. Stein RR, Bucci V, Toussaint NC, Buffie CG, Rätsch G, Pamer EG, et al. Ecological Modeling from Time-Series Inference: Insight into Dynamics and Stability of Intestinal Microbiota. PLoS Computational Biology. 2013;9: e1003388. doi:10.1371/journal.pcbi.1003388

203. Marino S, Baxter NT, Huffnagle GB, Petrosino JF, Schloss PD. Mathematical modeling of primary succession of murine intestinal microbiota. Proceedings of the National Academy of Sciences. 2014;111: 439–444. doi:10.1073/pnas.1311322111

204. Stein RR, Tanoue T, Szabady RL, Bhattarai SK, Olle B, Norman JM, et al. Computer-guided design of optimal microbial consortia for immune system modulation. eLife. 2018;7: e30916. doi:10.7554/eLife.30916

205. Rolig AS, Parthasarathy R, Burns AR, Bohannan BJM, Guillemin K. Individual Members of the Microbiota Disproportionately Modulate Host Innate Immune Responses. Cell Host & Microbe. 2015;18: 613–620. doi:10.1016/j.chom.2015.10.009

206. Gordon SR, Maute RL, Dulken BW, Hutter G, George BM, McCracken MN, et al. PD-1 expression by tumour-associated macrophages inhibits phagocytosis and tumour immunity. Nature. 2017;545: 495–499. doi:10.1038/nature22396

207. Dranoff G. Cytokines in cancer pathogenesis and cancer therapy. Nat Rev Cancer. 2004;4: 11–22. doi:10.1038/nrc1252

208. Rőszer T. Understanding the Mysterious M2 Macrophage through Activation Markers and Effector Mechanisms. Mediators of Inflammation. 2015;2015: 1–16. doi:10.1155/2015/816460

209. Balar AV, Galsky MD, Rosenberg JE, Powles T, Petrylak DP, Bellmunt J, et al. Atezolizumab as first-line treatment in cisplatin-ineligible patients with locally advanced and metastatic urothelial carcinoma: a single-arm, multicentre, phase 2 trial. The Lancet. 2017;389: 67–76. doi:10.1016/S0140-6736(16)32455-2

210. Lagarias JC, Reeds JA, Wright MH, Wright PE. Convergence Properties of the Nelder--Mead Simplex Method in Low Dimensions. SIAM Journal on Optimization. 1998;9: 112–147. doi:10.1137/S1052623496303470

211. Nelder JA, Mead R. A Simplex Method for Function Minimization. The Computer Journal. 1965;7: 308–313. doi:10.1093/comjnl/7.4.308

212. Lu D, Ni Z, Liu X, Feng S, Dong X, Shi X, et al. Beyond T Cells: Understanding the Role of PD-1/PD-L1 in Tumor-Associated Macrophages. Journal of Immunology Research. Hindawi Limited; 2019. doi:10.1155/2019/1919082

213. Gordon SR, Maute RL, Dulken BW, Hutter G, George BM, McCracken MN, et al. PD-1 expression by tumour-associated macrophages inhibits phagocytosis and tumour immunity. Nature. Nature Publishing Group; 2017. pp. 495–499. doi:10.1038/nature22396

214. Dranoff G. Cytokines in cancer pathogenesis and cancer therapy. Nature Reviews Cancer. Nature Publishing Group; 2004. pp. 11–22. doi:10.1038/nrc1252

215. Roszer T. Understanding the mysterious M2 macrophage through activation markers and effector mechanisms. Mediators of Inflammation. Hindawi Limited; 2015. doi:10.1155/2015/816460

216. Sakaguchi S, Powrie F. Emerging challenges in regulatory T cell function and biology. Science. American Association for the Advancement of Science; 2007. pp. 627–629. doi:10.1126/science.1142331

217. Hexun Z, Miyake T, Maekawa T, Mori H, Yasukawa D, Ohno M, et al. High abundance of Lachnospiraceae in the human gut microbiome is related to high immunoscores in advanced colorectal cancer. Cancer Immunology, Immunotherapy. 2023;72: 315–326. doi:10.1007/s00262-022-03256-8

218. Zhang X, Yu D, Wu D, Gao X, Shao F, Zhao M, et al. Tissue-resident Lachnospiraceae family bacteria protect against colorectal carcinogenesis by promoting tumor immune surveillance. Cell Host & Microbe. 2023;31: 418-432.e8. doi:10.1016/j.chom.2023.01.013

219. Mao J, Wang D, Long J, Yang X, Lin J, Song Y, et al. Gut microbiome is associated with the clinical response to anti-PD-1 based immunotherapy in hepatobiliary cancers. Journal for ImmunoTherapy of Cancer. 2021;9: e003334. doi:10.1136/jitc-2021-003334

220. Peng Z, Cheng S, Kou Y, Wang Z, Jin R, Hu H, et al. The Gut Microbiome Is Associated with Clinical Response to Anti–PD-1/PD-L1 Immunotherapy in Gastrointestinal Cancer. Cancer Immunology Research. 2020;8: 1251–1261. doi:10.1158/2326-6066.CIR-19-1014

221. Chen Y, Liu Y, Wang Y, Chen X, Wang C, Chen X, et al. Prevotellaceae produces butyrate to alleviate PD-1/PD-L1 inhibitor-related cardiotoxicity via PPARα-CYP4X1 axis in colonic macrophages. Journal of Experimental & Clinical Cancer Research. 2022;41: 1. doi:10.1186/s13046-021-02201-4

222. Wang Y, Du J, Gao Z, Sun H, Mei M, Wang Y, et al. Evolving landscape of PD-L2: bring new light to checkpoint immunotherapy. British Journal of Cancer. 2023;128: 1196–1207. doi:10.1038/s41416-022-02084-y

223. Netti PA, Berk DA, Swartz MA, Grodzinsky AJ, Jain RK. Role of extracellular matrix assembly in interstitial transport in solid tumors. Cancer Research. 2000;60: 2497–2503.

224. Hermann PC, Huber SL, Herrler T, Aicher A, Ellwart JW, Guba M, et al. Distinct Populations of Cancer Stem Cells Determine Tumor Growth and Metastatic Activity in Human Pancreatic Cancer. Cell Stem Cell. 2007;1: 313–323. doi:10.1016/j.stem.2007.06.002

225. Casciari JJ, Sotirchos S V., Sutherland RM. Variations in tumor cell growth rates and metabolism with oxygen concentration, glucose concentration, and extracellular pH. Journal of Cellular Physiology. 1992;151: 386–394. doi:10.1002/jcp.1041510220

226. Schmidt MM, Wittrup KD. A modeling analysis of the effects of molecular size and binding affinity on tumor targeting. Molecular Cancer Therapeutics. 2009;8: 2861–2871. doi:10.1158/1535-7163.MCT-09-0195

227. Pluen A, Boucher Y, Ramanujan S, McKee TD, Gohongi T, Di Tomaso E, et al. Role of tumor-host interactions in interstitial diffusion of macromolecules: Cranial vs. subcutaneous tumors. Proceedings of the National Academy of Sciences of the United States of America. 2001;98: 4628–4633. doi:10.1073/pnas.081626898

228. Chauhan VP, Stylianopoulos T, Martin JD, PopoviÄ Z, Chen O, Kamoun WS, et al. Normalization of tumour blood vessels improves the delivery of nanomedicines in a size-dependent manner. Nature Nanotechnology. 2012;7: 383–388. doi:10.1038/nnano.2012.45

229. Késmárky G, Kenyeres P, Rábai M, Tóth K. Plasma viscosity: A forgotten variable. Clinical Hemorheology and Microcirculation. 2008;39: 243–246. doi:10.3233/CH-2008-1088

230. Voutouri C, Kirkpatrick ND, Chung E, Mpekris F, Baish JW, Munn LL, et al. Experimental and computational analyses reveal dynamics of tumor vessel cooption and optimal treatment strategies. Proceedings of the National Academy of Sciences. 2019;116: 2662–2671. doi:10.1073/pnas.1818322116

231. Zhan W, Wang C-H. Convection enhanced delivery of liposome encapsulated doxorubicin for brain tumour therapy. Journal of Controlled Release. 2018;285: 212–229. doi:10.1016/j.jconrel.2018.07.006

232. Lambride C, Vavourakis V, Stylianopoulos T. Convection-Enhanced Delivery In Silico Study for Brain Cancer Treatment. Frontiers in Bioengineering and Biotechnology. 2022;10: 867552. doi:10.3389/fbioe.2022.867552

233. Zhao J, Cao Y, Jusko WJ. Across-Species Scaling of Monoclonal Antibody Pharmacokinetics Using a Minimal PBPK Model. Pharmaceutical Research. 2015;32: 3269–3281. doi:10.1007/s11095-015-1703-5

234. Van Den Broeck W, Derore A, Simoens P. Anatomy and nomenclature of murine lymph nodes: Descriptive study and nomenclatory standardization in BALB/cAnNCrl mice. Journal of Immunological Methods. 2006;312: 12–19. doi:10.1016/j.jim.2006.01.022

235. Stenken JA, Poschenrieder AJ. Bioanalytical chemistry of cytokines – A review. Analytica Chimica Acta. 2015;853: 95–115. doi:10.1016/j.aca.2014.10.009

236. Zhang Q, Liu Y-J, Li J-P, Zeng S-H, Shen H, Han M, et al. USP35 is a Potential Immunosuppressive Factor in Skin Cutaneous Melanoma. Journal of Inflammation Research. 2022;Volume 15: 3065–3082. doi:10.2147/JIR.S362619

237. Lai X, Friedman A. Combination therapy of cancer with cancer vaccine and immune checkpoint inhibitors: A mathematical model. PLOS ONE. 2017;12: e0178479. doi:10.1371/JOURNAL.PONE.0178479

238. Voutouri C, Nikmaneshi MR, Hardin CC, Patel AB, Verma A, Khandekar MJ, et al. In silico dynamics of COVID-19 phenotypes for optimizing clinical management. Proceedings of the National Academy of Sciences. 2021;118: e2021642118. doi:10.1073/pnas.2021642118

239. Friedman A, Hao W. The Role of Exosomes in Pancreatic Cancer Microenvironment. Bulletin of Mathematical Biology 2017 80:5. 2017;80: 1111–1133. doi:10.1007/S11538-017-0254-9

240. Lee HY, Topham DJ, Park SY, Hollenbaugh J, Treanor J, Mosmann TR, et al. Simulation and Prediction of the Adaptive Immune Response to Influenza A Virus Infection. Journal of Virology. 2009;83: 7151–7165. doi:10.1128/JVI.00098-09

Appendix 1: Scan and model parameters for chapter 2

Table 9: Scan parameters for the derivation of Diffusion Tensor Imaging and MR Elastography for patients and healthy subject.

Sequence	Repetition time (ms)	Echo time (ms)	Acquisition matrix	Resolution (mm^3)	Additional information
Diffusion Tensor Imaging	9800	60	$94 \times 94 \times 50$	$2.5 \times 2.5 \times 2.5$	Spin echo, single-shot, echo-planar imaging readout, sensitivity encoding 2, 15 gradient directions, b-values 0 s/mm^2 and 800 s/mm^2
MR Elastography	295	12	$72 \times 70 \times 15$	$3.1 \times 3.1 \times 3.1$	Motion-encoding gradient strength 13.2 mT/m, sensitivity encoding 2

Table 10: Values of model parameters for chapter 2

Parameter	Description	Value	Reference
k_{th}	hydraulic conductivity of tumor	3.8×10^{-12} $m^2 \cdot Pa^{-1} \cdot s^{-1}$	[223]

Parameter	Description	Value	Reference
c_{iox}	oxygen concentration in the vessels	0.2 mol·m^{-3}	[118,224]
D_{ox}	oxygen diffusion coefficient	1.55×10^{-4} m^2·day^{-1}	[118]
A_{ox}	oxygen uptake parameter	2200 mol·m^{-3}·day^{-1}	[118,225]
k_{ox}	oxygen uptake parameter	0.00464 mol·m^{-3}	[118,225]
k_1	growth rate parameter	0.032 day^{-1}	[44]
k_2	growth rate parameter	0.0083 mol·m^{-3}	[225]
ν_{Tumor}	Poisson's ratio (tumor)	0.25	[116]
ν_{Normal}	Poisson's ratio (host)	0.2	[116]
ω	radial frequency	100π rad·s^{-1}	--
ρ_{cell}	constant proliferation rate	0.012 day^{-1}	[85]
p_{v_tumor}	vascular pressure in tumor	1 kPa	[115]
p_{v_Normal}	vascular pressure in host tissue	2 kPa	[115]
p_{vl}	lymphatic pressure	0	[116]
S_{V0}	vascular density of host tissue	70 cm^{-1}	[115]
$L_{pl}\,S_{vl}$	permeability of lymphatics	0.05 (mmHg·s)$^{-1}$	[115]
c_e	receptor concentration	0.01 mol·m^{-3}	[153,226]
Φ	volume fraction of tumor accessible to drug	0.3	[153,226]

Parameter	Description	Value	Reference
k_{on}	binding rate constant	1.296×10^6 $m^3 \cdot mol^{-1} \cdot day^{-1}$	[82,119]
k_{off}	dissociation rate constant	691.2 day^{-1}	[82,119]
k_{int}	internalization rate constant	3.7 day^{-1}	[82,119]
t_0	time of drug injection	41 day	--
$D_{f\_rs=1nm}$	drug diffusion coefficient (1nm)	1×10^{-6} $cm^2 \cdot s^{-1}$	[227]
$D_{f\_rs=35nm}$	drug diffusion coefficient (35nm)	$0.5 \times 10^{-8} cm^2 \cdot s^{-1}$	[227]
$D_{f\_rs=75nm}$	drug diffusion coefficient (75nm)	0.5×10^{-9} $cm^2 \cdot s^{-1}$	[227]
k_d	blood circulation decay	0.417 day^{-1}	[228]
L_{vw}	vessel wall thickness	5×10^{-6} m	[116]
η	plasma viscosity at 310K	1.3×10^{-3} Pa·s	[229]
γ_{tumor}	fraction of vessel wall surface area occupied by pores (tumor)	1×10^{-3}	[228]
γ_{Normal}	fraction of vessel wall surface area occupied by pores (host)	1×10^{-4}	[228]
r_{0_host}	vessel wall pore radius (host)	3.5 nm	[121]
r_{0_tumor}	vessel wall pore radius (tumor)	50–150 nm	[121]

Appendix 2: Model parameters and variables for chapter 3

Table 11: Table of model variables for chapter 3

Description	Variable
Interstitial fluid pressure	p_i
Fluid velocity	v^f
Solid velocity	v^b
Free conjugated-cytokines	Ic_f
Conjugated-cytokines bound	Ic_b
Conjugated-cytokines in the blood	Ic_{blood}
Growth stretch ratio	λ_g
Pro-inflammatory cytokines produced from immune cells	c_c
Total pro-inflammatory cytokines	c
Antigen presenting cells	APC
Effector CD4+ T cells	Th^E
Effector CD8+ T cells	T^E
Innate cells	In
Cancer cells	$\overline{T}$
Antigen	A_g
Oxygen	c_{ox}

Table 12: Table of model parameters for chapter 3

Description	Parameter	Value	Reference
Hydraulic conductivity (tumor)	k_{thT}	$4.13 \cdot 10^{-8}\ cm^2 \cdot mmHg^{-1} \cdot s^{-1}$	[11]
Hydraulic conductivity (host)	k_{thH}	$8.53 \cdot 10^{-9}\ cm^2 \cdot mmHg^{-1} \cdot s^{-1}$	[11]
Oxygen concentration in the vessels	c_{iox}	$0.2\ mol \cdot m^{-3}$	[118,224]
Oxygen diffusion coefficient	D_{ox}	$1.55 \cdot 10^{-4}\ m^2 \cdot day^{-1}$	[118]
Oxygen uptake parameter A	A_{ox}	$2200\ mol \cdot m^{-3} \cdot day^{-1}$	[118,225]
Oxygen uptake parameter k	k_{ox}	$0.00464\ mol \cdot m^{-3}$	[118,225]
Growth rate parameter	k_2	$0.0083\ mol \cdot m^{-3}$	[225]
Vascular pressure	p_v	$15.6\ mmHg$	[11]
Lymphatic pressure	p_{vl}	0	[116]
Vascular density (host)	S_{vH}	$70\ cm^{-1}$	[6]
Vascular density (tumor)	S_{vT}	$50\ cm^{-1}$	[6]
Permeability of lymphatics	$L_{pl}S_{vl}$	$0.05\ mmHg^{-1} \cdot s^{-1}$	[11]
Vessel wall thickness	L_{vw}	$5 \cdot 10^{-6}\ m$	[116]
Water viscosity at 310K	vis	$7 \cdot 10^{-4}\ Pa \cdot s$	[116]
Fraction of vessel wall surface area occupied by pores (tumor)	γ_T	10^{-3}	[228]

Description	Parameter	Value	Reference
Fraction of vessel wall surface area occupied by pores (host)	γ_H	10^{-4}	[228]
Vessel wall pore radius (host)	r_{0H}	3.5 nm	[121]
Vessel wall pore radius (tumor)	r_{0T}	100 nm	[121]
Production of proinflammatory cytokines by innate immune cells	k_{In}	$3 \cdot 10^{-8}$ day^{-1}	[146]
Production of proinflammatory cytokines by effector CD8+ Tcells	k_{T^E}	$3 \cdot 10^{-8}$ day^{-1}	[146]
Production of proinflammatory cytokines by effector CD4+ Tcells	k_{Th^E}	$3 \cdot 10^{-8}$ day^{-1}	[146]
Production of proinflammatory cytokines by antigen presenting cells	k_{APC}	$3 \cdot 10^{-8}$ day^{-1}	[146]
Initial degradation of antigen presenting cells	δ_{APC_0}	0.1 day^{-1}	[146]

Description	Parameter	Value	Reference
Initial degradation of immature antigen presenting cells	$\delta_{\mathrm{IAPC_0}}$	$0.1\ \mathrm{day}^{-1}$	[146]
Initial degradation of effector CD4+ Tcells	$\delta_{\mathrm{Th_0^E}}$	$0.197\ \mathrm{day}^{-1}$	[146]
Initial degradation of effector CD8+ Tcells	$\delta_{\mathrm{T_0^E}}$	$0.18\ \mathrm{day}^{-1}$	[146]
Initial degradation of Innate immune cells	$\delta_{\mathrm{In_0}}$	$0.18\ \mathrm{day}^{-1}$	[146]
Degradation of cytokines produced by immune cells	$\delta_{\mathrm{c_c}}$	$1.38\ \mathrm{day}^{-1}$	[146]
The rate in which the drug exits through the lymphatic vessels (host)	$\delta_{\mathrm{Ic_{flH}}}$	$1.38\ \mathrm{day}^{-1}$	[146]
The rate in which the drug exits through the lymphatic vessels (tumor)	$\delta_{\mathrm{Ic_{flT}}}$	0	[82]
Production of APCs	χ_{APC}	$0.5\ \mathrm{cm}^3 \cdot \mathrm{g}^{-1}$	This study
Growth rate parameter (Agarwal et. al.)	$\mathrm{k_{1A}}$	$0.19409\ \mathrm{day}^{-1}$	Optimization
Growth rate parameter (Momin et. al.)	$\mathrm{k_{1M}}$	$0.3446\ \mathrm{day}^{-1}$	Optimization
Source of effector CD4+ and source of effector CD8+ (Momin et. al.)	$\mathrm{m_{APCM}}$	$2.36 \cdot 10^{-6}\ \mathrm{s}^{-1}$	Optimization

Description	Parameter	Value	Reference
Production of NK (Momin et. al.)	λ_{InM}	$0.025\ \mathrm{g}\cdot\mathrm{cm}^{-3}\cdot\mathrm{day}^{-1}$	Optimization
Production of IAPC (Momin et. al.)	λ_{IAPCM}	$0.025\ \mathrm{g}\cdot\mathrm{cm}^{-3}\cdot\mathrm{day}^{-1}$	Optimization
Half saturation concentration Innate cells (Momin et. al.)	$\mathrm{K}_{\mathrm{cInM}}$	$9.1346\cdot10^{-4}\ \mathrm{g}\cdot\mathrm{cm}^{-3}$	Optimization
Half saturation antigen presenting cells (Momin et. al.)	$\mathrm{K}_{\mathrm{cAPCM}}$	$9.1346\cdot10^{-4}\ \mathrm{g}\cdot\mathrm{cm}^{-3}$	Optimization
Killing rate constants of tumor cells by innate immune cells (Momin et. al.)	$\mathrm{n}_{\mathrm{InM}}$	$54.1857\ \mathrm{cm}^{3}\cdot\mathrm{g}^{-1}\cdot\mathrm{day}^{-1}$	Optimization
killing rate constants of tumor cells by adaptive immune cells (Momin et. al.)	$\mathrm{n}_{\mathrm{adM}}$	$108.3713\ \mathrm{cm}^{3}\cdot\mathrm{g}^{-1}\cdot\mathrm{day}^{-1}$	Optimization
Antigen uptake rate (Momin et. al.)	$\mathrm{n}_{\mathrm{A_gM}}$	$108.3713\ \mathrm{cm}^{3}\cdot\mathrm{g}^{-1}\cdot\mathrm{day}^{-1}$	Optimization
Source of effector CD4+ and source of effector CD8+ (Agarwal et. al.)	$\mathrm{m}_{\mathrm{APCA}}$	$2.1395\cdot10^{-6}\ \mathrm{s}^{-1}$	Optimization
Production of NK (Agarwal et. al.)	λ_{InA}	$0.0253\ \mathrm{g}\cdot\mathrm{cm}^{-3}\cdot\mathrm{day}^{-1}$	Optimization

Description	Parameter	Value	Reference
Production of IAPC (Agarwal et. al.)	λ_{IAPCA}	$0.0253\ \mathrm{g}\cdot\mathrm{cm}^{-3}\cdot\mathrm{day}^{-1}$	Optimization
Half saturation concentration Innate cells (Agarwal et. al.)	$\mathrm{K}_{\mathrm{cInA}}$	$7.0143\cdot10^{-4}\ \mathrm{g}\cdot\mathrm{cm}^{-3}$	Optimization
Half saturation antigen presenting cells (Agarwal et. al.)	$\mathrm{K}_{\mathrm{cAPCA}}$	$7.0143\cdot10^{-4}\ \mathrm{g}\cdot\mathrm{cm}^{-3}$	Optimization
Killing rate constants of tumor cells by innate immune cells (Agarwal et. al.)	$\mathrm{n}_{\mathrm{InA}}$	$44.0016\ \mathrm{cm}^{3}\cdot\mathrm{g}^{-1}\cdot\mathrm{day}^{-1}$	Optimization
Killing rate constants of tumor cells by adaptive immune cells (Agarwal et. al.)	$\mathrm{n}_{\mathrm{adA}}$	$88.0032\ \mathrm{cm}^{3}\cdot\mathrm{g}^{-1}\cdot\mathrm{day}^{-1}$	Optimization
Antigen uptake rate (Agarwal et. al.)	$\mathrm{n}_{\mathrm{A_gA}}$	$88.0032\ \mathrm{cm}^{3}\cdot\mathrm{g}^{-1}\cdot\mathrm{day}^{-1}$	Optimization
Diffusion coefficient IAPC	$\mathrm{D}_{\mathrm{IAPC}}$	$4.4150\cdot10^{-4}\ \mathrm{cm}^{2}\cdot\mathrm{day}^{-1}$	[230]
Diffusion coefficient APC	$\mathrm{D}_{\mathrm{APC}}$	$4.4150\cdot10^{-4}\ \mathrm{cm}^{2}\cdot\mathrm{day}^{-1}$	[230]
Diffusion coefficient CD4	$\mathrm{D}_{\mathrm{Th^E}}$	$4.4150\cdot10^{-4}\ \mathrm{cm}^{2}\cdot\mathrm{day}^{-1}$	[230]
Diffusion coefficient CD8	$\mathrm{D}_{\mathrm{T^E}}$	$4.4150\cdot10^{-4}\ \mathrm{cm}^{2}\cdot\mathrm{day}^{-1}$	[230]
Diffusion coefficient Innate immune cells	D_{In}	$4.4150\cdot10^{-4}\ \mathrm{cm}^{2}\cdot\mathrm{day}^{-1}$	[230]
Diffusion cancer cells	$\mathrm{D}_{\overline{\mathrm{T}}}$	$4.4150\cdot10^{-4}\ \mathrm{cm}^{2}\cdot\mathrm{day}^{-1}$	[230]

Description	Parameter	Value	Reference
Diffusion coefficient pro-inflamatory cytokines by immune cells	D_{c_c}	$6.0472 \cdot 10^{-2}\ cm^2 \cdot day^{-1}$	[145]
Diffusion coefficient Antigen	D_{A_g}	$6.0472 \cdot 10^{-2}\ cm^2 \cdot day^{-1}$	[145]
Volume of blood	V_{blood}	$2\ mL$	[22]
Volume fraction of tumor accessible to drug	Φ	0.3	[153,226]
Initial concentration of pro inflammatory cytokines produced by immune cells	c_{cin}	$3 \cdot 10^{-11}\ g \cdot cm^{-3}$	[146]
Initial concentration of Innate immune cells	In_{In}	$9 \cdot 10^{-4}\ g \cdot cm^{-3}$	[146]
Initial concentration of Immature antigen presenting cells	$IAPC_{In}$	$5 \cdot 10^{-5}\ g \cdot cm^{-3}$	[146]
Initial concentration of tumor cells	$\overline{T_0}$	$0.4\ g \cdot cm^{-3}$	[146]
Tumor region threshold concentration	$Thld$	$0.2\ g \cdot cm^{-3}$	This study
Concentration of surface receptors	c_e	$2 \cdot 10^{-4}\ mol \cdot m^{-3}$	[22]
Binding rate constant	k_{on}	$1 \cdot 10^{2}\ m^3 \cdot mol^{-1} \cdot s^{-1}$	[22]
Dissociation rate constant	k_{off}	$1 \cdot 10^{-3}\ s^{-1}$	[22]
Density	ρ	$1000\ kg \cdot m^{-3}$	[231]

Description	Parameter	Value	Reference
Inflow velocity	V_{in}	$0.075215\ m \cdot s^{-1}$	This study
Porosity	ϵ_p	0.3	[232]
Initial concentration of injected cytokines (Momin et. al.)	$Ic_{f_{InM}}$	$0.082645\ mol \cdot m^{-3}$	[22]
Initial concentration of injected cytokines (Agarwal et. al.)	$Ic_{f_{InA}}$	$0.01\ mol \cdot m^{-3}$	[20]
Molecular weight of agonist (Momin et. al.)	M_{wM}	121kDa	[21]
Diffusion coefficient injected pro-inflamatory cytokines free (Momin et. al.)	D_{Ic_fM}	$0.5 \cdot 10^{-6}\ cm^2 \cdot s^{-1}$	[227]
Rate of clearance of agonist (Momin et. al.)	δ_{clearM}	$0.4\ hr^{-1}$	[226]
Initial tumor radius (Momin et. al.)	$TumorX_M$	2.3489 mm	[21]
Molecular weight of agonist (Agarwal et. al.)	M_{wA}	65kDa	[20]
Diffusion coefficient injected pro-inflamatory cytokines free (Agarwal et. al.)	D_{Ic_fA}	$0.75 \cdot 10^{-6}\ cm^2 \cdot s^{-1}$	[227]

Description	Parameter	Value	Reference
Rate of clearance of agonist (Agarwal et. al.)	δ_{clearA}	$1.5\ \mathrm{hr}^{-1}$	[226]
Initial tumor radius (Agarwal et. al.)	$\mathrm{TumorX}_{\mathrm{A}}$	$2.8338\ \mathrm{mm}$	[20]

Appendix 3: Model parameters for chapter 4

Table 13: Table of model parameters for chapter 4

Description	Parameter	Value	Reference
Hydraulic conductivity (tumor)	k_{thT}	$4.13 \cdot 10^{-8}\ cm^2 \cdot mmHg^{-1} \cdot s^{-1}$	[11]
Hydraulic conductivity (host)	k_{thH}	$8.53 \cdot 10^{-9}\ cm^2 \cdot mmHg^{-1} \cdot s^{-1}$	[11]
Oxygen concentration in the vessels	c_{iox}	$0.2\ mol \cdot m^{-3}$	[118,224]
Oxygen diffusion coefficient	D_{ox}	$1.55 \cdot 10^{-4}\ m^2 \cdot day^{-1}$	[118]
Oxygen uptake parameter A	A_{ox}	$2200\ mol \cdot m^{-3} \cdot day^{-1}$	[118,225]
Oxygen uptake parameter k	k_{ox}	$0.00464\ mol \cdot m^{-3}$	[118,225]
Growth rate parameter	k_2	$0.0083\ mol \cdot m^{-3}$	[225]
Vascular pressure	p_v	15.6 mmHg	[11]
Lymphatic pressure	p_{vl}	0	[143]

Description	Parameter	Value	Reference
Vascular density (host)	S_{vH}	$70\ cm^{-1}$	[148]
Vascular density (tumor)	S_{vT}	$50\ cm^{-1}$	[148]
Permeability of lymphatics	$L_{pl}S_{vl}$	$0.05\ mmHg^{-1} \cdot s^{-1}$	[11]
Vessel wall thickness	L_{vw}	$5 \cdot 10^{-6}$ m	[143]
Lymphatic vessel wall thickness	L_{vwl}	$5 \cdot 10^{-6}$ m	[143]
Production of proinflammatory cytokines by innate immune cells	k_{In}	$3 \cdot 10^{-8}\ day^{-1}$	[146]
Production rate of pro-inflammatory cytokines by effector CD8+ Tcells	k_{CD8}	$3 \cdot 10^{-8}\ day^{-1}$	[146]
Production rate of pro-inflammatory cytokines by antigen presenting cells	k_{APC}	$3 \cdot 10^{-8}\ day^{-1}$	[146]

Description	Parameter	Value	Reference
Degradation of antigen presenting cells	δ_{APC}	$0.1\ day^{-1}$	[146]
Degradation of immature antigen presenting cells	δ_{IAPC}	$0.1\ day^{-1}$	[146]
Degradation of effector CD8+ Tcells	δ_{CD8}	$0.18\ day^{-1}$	[146]
Degradation of Innate immune cells	δ_{In}	$0.18\ day^{-1}$	[146]
Degradation of cytokines	δ_{c}	$1.38\ day^{-1}$	[146]
Degradation of anti-PDL1	δ_{aPDL1}	$1.38\ day^{-1}$	[146]
Production of APCs	χ_{APC}	$0.5\ cm^3 \cdot g^{-1}$	[189]
Killing rate constant of tumor cells by innate immune cells	n_{In}	$61.88\ cm^3 \cdot g^{-1} \cdot day^{-1}$	[189]
Diffusion coefficient IAPC	D_{IAPC}	$4.4150 \cdot 10^{-4}\ cm^2 \cdot day^{-1}$	[230]

Description	Parameter	Value	Reference
Diffusion coefficient APC	D_{APC}	$4.4150 \cdot 10^{-4}\ cm^2 \cdot day^{-1}$	[230]
Diffusion coefficient CD4	D_{Th^E}	$4.4150 \cdot 10^{-4}\ cm^2 \cdot day^{-1}$	[230]
Diffusion coefficient CD8	D_{CD8}	$4.4150 \cdot 10^{-4}\ cm^2 \cdot day^{-1}$	[230]
Diffusion coefficient Innate immune cells	D_{In}	$4.4150 \cdot 10^{-4}\ cm^2 \cdot day^{-1}$	[230]
Diffusion coefficient of anti-PDL1	D_{aPDL1}	$7.85 \cdot 10^{-2}\ cm^2 \cdot day^{-1}$	[145]
Diffusion coefficient of cancer cells	$D_{\overline{T}}$	$4.4150 \cdot 10^{-4}\ cm^2 \cdot day^{-1}$	[230]
Diffusion coefficient pro-inflamatory cytokines by immune cells	D_c	$6.0472 \cdot 10^{-2}\ cm^2 \cdot day^{-1}$	[145]
Diffusion coefficient Antigen	D_{A_g}	$6.0472 \cdot 10^{-2}\ cm^2 \cdot day^{-1}$	[145]
Volume of blood	V_b	8.5 mL	[233]

Description	Parameter	Value	Reference
Volume of tumor draining lymph nodes	V_l	$1.6\text{mL}/22$	[233,234]
Initial concentration of pro inflammatory cytokines produced by immune cells	c_{in}	$3 \cdot 10^{-11}\ \text{g} \cdot \text{cm}^{-3}$	[146]
Initial concentration of innate immune cells	In_{In}	$9 \cdot 10^{-4}\ \text{g} \cdot \text{cm}^{-3}$	[146]
Initial concentration of Immature antigen presenting cells	$IAPC_{In}$	$5 \cdot 10^{-5}\ \text{g} \cdot \text{cm}^{-3}$	[146]
Initial concentration of tumor cells	$\overline{T_0}$	$0.4\ \text{g} \cdot \text{cm}^{-3}$	[146]
Tumor region threshold concentration	Thld	$0.2\ \text{g} \cdot \text{cm}^{-3}$	[189]
Volumetric flow rate from lymph nodes to blood	$Q^{l \to b}$	$(0.2830/22)\text{ml} \cdot \text{h}^{-1}$	[233,234]

Description	Parameter	Value	Reference
Water viscosity at 310K	vis	$7 \cdot 10^{-4}$ Pa · s	[143]
Fraction of vessel wall surface area occupied by pores (tumor)	γ_T	10^{-3}	[228]
Fraction of vessel wall surface area occupied by pores (host)	γ_H	10^{-4}	[228]
Vessel wall pore radius (host)	r_{0H}	3.5 nm	[121]
Vessel wall pore radius (tumor)	r_{0T}	100 nm	[121]
Molecular weight of anti-PDL1	Mw_{aPDL1}	33 kDa	[235]
Molecular weight of cytokines	Mw_c	33 kDa	[236]
Blocking rate of PDL1 by anti-PDL1	k_{on}	$6.87 \cdot 10^6$ cm^3 · day^{-1} · g^{-1}	[145]
Unbinding rate of PDL1 by anti-PDL1	k_{off}	0.0462 day^{-1}	[145]

Description	Parameter	Value	Reference
Production of NK	λ_{In}	$1 \cdot 10^{-3}\ g \cdot cm^{-3} \cdot day^{-1}$	Optimization
Production of IAPC	λ_{IAPC}	$1 \cdot 10^{-3}\ g \cdot cm^{-3} \cdot day^{-1}$	
Half saturation concentration of innate cells and antigen presenting cells	K_{cIn}, K_{cAPC}	$2.81 \cdot 10^{-6}\ g \cdot cm^{-3}$	
Killing rate constant of tumor cells by innate immune cells	n_{IAPC}	$61.88\ cm^3 \cdot g^{-1} \cdot day^{-1}$	
Killing rate constant of tumor cells by CD8+ Tcells cells and antigen uptake rate	n_{CD8}, n_{A_g}	$123.76\ cm^3 \cdot g^{-1} \cdot day^{-1}$	
Activation rate constant of CD8+ Tcells	h_{CD8}	$17.06\ cm^3 \cdot g^{-1} \cdot day^{-1}$	
Extravasation rate constant for innate immune cells, immature antigen	$z_{In}^{b\to t}, z_{IAPC}^{b\to t}, z_{CD8}^{b\to t}$	$0.28\ s^{-1}$	

Description	Parameter	Value	Reference
presenting cells, CD8+ Tcells			
Rate constant of lymphatic drainage of pro-inflammatory cytokines, anti-PDL1, innate immune cells, immature antigen presenting cells, antigen presenting cells, CD8+ Tcells	$z_c^{t\to l}, z_{aPDL1}^{t\to l}, z_{In}^{t\to l}, z_{IAPC}^{t\to l}, z_{APC}^{t\to l}, z_{CD8}^{t\to l}$	$0.17\ s^{-1}$	
Effectiveness of the killing of cancer cells bound by anti-PDL1 compared to cancer cells with free PDL1 receptors	w_a	1.62	
Source of anti-PDL1	g_{aPDL1}	$2.67 \cdot 10^{-4}\ g \cdot cm^{-3} \cdot day^{-1}$	
Growth rate parameter B16F10	$k_{1B16F10}$	$0.236\ day^{-1}$	

Description	Parameter	Value	Reference
Growth rate parameter 4T1	k_{14T1}	$0.176\ day^{-1}$	
Growth rate parameter E0771	k_{1E0771}	$0.201\ day^{-1}$	
Growth rate parameter MCA205	$k_{1MCA205}$	$0.203\ day^{-1}$	
Vascular density of B16F10 (tumor) for combination therapy	$S_{vTB16F10}$	$230\ cm^{-1}$	
Vascular density of 4T1 (tumor) for combination therapy	S_{vT4T1}	$120\ cm^{-1}$	
Vascular density of E0771 (tumor) for combination therapy	$S_{vTE0771}$	$145\ cm^{-1}$	
Vascular density of MCA205 (tumor) for combination therapy	$S_{vTMCA205}$	$140\ cm^{-1}$	

Appendix 4: Model parameters and variables for chapter 5

Table 14: The variables of that are calculated by our mathematical model. Each variable corresponds to a model component shown in Figure 34

Description	Variable
Pro-Inflammatory cytokines	c
Immunosuppressive cytokines	α
Natural killer cells	NK
Naïve $CD8^+$ T cells	T^N
Effector $CD8^+$ Tcells	T^E
Dendritic cells	DC
Antigen-presenting cells	APC
Naive $CD4^+$ T cells	Th^N
Effector $CD4^+$ T cells	Th^E
Neutrophils	N
Type 1 Macrophages	M_1
Type 2 Macrophages	M_2
Naïve B cells	B^N
Plasma B cells	P

Description	Variable
Memory B cells	MB
joijijo	
Regulatory T cells	T_{reg}
Antibodies against tumor antigen	A
Cancer cells	$\hat{T}$
Dead cancer cells or free tumor antigen	$\hat{T}_D$
Cancer cells carrying antibodies	$\hat{T}_A$
Amount of available PD-L1 on the cells	$[PDL1]$
Amount of the available PD-1 on the cells	$[PD1]$
The concentration of PD-1 – PD-L1 complex	$[PD1-PDL1]$
Concentration of anti-PD-1	$[anti-PD1]$
The concentration of anti-PD-1 - PD-1 complex	$[PD1-antiPD1]$
Concentration of anti-PD-L1	$[anti-PDL1]$
The concentration of anti-PD-L1 - PD-1 complex	$[PDL1-antiPDL1]$

Table 15: Values of model parameters for chapter 5

Name	Symbol	Value	Reference
Production of proinflammatory cytokines by the immune cells	$k_{cNK,}$ k_{cT^E}, k_{cAPC}, k_{cTh^E}, k_{cN}, k_{cM1}, k_{cP}	0.02 day^{-1}	Estimated
Production of immunosuppressive cytokines by the immune cells	$K_{ant-T_{reg}}$, K_{ant-M2}	1.78×10^{-15} day^{-1}	Estimated
Amount of PD-L1 on the immune cells	β_{DC^*}, β_{DC}, β_{M2}, β_{M1}, β_{B^N}, β_P	5.22×10^{-7}	[237]
Amount of PD-1 on the immune cells	a_{T^E}, a_{T_N}, a_{Th_N}, a_N, a_{NK}, a_{M_1}, a_{M_2}, a_{APC}, a_{DC}, $a_{T_{reg}}$	2.49×10^{-7}	[237]
Binding of PD-1 to the PD-L1	a_{PL}	44.58 [cm^3/g/day]	[238]
Unbinding of PD-1 to the PD-L1	d_Q	4.34 [1/d]	[238]
Unbinding of PD-1 to the anti-PD-1 and PD-L1 to the anti-PD-L1	$d_{PD1-aPD1}$, $d_{PDL1-aPDL1}$	0.1 day^{-1}	[238]

Name	Symbol	Value	Reference
Death rate of Tumor cells	d_{Tc}	0	Estimated
Binding of antibodies to Tumor cells	d_A	$2.65x10^{-4}$ [cm^3/g/day]	Estimated
Source of Immune cells	$S_{DC}, S_{TN}, S_B, S_{ThN}$	1.128×10^{-4} [g/ cm^3/d]	Estimated
	S_{Treg}	1.128×10^{-7} [g/ cm^3/d]	
Degradation of Immune cells	$\delta_{DC}, \delta_{APC}, \delta_{Th^N}, \delta_{Th^E}, \delta_{T^N}, \delta_{T^E}, \delta_{M1}, \delta_{M2}, \delta_N, \delta_{NK}, \delta_B, \delta_{MB}, \delta_P$	0.23 day^{-1}	[239]
	δ_{Treg}	0.08 day^{-1}	
Degradation of cytokines	δ_c, δ_a	6.5 day^{-1}	[239]
Production of Antibodies	k_A	0.1 day^{-1}	[240]
Effectiveness of DC to APCs	χ_{DC}	0.54	Estimated
Effectiveness of M1 to APCs	χ_{DC}	0.37	Estimated
Production of immune cells	$\lambda_{NK}, \lambda_{M1}, \lambda_{M2}, \lambda_N$	$1.0x\ 10^{-4}$ [g/ cm^3/d]	Estimated

Name	Symbol	Value	Reference
Half saturation Concentration Neutrophils	K_N	$2.37x10^{-11}$ [g/cm^3]	[239]
Half saturation Concentration Natural killer cells	K_{NK}	$2.37x10^{-11}$ [g/cm^3]	[239]
Half saturation Concentration B cells	K_B	$2.37x10^{-11}$ [g/cm^3]	[239]
Half saturation Concentration of pro inflammatory cytokines for Dendritic cells' activation	K_{cDC}	$1.18x10^{-8}$ [g/cm^3]	Estimated
Half saturation Concentration of anti inflammatory cytokines for APC's activation	K_{aAPC}	$1.20x10^{-12}$ [g/cm^3]	Estimated
Half saturation Concentration for CD4+ activation	K_{Th}	$2.37x10^{-11}$ [g/cm^3]	[239]
Half saturation Concentration for CD8+ activation	K_{T^N}	$2.37x10^{-11}$ [g/cm^3]	[239]

Name	Symbol	Value	Reference
Half saturation Concentration for B cells activation	K_B	$2.37x10^{-11}$ [g/cm^3]	[239]
Killing rate constants	$Krc_{T^E}, Krc_{Nk}, Krc_{M_1}, Krc_N, Krc_{DC}, Krc_{DC^*}$	Varying parameters for fitting experimental data	Optimization
Activation rate constants	$Arc_{Th}, Arc_{T^N}, Arc_{B^N M}, Arc_{B^N P}$	Varying parameters for fitting experimental data -	Optimization

Table 16: The values of model parameter of chapter 5 that were determined by an optimization procedure

Name	Symbol	Value of each study		
		Matson et. al	**Gopalakrishnan et. al**	**Spencer et. al**
Proliferation rate of tumor cells	$k_{\hat{T}}$	0.16 [1/day]	0.25 [1/day]	0.18 [1/day]
Half saturation Concentration of PD-1 PD-L1 complex	K_T	$1.87x10^{-23}$ [g/cm^3]	$3.87x10^{-22}$ [g/cm^3]	-
Amount of PD-L1 on the tumor cells	$\beta_{\hat{T}}$	$1.70x10^{-13}$	$5.3x10^{-13}$	$8.77x10^{-15}$

Name	Symbol	Value of each study		
		Matson et. al	**Gopalakrishnan et. al**	**Spencer et. al**
Unbinding of PD-1 to the PD-L1	d_Q	48.31 [1/d]	4.34 [1/d]	-
Source term of the anti-PD-L1	$\gamma_{anti-PDL1}$	4.34 [g/(cm^3 day)]	4.34 [g/(cm^3 day)]	-
Binding of PD-L1 to the anti-PD-L1	$\mu_{PDL1-aPDL1}$	180.62 [day^{-1} cm^3/g]	180.62[day^{-1} cm^3/g]	-
Degradation of antiPD-L1	$d_{anti-PDL1}$	2.21x10^{-10} [1/d]	2.40x10^{-10} [1/d]	-
Source term of the anti-PD-1	$\gamma_{anti-PD1}$	-	-	84.19 [g/(cm^3 day)]
Binding of PD-1 to the anti-PD-1	$\mu_{PD1-aPD1}$	-	-	102.91 [day^{-1} cm^3/g]
Degradation of antiPD-1	$d_{anti-PD1}$			25.21 [1/d]
Amount of PD-1 on the immune cells	a_{T^E}, a_{Th^E}, a_N, a_{NK}, a_{M_1}, a_{M_2}, a_{APC}, $a_{T_{reg}}$	-	-	1.48x10^{-4}
Amount of PD-1 on the immune cells	a_{T_N}, a_{Th_N}, a_{DC}	-	-	3.08x10^{-8}